

Needle-Tissue Interaction by Experiment

D.J. van Gerwen

NEEDLE-TISSUE INTERACTION BY EXPERIMENT

D.J. van Gerwen

Needle-Tissue Interaction by Experiment

Proefschrift

ter verkrijging van de graad van doctor aan de Technische Universiteit Delft;
op gezag van de Rector Magnificus prof. ir. K.C.A.M. Luyben,
voorzitter van het College voor Promoties
in het openbaar te verdedigen op dinsdag 10 december 2013 om 12.30 uur
door

Dennis Jordi VAN GERWEN

ingenieur luchtvaart en ruimtevaart
geboren te Amstelveen

Dit proefschrift is goedgekeurd door de promotor:
prof. dr. J. Dankelman

Copromotor:
dr. J.J. van den Dobbelsteen

Samenstelling promotiecommissie:

Rector Magnificus,	voorzitter
prof. dr. J. Dankelman,	Technische Universiteit Delft, promotor
dr. J.J. van den Dobbelsteen,	Technische Universiteit Delft, copromotor
prof. dr. ir. S. Stramigioli,	Universiteit Twente
prof. A. Melzer,	University of Dundee
prof. dr. U. Staufer,	Technische Universiteit Delft
prof. dr. ir. C.A. Grimbergen,	Universiteit van Amsterdam
drs. M. Vogt,	Erasmus Medisch Centrum
prof. dr. ir. P. Breedveld,	Technische Universiteit Delft, reservelid

Title: Needle-Tissue Interaction by Experiment
Author: D.J. van Gerwen (d.j.vangerwen@tudelft.nl)
© D.J. van Gerwen 2013
ISBN 978-94-6186-238-9

Summary

Medical needles may not be very popular among patients, but they are exceptionally versatile instruments that have found their way into virtually every clinical intervention imaginable. However, despite their versatility, needles can be very difficult to use, and there is much room for improvement.

Improvements can be realized by optimization of needle geometry, by the development of training facilities for clinicians, imaging modalities and needle-based sensors, by development of needle-steering mechanisms and path planning methods, or even by fully automating the needle insertion process. These approaches all rely on a proper understanding of the mechanical interaction between needle and soft-tissue.

Ideally, insight into needle-tissue interaction mechanics should follow from the development and refinement of theoretical models based on experimental observation. The development of theoretical models has received a lot of attention in the literature, but our inability to collect useful and reliable experimental data remains an important obstacle. For this reason, the present thesis deals with the experimental study of needle-tissue interaction.

The goal of the thesis is to provide insight into needle-tissue interaction mechanics based on experimental observation. To achieve this goal we measure the axial component of the external force acting on the needle during interaction with tissue, and we observe the position of the needle relative to the surrounding tissue.

The first part of the thesis provides a basis for experimentation. This includes a survey of literature related to needle-tissue interaction force measurements. The intention of this survey is to gather existing experimental evidence regarding the influence of different factors, such as needle type, tissue type, and insertion speed, on the axial force. Based on this survey, a data model is constructed that describes the interrelations between the different aspects of needle-tissue interaction experiments. This data model enables the detailed encoding of experimental equipment, conditions, design, and results, and can be used as the blueprint for a database for experimental needle-tissue interaction data.

The second part of the thesis presents two examples of relatively well-controlled experiments involving artificial specimens. These examples illustrate what happens at the tip of a needle during puncture of a membrane. The first experiment involves the use of high speed video to investigate the relation between axial force and needle tip geometry. The second experiment presents a follow-up study that investigates the influence of needle coating (lubrication) on the axial force during membrane puncture.

The last part of the thesis presents two examples of experiments involving biological tissue. The first example is an exploratory study aimed at the characterization of forces during needle insertion into the kidney of a human cadaver. This is done with the help of synchronized ultrasound visualization. The second example is concerned with needle insertion into isolated porcine kidneys, intended to achieve a more detailed characterization of forces for different anatom-

ical structures inside the kidney. This experiment uses synchronized ultrasound visualization with the ultrasound probe moving along with the needle.

The thesis contributes to the field of needle-tissue interaction mechanics by providing an overview of available knowledge concerning needle-tissue interaction forces, and by providing a framework for structuring and expanding this knowledge. The thesis provides some insight by illustrating how needle reuse, needle coating, and specimen boundary conditions influence specific force metrics in artificial specimens. In addition, the thesis provides a first impression of the variability encountered during needle insertion into human cadaverous kidneys, and it provides a multivariate stochastic model of membrane puncture forces in porcine kidneys that can be used to simulate puncture events. However, the most important contribution consists of a set of tools for gathering, analyzing, and disseminating experimental needle-tissue interaction data.

Samenvatting: Naald-weefselinteractie op basis van experimenten

Naalden voor medische doeleinden zijn misschien niet erg populair bij de patiënt, maar het zijn uitzonderlijk veelzijdige instrumenten die hun toepassing vinden in bijna elke denkbare klinische interventie. Ondanks deze veelzijdigheid is het gebruik van een naald vaak moeilijk en is er nog veel ruimte voor verbetering.

Verbetering wordt onder andere gezocht in de optimalisatie van naaldgeometrie, de ontwikkeling van trainingsfaciliteiten voor klinici, de verbetering van beeldvormende technieken, de ontwikkeling van sensoren in de naald, de ontwikkeling van stuurmechanismen en routeplanning van naalden, of zelfs in het volledig automatiseren van het inbrengproces. Al deze toepassingen vereisen een gedegen inzicht in de mechanische interactie tussen naald en weefsel.

In het ideale geval volgt dit inzicht uit het samenspel tussen theorie en experiment, maar in de praktijk is de beschikbare wetenschappelijke literatuur vooral gericht op theoretische modellen en blijkt de ontwikkeling van deze modellen beperkt door een gebrek aan bruikbare experimentele gegevens. Om die reden is dit proefschrift gericht op het empirisch onderzoek van naald-weefselinteractie.

Het doel van dit proefschrift is om op empirische gronden inzicht te verschaffen in de mechanismen van naald-weefselinteractie. Om dit doel te bereiken meten we de axiale component van de externe kracht op de naald tijdens de interactie met verschillende soorten weefsel en observeren we de positie van de naaldpunt ten opzichte van deze weefsels.

Het eerste deel van het proefschrift levert een basis voor het experimenteel onderzoek. Dit gebeurt aan de hand van een literatuuronderzoek waarin experimentele kennis wordt verzameld over de invloed van verschillende factoren, zoals type naald, type weefsel, en inbrengsnelheid, op de axiale kracht. Op basis van dit onderzoek wordt een datamodel opgesteld dat de verbanden beschrijft tussen de verschillende experimentele aspecten van naald-weefsel-interactie. Dit datamodel vormt de blauwdruk voor een database met empirische bevindingen ten aanzien van naald-weefselinteractie.

Het tweede deel van het proefschrift beschrijft twee voorbeelden van relatief goed gecontroleerde experimenten met kunstmatige weefsels. Deze voorbeelden laten zien wat er gebeurt aan de punt van de naald tijdens het doorprikken van een kunststof membraan. Het eerste voorbeeld behandelt het gebruik van high-speed video om verband te leggen tussen de axiale kracht en de geometrie van de punt. Het tweede onderzoekt de invloed van coating op de axiale kracht.

Het laatste deel van het proefschrift presenteert twee voorbeelden van experimenten met biologische weefsels. Het eerste voorbeeld is gericht op het karakteriseren van de krachten die optreden tijdens het prikken in de nier van een menselijk kadaver. Het tweede richt zich op een meer gedetailleerde karakterisering van de krachten tijdens het prikken in geïsoleerde varkensnieren. In beide experimenten wordt gebruik gemaakt van echovisualisatie om de positie van de naald ten opzichte van het weefsel te bepalen.

Het proefschrift draagt op verschillende manieren bij aan het veld van de naald-weefselinteractiemechanica. Het levert een overzicht van beschikbare kennis op het vlak van de interactiekrachten en het voorziet in een kader voor het structureren en uitbreiden van deze kennis. Deze uitbreiding wordt ook in de praktijk gebracht door te illustreren hoe de interactiekrachten beïnvloed worden door factoren zoals hergebruik, coating, en randvoorwaarden voor kunstmatige membranen. Daarnaast geeft het proefschrift een eerste indruk van de variabiliteit die optreedt bij het prikken in de nier van een menselijk kadaver en presenteert het een multivariaat stochastisch model van de prikkrachten in varkensnieren, dat onder andere gebruikt kan worden in priksimulaties. De belangrijkste bijdrage bestaat echter uit een set gereedschappen voor het verzamelen, analyseren en verspreiden van experimentele naald-weefselinteractiedata.

Contents

1	Introduction	1
1.1	Background	1
1.1.1	Basic anatomy of a needle	1
1.1.2	Why study needle-tissue interaction?	2
1.1.3	A very short word on needle-tissue interaction models	4
1.2	Problem statement	4
1.3	Goal of the thesis	5
1.4	Approach and thesis outline	5
2	A Survey of Experimental Data	7
2.1	Introduction	7
2.1.1	Background	7
2.1.2	Related work	8
2.1.3	Aim	8
2.1.4	Survey method	8
2.2	Axial Force Characteristics	9
2.2.1	Magnitude of axial forces	9
2.2.2	Needle insertion phases	10
2.2.3	Components of the axial force	13
2.3	Influence of Insertion Method	17
2.3.1	Manual vs automated insertion	17
2.3.2	Insertion velocity	18
2.3.3	Axial rotation	23
2.3.4	Insertion location and direction	24
2.3.5	Bevel orientation	25
2.4	Influence of Needle Characteristics	25
2.4.1	Diameter	26
2.4.2	Tip type	27
2.4.3	Sharpness	30
2.4.4	Lubrication	30
2.5	Influence of Tissue Characteristics	31
2.5.1	Artificial vs Biological	31
2.5.2	Human tissue vs other biological tissue	32

2.5.3	Live vs dead biological tissue	33
2.5.4	Decay time	33
2.5.5	Freezing and tissue hydration	34
2.6	Discussion	34
2.6.1	Axial force characteristics	34
2.6.2	Insertion method	35
2.6.3	Needle characteristics	35
2.6.4	Tissue characteristics	36
2.7	Conclusion	36
3	A data model for needle-tissue interaction experiments	39
3.1	Introduction	39
3.1.1	Structured representation of experiments	39
3.1.2	Relational data model basics	40
3.1.3	Relational data model diagrams	41
3.2	A relational data model for needle-tissue interaction research . . .	41
3.2.1	Experiment	42
3.2.2	Researcher	42
3.2.3	Publication	43
3.2.4	Condition	43
3.2.5	Factor	46
3.2.6	Specimen	46
3.2.7	Needle	47
3.2.8	Equipment and instrumentation	47
3.2.9	Unit type	48
3.3	Model implementation	48
3.3.1	Data model implementation	48
3.3.2	Adding data	48
3.3.3	Retrieving data	49
3.4	Discussion	49
4	Observations of membrane puncture	51
4.1	Introduction	51
4.1.1	Background	51
4.1.2	Problem statement	52
4.1.3	Related work	52
4.1.4	Research question	52
4.1.5	Approach	53
4.2	Materials and methods	53
4.2.1	Instrumentation	53
4.2.2	Specimens	54
4.2.3	Specimen support	55
4.2.4	Needles	55
4.2.5	Insertion parameters	55
4.2.6	Protocol	56

4.2.7	Experimental design	56
4.2.8	Data analysis	57
4.3	Results	58
4.3.1	Microscopic observations	58
4.3.2	High speed video footage, membrane displacement, and force response	58
4.3.3	Basic rules for the identification of characteristic points on the force response curve	62
4.3.4	Evaluation of the metrics	64
4.4	Discussion	65
4.4.1	Interpretation of the results	65
4.4.2	Limitations	67
4.4.3	Conclusion	67
5	The effects of needle coating on puncture force	69
5.1	Introduction	69
5.1.1	Background	69
5.1.2	Problem statement	69
5.1.3	Related work	70
5.1.4	Objective	70
5.1.5	Approach	71
5.2	Materials and Methods	71
5.2.1	Equipment and instrumentation	71
5.2.2	Specimens	71
5.2.3	Needles	71
5.2.4	Surface treatment	72
5.2.5	Insertion parameters	72
5.2.6	Experimental design	72
5.2.7	Analysis	73
5.3	Results	74
5.4	Discussion	79
5.4.1	Interpretation	79
5.4.2	Limitations	79
5.4.3	Conclusion	80
6	Kidney puncture forces in a human cadaver	81
6.1	Introduction	81
6.1.1	Background	81
6.1.2	Problem statement	82
6.1.3	Related work	83
6.1.4	Research Objective	83
6.2	Materials and Methods	83
6.2.1	Materials	83
6.2.2	Methods	86
6.3	Results	89

6.3.1	Ultrasound	89
6.3.2	Force-position history	90
6.3.3	Pre-processing	93
6.3.4	Evaluation of metrics	93
6.4	Discussion	98
6.4.1	Interpretation of the results	98
6.4.2	Limitations of the study	100
6.4.3	Conclusion and recommendations	100
7	Stochastic modeling of kidney puncture forces	103
7.1	Introduction	103
7.1.1	Background	103
7.1.2	Problem description	104
7.1.3	Related work	104
7.1.4	Research objective and approach	105
7.2	Materials and Methods	106
7.2.1	Measurement protocol and experimental conditions	106
7.2.2	Test specimens	106
7.2.3	Instrumentation	106
7.2.4	Needle characteristics	107
7.2.5	Force signal processing	109
7.2.6	Ultrasound signal processing	110
7.2.7	Peak classification	111
7.2.8	Definition of force metrics	111
7.2.9	Stochastic modeling of the force metrics	111
7.2.10	Simulation of the force metrics	113
7.3	Results	113
7.3.1	Raw data	113
7.3.2	Force metrics	115
7.3.3	Stochastic models of the force metrics	116
7.3.4	Simulation results	116
7.4	Discussion	121
7.4.1	Summary of main results	121
7.4.2	Interpretation of main results	122
7.4.3	Limitations	123
7.4.4	Conclusion	123
8	Discussion	125
8.1	A broader scope	125
8.1.1	Measuring is essential for a proper understanding	125
8.1.2	Little is known from the literature	126
8.1.3	Synthesis of knowledge requires structure	127
8.1.4	Direct visual observation is essential for selection of metrics	128
8.1.5	Lubrication influences the force metrics	129
8.1.6	Kidneys in human cadavers	130

8.1.7	Isolated porcine kidneys	132
8.2	General limitations of the work	133
8.3	Conclusion	135
8.3.1	Accomplishments	135
8.3.2	Recommendations	136
8.3.3	Final comment	137

Chapter 1

Introduction

If it disagrees with experiment, it's wrong. That's all there is to it. —Richard P. Feynman, 1964

1.1 Background

Although they may not be very popular among patients, medical needles are exceptionally versatile instruments that have found their way into virtually every clinical intervention imaginable. However, despite their versatility, needles can be very difficult to use, and there is much room for improvement. To enable such improvement, it is necessary to understand how needles interact with tissue. This thesis deals with the experimental study of needle-tissue interaction.

1.1.1 Basic anatomy of a needle

The thesis focuses on hollow needles¹ such as those depicted in Figures 1.1 and 1.2. These needles are typically characterized by their tip shape, cannula length, and outer diameter. Needle diameter is expressed using the Stubs wire gauge system [1] and standard sizes range from 10G (3.4mm) to 35G (0.2mm) according to ISO-9626 [2].²

Before proceeding it is important to discuss some jargon. Figure 1.1 presents a basic overview of needle components, which are defined below.

Needle: A long slender instrument used to perform medical procedures, typically comprising a hub, cannula, and (optional) stylet.

Hub: The proximal end of the needle, specifically that part by which the clinician holds the needle, typically made of plastic and equipped

¹This excludes the class of suture needles (also called surgical needles).

²Other useful standards related to needles are DIN-13097 [3] (hypodermic needle tip geometry and testing), ISO-7864 [4] (sterile hypodermic needles), and ISO-11608-2 [5] (needle based injection systems for medical use).

with one or more interfaces for the attachment of syringes or tubes (Luer interface).

Cannula: A long slender tube, typically made of stainless steel, that facilitates passage of a medium from the hub to the tip and vice versa, and that transfers loads between the hub and the tip.

Lumen: The hollow space inside the cannula.

Stylet: A long slender solid, made of plastic or stainless steel, that fills the lumen. We distinguish between cutting stylets that protrude from the cannula, and non-cutting stylets that are flush with the cannula.

Tip: The distal end of the needle, specifically that part for which the shape of the cross-section³ varies along the longitudinal axis of the (undeformed) needle. Note that the tip is often an integral part of the cannula and may include part of the stylet (as in Figure 1.1).

Point: The distal end of the tip, specifically that point at which the cross-sectional area becomes zero.

Shaft: That part of the cannula that does not belong to the tip, i.e. that part for which the cross-section shape is constant.

An extensive glossary is provided by Kucklick [1], who also discusses needle materials and manufacturing methods. The precise definitions of tip, point, and shaft given above differ from those found in the literature, but are more convenient for the discussion of needle-tissue interaction forces.

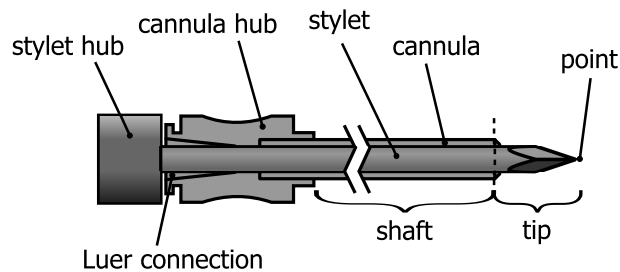


Figure 1.1: Basic anatomy of a needle with cutting stylet (partial cross-section). Note that the tip comprises part of the stylet and part of the cannula.

1.1.2 Why study needle-tissue interaction?

The most common type of needle is the hypodermic needle, which is used to reach superficial targets, just under the skin. However, as illustrated by Figure

³perpendicular to the longitudinal axis of the undeformed needle

1.2, there are many other types of needle that can be used for a great variety of complicated interventions such as regional anesthesia, biopsy, catheterization, ablation, and other procedures. These needles allow us to reach deep inside the body with a minimal amount of tissue damage, but this comes at the cost of limited navigation ability. As a result, the success of a needle intervention depends heavily on the clinician's skill and knowledge.

The ability to navigate is limited by two factors: Firstly there is no direct view of the needle tip and surrounding tissue, which makes it difficult to know the position of the tip in relation to relevant anatomy. Secondly, the needle can only be controlled by applying loads to the part that is outside the body, which makes it difficult to steer the needle towards a desired position inside the body, especially for long, slender needles. These issues limit the placement accuracy, thereby reducing treatment efficacy and increasing the risk of inadvertent tissue damage.

The navigation problem can be dealt with in different ways, for example by focusing on improved training facilities for clinicians, improved information (better visualization, needle-based sensors), designing needle geometries that allow better manual control, developing steering mechanisms and path planning methods, or even by fully automating the needle insertion process [6–8].

These approaches all rely on a proper understanding of the mechanical interaction between needle and soft-tissue.

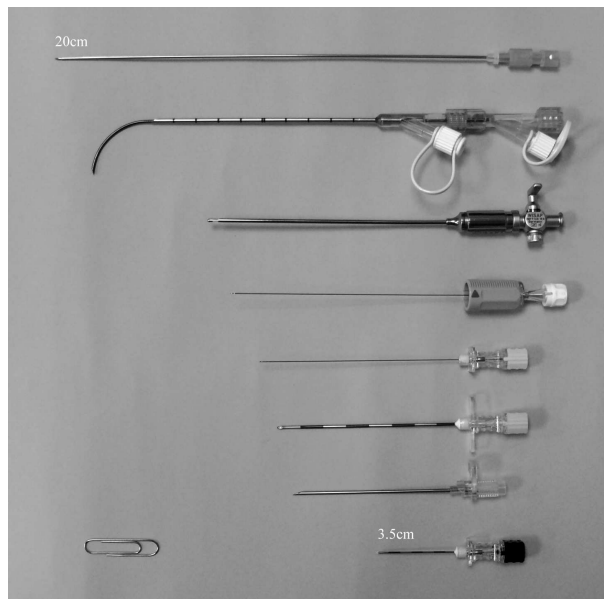


Figure 1.2: A random assortment of needles for a variety of interventions, ranging from intravenous cannulation to kidney catheterization.

1.1.3 A very short word on needle-tissue interaction models

Ideally, a proper understanding of needle-tissue interaction mechanics should follow from the development and refinement of theoretical models based on experimental observation. Such theoretical models may range from very general descriptive models that are mainly phenomenological in nature (top-down approach) to very detailed models based on first-principles (bottom-up approach).

A detailed model of needle-tissue interaction would typically describe the deformation of the needle due to loads exerted by the tissue, and, conversely, the deformation of the tissue due to loads exerted by the needle. We refer to these loads, acting on the interface between needle and tissue, as interaction loads. On a more detailed level, the interaction loads are governed (and limited) by phenomena from the fields of contact mechanics (including friction mechanics), and fracture mechanics.

The development of theoretical models has received a lot of attention in the literature [6, 7, 9, 10], and some experimental work has been done in conjunction. However, as shown e.g. by Misra et al. [9] in their extensive review of continuum mechanics-based tool-tissue interaction modeling, our inability to collect useful and reliable experimental data remains an important obstacle to the development of useful models.

1.2 Problem statement

In testing the agreement between theory and experiment, one usually presupposes that the experiment represents something close to the truth. Whether this assumption is accurate depends on the ability to control the experiment and to observe its outcome. Shortcomings in these respects will introduce discrepancies that may invalidate the test itself. This implies that disagreement between theory and observation does not necessarily invalidate the theory, nor does agreement necessarily validate the theory [11]. Thus, it is imperative that we understand how to control needle-tissue interaction experiments and measure their results.

Perhaps the most important challenge in this respect is dealing with biological soft-tissue. These tissues often show effects of preconditioning (history dependent behavior), hysteresis (under cyclic loading), relaxation (reduction of stress under constant strain), creep (increase of strain under constant stress), and nonlinear stress-strain relationships. Moreover, soft-tissues are composite structures, which implies that their properties depend not only on the materials involved but also on the composition and structure in which these materials are arranged. Thus, biological soft-tissues are typically inhomogeneous (properties depend on location) and anisotropic (properties depend on orientation). To complicate matters even more, soft-tissue naturally exists in a living state, which implies that its properties are time variant.

However, even when dealing with artificial materials, there are many factors in a needle-tissue interaction experiment that are difficult to control but may have

a large influence on the outcome. One example is the question of how to control specimen boundary conditions.

Whether using biological or artificial specimens, the interaction process is difficult to observe visually, because the action is obscured by both needle and tissue. Instead we need to rely on measurements of external reaction loads and crude measurements of local tissue displacement, in combination with theoretical models, to infer what is actually taking place at the needle tip.

Finally, due to the large variety of dependent and independent factors involved in these experiments, it is difficult to keep track of experimental data and conditions tested.

Thus, to obtain reliable experimental data that can be used to test and improve theories of needle-tissue interaction mechanics, it is imperative that we learn how to control experimental conditions and interpret experimental data.

1.3 Goal of the thesis

The goal of this thesis is to provide insight into needle-tissue interaction mechanics based on experimental observation. This involves the development of a structured approach to experimentation, storage of data, and analysis of data.

1.4 Approach and thesis outline

The current thesis focuses on an aspect of needle-tissue interaction that is relatively easy to measure, namely the axial component of the external force acting on the needle during interaction with (soft-)tissue. To make sense of this axial force, it is necessary to relate it to the position of the needle relative to the surrounding tissue.

The approach adopted here to study needle-tissue interaction is mostly phenomenological. We consider what is already known, construct a general framework to facilitate the storage of experimental data, and then proceed by investigating some specific questions that have not been answered yet in the literature. To this end we consider experiments with artificial materials, in relatively well controlled environments, and experiments with biological tissue, which are much more difficult to control and analyze. An outline of the thesis is sketched below.

Chapter 2 presents a survey of literature related to needle-tissue interaction force measurements. The intention of this survey is to gather existing experimental evidence regarding the influence of different factors, such as needle type, tissue type, insertion speed, etc. on the axial force.

Chapter 3 presents a data model that describes the interrelations between the different aspects of needle-tissue interaction experiments, based on findings from the literature survey. This data model enables the detailed encoding of experimental equipment, conditions, design, and results, and forms the basis of a

database for experimental needle-tissue interaction data.

Chapter 4 describes what actually happens at the tip of a needle during puncture of an artificial membrane. The experiment presented involves the use of high speed video to investigate the relation between axial force and needle tip geometry.

Chapter 5 presents a follow-up study that investigates the influence of needle coating (lubrication) on the axial force during membrane puncture.

Chapter 6 takes us from the well controlled artificial environment into that of the human body. An exploratory study is presented that is aimed at the characterization of forces during needle insertion into the kidney of a human cadaver. This is done with the help of synchronized ultrasound visualization.

Chapter 7 describes a study of needle insertion into isolated porcine kidneys, intended to achieve a more detailed characterization of forces for different anatomical structures inside the kidney. This experiment uses synchronized ultrasound visualization with the ultrasound probe moving along with the needle.

Chapter 8 finally puts everything in perspective.

Chapter 2

A Survey of Experimental Data

(This chapter is an adaptation of [12], reprinted with permission)

2.1 Introduction

Needles are common medical tools, yet considerable skill is required to use them effectively and safely. Developments in the fields of medical simulation and robotics, aimed at improving needle intervention efficacy, require a thorough understanding of needle-tissue interaction mechanics.

2.1.1 Background

The development of theoretical models that describe the interaction between needle and tissue, in terms of loads and displacements, has received a lot of attention in recent years (e.g. [6, 7, 9]). These models form an essential component of virtual-reality simulators with force feedback, intended for skills training. Moreover, they are indispensable for the development of new types of needles and needle-insertion robots.

Validation of these theoretical models is essential, especially for medical applications, and this requires reliable experimental data. However, for both practical and ethical reasons, experimental data from needle insertions into living biological tissue are rather difficult to come by.

To provide a starting point for researchers in this field, we have performed a survey of the experimental data available in literature.

2.1.2 Related work

Other researchers have reviewed the theory behind mathematical models for needle-tissue interaction, but none of them focused explicitly on experimental data.

Abolhassani et al. [6] provide an overview of research related to needle insertion into soft-tissue with a broad scope, covering topics such as needle modeling, tissue modeling, and the application of these models to automated needle insertion.

Misra et al. [9] present an extensive review of literature related to the modeling of tool-tissue interaction for use in virtual-reality simulation. Topics covered include continuum mechanics and finite element methods, and their application to modeling of non-invasive as well as invasive tool-tissue interaction. Experimental methods for parameter identification and validation are also discussed briefly.

Cowan et al. [7] provide a thorough discussion of needle-tissue interaction models, path planning methods and imaging options in relation to robotic needle steering, but experimental findings receive little attention.

The survey of force sensing techniques presented by Trejos et al. [13], although mainly aimed at general minimally invasive surgery, helps to clarify the difficulties encountered when measuring instrument-tissue interaction forces in a clinical setting.

The current work is different from these reviews because it focuses solely on collecting and interpreting experimental data available in literature.

2.1.3 Aim

The mechanical interaction between needle and biological tissue is influenced by a great number of variables, e.g. related to insertion method, needle characteristics, and tissue characteristics. The aim of this survey is to collect experimental data that show *how* the axial needle force is influenced by these variables, and to guide the reader to the relevant literature. In addition, quantitative force information is collected and areas open for further research are identified.

2.1.4 Survey method

The survey is limited to those papers that present original force measurement data obtained during insertion of a needle (or similar tool) into any kind of soft material, either artificial or biological, living or dead.

The search was conducted during the last months of 2010, using the PubMed database (medical literature), the Scitopia.org search engine (technical literature), and Google Scholar.¹

¹A typical search string is: *(needle* OR cannula) AND (force* OR haptic* OR resistance OR friction) AND (measur* OR instrument*) AND (insert* OR advanc* OR displace* OR position* OR introduc* OR punctur* OR interact*)*

Table 2.1: Classification of papers by information content, indicating usefulness for the current survey

Class	Criteria	References
C3	methods clear, data presented with variability and sample size, and some form of statistical analysis	[14]-[25]
C2	as C3, but no statistical analysis	[26]-[39]
C1	as C2, but data are presented without indication of variability or sample size	[40]-[82]
C0	as C1, but description of methods not clear or incomplete (e.g. needle diameter not mentioned)	[83]-[112]

Relevant papers were selected by considering title and abstract, and subsequently by examining tables and figures for useful information. In addition, references found in these papers were investigated. This resulted in a total of 99 papers.

Details of experimental methods and results were extracted manually and stored in a custom database. Using this database, the papers were objectively classified into four categories as shown in Table 2.1 (based purely on information content). A paper with C3 classification is more likely to be useful for the current survey than one with classification C0. However, it is stressed here that this classification is not a measure of quality: a C0 paper can still be of high quality.

The survey is structured in such a way that relevant literature is discussed by topic. The intention is to allow the reader to quickly skip to the topic of interest without having to read the entire survey.

2.2 Axial Force Characteristics

A typical medical needle consists of a slender stainless steel tube or ‘cannula’, with a plastic hub on one end and a sharp tip on the other. The hollow space inside the cannula is called the lumen. The tip is the part of the cannula that has varying cross-section, whereas the shaft has constant cross-section.

Axial force is defined here as the force acting on the needle hub in the direction of insertion. As will be discussed in the following sections, the axial force can consist of puncture force, cutting force, and friction force.

2.2.1 Magnitude of axial forces

The order-of-magnitude of needle-tissue interaction forces represents an important practical consideration for many applications. However, due to the large number of variables involved in needle tissue interaction, and the large variety

Table 2.2: Maximum axial force values found in all papers

Description	n	Median	Min-Max
-	[-]	[N]	[N]
total axial force	63	5.0	0.00004 ^[58] -92.0 ^[27]
puncture force	24	1.22	0.0005 ^[110] -19.2 ^[72]
cutting force	10	0.95	0.05 ^[39] -1.3 ^[18]
friction force	10	1.0	0.15 ^[33] -2.8 ^[68]

of experimental approaches, it is difficult to give a comprehensive overview of all the forces encountered.

To provide at least some indication of the order-of-magnitude of forces typically encountered, the medians and extrema of the maximum axial forces found in all papers (irrespective of experimental conditions etc.) are presented in Table 2.2. The large range of forces is mainly due to atypical needle diameters ($30\mu m$ [58] to $11mm$ [27]). The median is used because it is insensitive to these extrema.

2.2.2 Needle insertion phases

During needle insertion into soft-tissue, the motion of the needle relative to the surrounding tissue needs to be considered, rather than the absolute motion of the needle. By looking at the position of a needle relative to a tissue boundary, it is possible to distinguish three basic phases of interaction, as depicted in Figure 2.1. These phases may be repeated when the needle encounters internal structures or variations in tissue properties. Similar penetration phases are described in the German industry standard for hypodermic needle tips, DIN 13097.

Phase 1: Boundary displacement

The first phase (Figure 2.1b) starts when the needle comes into contact with the tissue boundary, and ends when the tissue boundary is breached. The actual breaching of the boundary is referred to as the puncture event.

During the boundary displacement phase, the tissue boundary deflects under the influence of the load applied by the needle tip, but the needle tip does not penetrate the tissue (the boundary moves along with the needle). This phenomenon is known as “tenting” [60], [63].

A typical force-time curve is shown in Figure 2.2. This figure was borrowed from Kobayashi et al. [30], who specifically measured the tissue displacement and investigated relative velocity during insertion.

This figure clearly shows a non-linear increase in force during the boundary displacement phase (relative velocity is zero). The shape of this curve is reminiscent of the load increase during thin-membrane displacement as found by e.g. Selvadurai [113]. Similar non-linear behavior of the axial force during boundary displacement is found in nearly all studies included in this survey.

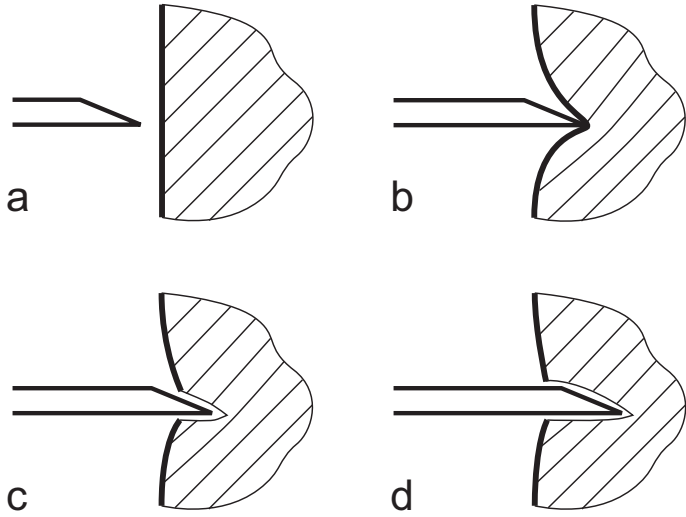


Figure 2.1: Basic phases in needle insertion: a. no interaction; b. boundary displacement; c. tip insertion; d. tip and shaft insertion

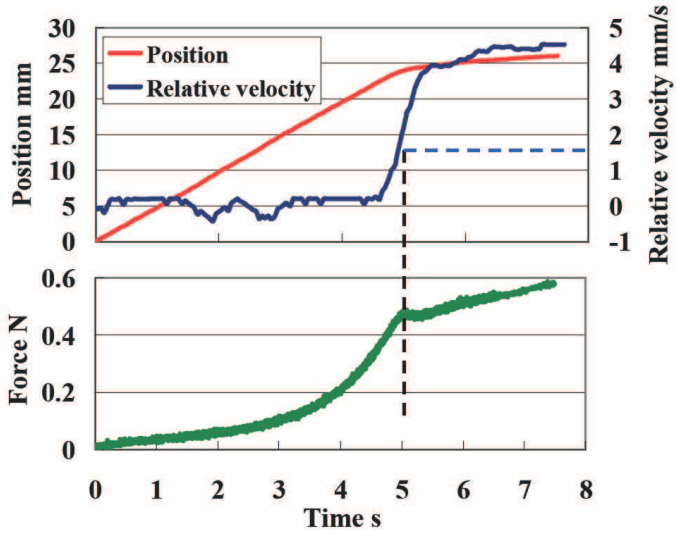


Figure 2.2: Distinction between the pre-puncture and post-puncture phases based on relative velocity, for a 17G beveled needle inserted into porcine liver ex vivo, at 5mm/s [30]. Position is that of the tissue boundary. (©2009 IEEE)

At some point, the relative velocity starts to increase, which indicates that

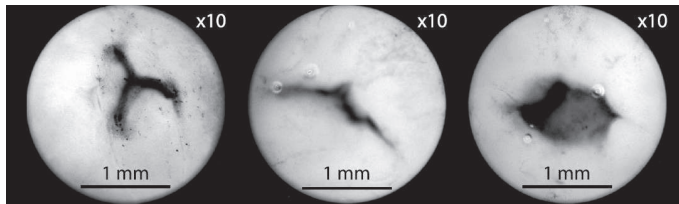


Figure 2.3: Crack shapes in fresh porcine liver. Left-to-right: triangular diamond tip, small bevel angle, very large bevel angle. (With kind permission from Springer Science+Business Media: [46] Fig. 3)

puncture has occurred. The puncture event and the processes at work during the post-puncture phases (phases 2 and 3) can be described using fracture mechanics theory, as shown by Mahvash and Dupont [64], Nguyen et al. [72], Shergold and Fleck [80], Azar and Hayward [46], and Mahvash and Hayward [114].

As the needle displaces the tissue boundary, the load at the needle point increases, as do the stresses in the tissue surrounding the contact area. Once these stresses exceed a certain critical value, according to Kobayashi et al. [16], a crack will be initiated in the tissue and the needle will start to penetrate the tissue.

The work of Shergold and Fleck [80] and that of Azar and Hayward [46] suggests that the shape of this crack depends on the shape of the needle tip. A planar crack is initiated when using sharp bevel needles or conical needles. Diamond tips were found to create star shaped cracks, and needles with a very large bevel angle were found to create ring cracks, as illustrated by Figure 2.3. This result was found for artificial gels as well as for porcine skin and porcine liver *ex vivo*, and for human skin *in vivo*. Once a crack has been initiated, phase 2 commences.

Phase 2: Tip insertion

The second phase (Figure 2.1c) starts when the tissue boundary is breached, and ends when the tissue-boundary slides from the tip onto the shaft. During this phase, as the needle is advanced, the crack in the tissue-boundary is enlarged. The cut made by the sharp edges of the tip is wedged open by the increasing cross-sectional area of the tip, as described by e.g. Mueller [33].

The crack growth process can be either gradual, stable crack growth (cutting), or sudden, unstable crack growth (rupture), depending on the local properties of the tissue, such as rupture toughness (i.e. the work required to cut the tissue, per unit cross-section area), and on the amount of strain energy stored in the tissue due to deformation.

When a thin membrane is punctured, the amount of energy stored during the boundary displacement phase is often so large that rupture occurs (sudden crack extension). This results in a (relatively large) drop in force, as the accumulated strain energy is used to extend the crack (an irreversible process). Rupture continues until the strain energy levels become low enough for the crack extension

to proceed in a stable manner (i.e. cutting).

A needle traversing an internal tissue boundary can cause rupture when the toughness of the new tissue layer is significantly lower than that of the current tissue layer, according to Mahvash and Dupont [64].

The transition from tip to shaft may also give rise to an increase in axial force, due to the hole in the tissue boundary being wedged open. The magnitude of this effect depends on needle type, as will be discussed later.

Phase 3: Tip and shaft insertion

The third phase (Figure 2.1d) starts just after the transition from tip to shaft and ends when the needle is stopped or when a new (internal) tissue boundary is encountered. During this phase, the contact area between tip and tissue and the size of the hole at the boundary remain more or less constant. Only the contact area between shaft and tissue increases as the needle is advanced.

During this phase the needle is subject to cutting (or rupture) forces at the tip, and to a varying friction force that is due to the increasing contact area between shaft and tissue.

Hing et al. [28] found that the stable cutting force is more or less constant, in porcine liver *ex vivo*, with some fluctuations due to rupture (small internal puncture events), depending on the level of inhomogeneity of the tissue. These findings were based on 45 insertions of diamond tip needles at 13 mm/s. Results for a single insertion are depicted in Figure 2.4.

Their approach was based on the assumption that the axial force is composed of a cutting force and a friction force. Evidence in support of this assumption is discussed next.

2.2.3 Components of the axial force

Interaction between needle and tissue results in distributed loads along the needle-tissue interface, that is, along the contact area between needle and tissue, as depicted in Figure 2.5. These surface forces consist of normal and tangential tractions acting on the contact surface, as mentioned by e.g. [67, 105]. An important question is how these loads are distributed along the needle.

Since direct measurement of such a load distribution is practically impossible, indirect methods need to be used. This implies that one has to resort to the use of needle-tissue interaction models to reconstruct the load distribution along the needle based on external force measurements and tissue displacement measurements.

Artificial materials are generally easier to model than biological tissues, since the latter are composite structures and thus are inhomogeneous and anisotropic.

Load distribution in artificial materials

DiMaio and Salcudean [50, 51, 91] employed finite element (FE) models to ex-

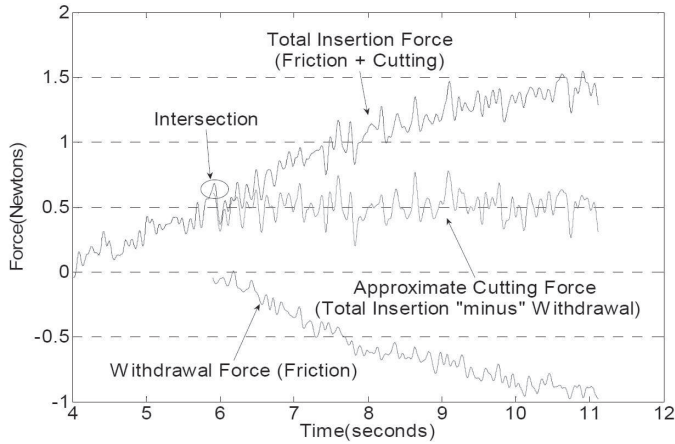


Figure 2.4: Cutting force estimation by subtracting withdrawal force from insertion force [28], for 18G diamond tip needle at 13mm/s in porcine liver ex vivo (©2006 IEEE)

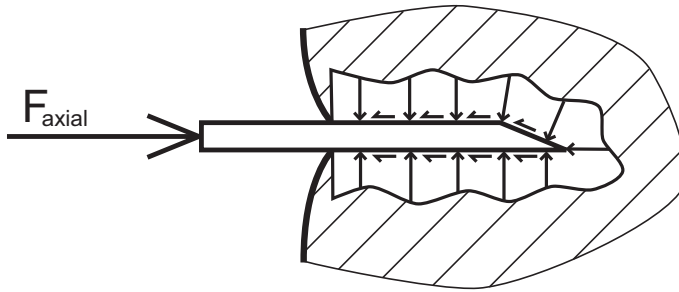


Figure 2.5: Axial force acting on the base of the needle and surface forces acting on the tip and on the part of the cannula inside the tissue. Forces and moments will typically act on the hub in all directions, but focus here is only on the axial force since this is considered the most important.

tract an approximate axial load distribution based on axial force measurements and tissue-displacement measurements in PVC phantoms. The load distribution along the needle was found to be largely uniform, with the exception of a peak near the tip, as depicted in Figure 2.6. Although no explanation is given for this peak, it is reasonable to assume that it is related to the mechanical processes at work near the tip (cutting/rupture). The large uniform part of the distribution is supposedly due to friction.

Dehghan et al. [88] used a three-parameter model (shaft height, peak height, peak width) to approximate that same distribution (Figure 2.6), and identified these parameters using a finite element approach similar to that of DiMaio and

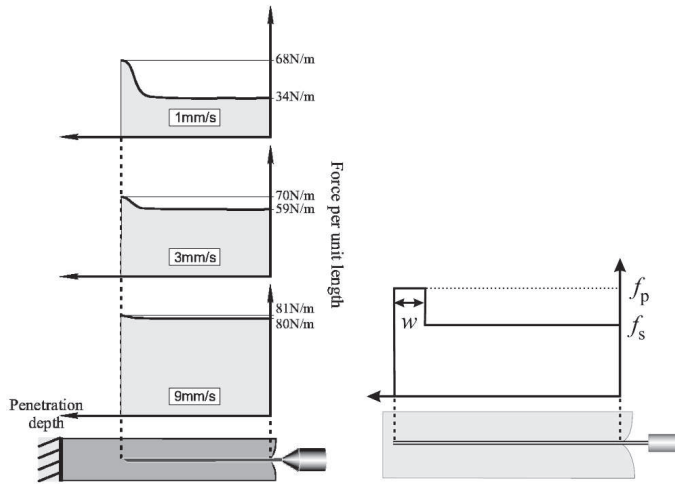


Figure 2.6: Distribution of axial load along a 17G Tuohy needle at different velocities in a PVC phantom [51] (©2003 IEEE), and the three-parameter model used by Dehghan et al. [88] to approximate this distribution, with peak width w , peak force density f_p and shaft force density f_s (With kind permission from Springer Science+Business Media: [88] Fig. 3b).

Salcudean [51]. The peak widths found for insertions into artificial phantom material are in the same order of magnitude as the needle tip length, which supports the assumption that the peak is due to the cutting process.

Crouch et al. [26], used a similar approach, based on a FE model and measurements of tissue displacement and force, to estimate the load distribution along an 18G diamond tip needle in a silicone gel. Their approach focused on the influence of needle velocity. The distribution shape was approximated using cubic splines and also shows a large uniform part together with a peak at the tip. A drop in force is observed, just behind the peak, but no explanation is given for this peculiarity.

The detailed distribution of loads along the tip of a beveled needle is investigated by Misra et al. [105], but they only consider transverse forces.

Note that a constant force density (force per unit length) along the cannula, i.e. a uniform load distribution, corresponds to a linear force-position relation with slope equal to the force density. This knowledge is useful when considering biological tissue.

Load distribution in biological tissue

In the aforementioned, the axial load distribution was found to be largely uniform when the needle is inserted into homogeneous isotropic artificial materials. The question now is whether this is also true for biological tissue.

The FE approach is not practical here, due to difficulties in modeling biological tissue and in measuring internal tissue displacement. However, if the load distribution does indeed remain uniform, this would result in a linear rise of friction force with insertion distance, or in a constant friction force if the contact area remains constant during insertion. In order to verify this, friction force needs to be measured somehow.

Different approaches can be adopted for measuring the friction force acting on a needle. For example, Hing et al. [28, 29] assume that the force during removal of the needle is due to friction only, thereby yielding a direct friction measurement. The resulting friction curve shown in Figure 2.4, for porcine liver, can be interpreted as approximately linear.

Another approach is to make sure that the needle tip is outside the tissue on the other side, thereby ensuring that the tip no longer interacts with the tissue and the force measured is only due to friction along the cannula. This method, in combination with unidirectional motion, is used by Abolhassani et al. [40] (turkey muscle), and Kobayashi et al. [30] (porcine liver), resulting in approximately constant friction force (as the contact area between needle and tissue remains constant).

The same approach is used by Simone and Okamura [81, 82], O'Leary et al. [73], and Okamura et al. [18] (bovine liver). Using bi-directional motion, they investigated of static as well as dynamic components of friction force.

Yet another approach is to measure the tip force and total force independently, as was done by Kataoka et al. [56] for a 17G diamond tip needle in canine prostate *ex vivo*. Their special measurement device allowed indirect determination of the friction component based on the assumption that total insertion force is the sum of tip force and friction force. Their results seem to indicate that, during the post-puncture insertion phases, friction force does indeed increase linearly with insertion distance. However, in their findings the (friction) force does not change sign during retraction, which undermines the credibility of the results.

The above findings suggest that axial load distribution along the needle is approximately uniform, not only for (homogeneous, isotropic) artificial materials, but also for the biological tissues investigated here.

In addition, force vs position diagrams presented by other authors, who did not explicitly measure friction, in many cases show an approximately linear rise in total force during the post-puncture phases. This too is consistent with the assumption that the total insertion force is composed of a constant force due to (quasi-steady) cutting and a linearly increasing force due to friction. Examples are provided by Meltsner et al. [66], Okamura et al. [18], O'Leary et al. [73], Podder et al. [74] for artificial materials, and by Healey et al. [52], Mahvash and Dupont [64], Kobayashi et al. [30] for biological tissue. Note that there are always some excursions due to e.g. internal puncture events, as found e.g. by Mahvash and Dupont [17] for porcine liver.

Note that Howard et al. [55], Jensen et al. [15] and Naemura [69] attempted to measure friction by inserting the needle twice at precisely the same location, under the assumption that all the cutting was done on the first insertion so that

the force during the second insertion would be entirely due to friction. This approach is questionable because there is no reason to assume that the needle tip will follow the exact same path without so much as scraping the tissue wall.

In short, three phases can be distinguished during basic needle insertion, based on the position of the tip relative to the tissue boundary. During insertion, crack initiation and stable or unstable crack extension processes occur, which are referred to as puncture, cutting, and rupture respectively. There are indications that cutting results in approximately constant force, and that the friction force increases approximately linearly with insertion depth in various materials. The following section investigates how the axial force components are influenced by insertion method.

2.3 Influence of Insertion Method

The interaction between needle and tissue is influenced by the way the needle is inserted. For example, manual insertion will yield different results than automated insertion. Likewise, force may be influenced by insertion velocity, axial rotation during insertion, location and direction of insertion, and by bevel orientation during insertion.

2.3.1 Manual vs automated insertion

During clinical procedures, the clinician, needle and patient are all part of a complex dynamical system with many interactions. This means that there are many potential confounding factors.

To illustrate this point, an example of a force vs position diagram for manual needle insertion during a clinical procedure and the corresponding velocity vs position diagram are depicted in Figure 2.7 [75].

Obviously, the velocity varies tremendously throughout the procedure, but it is not known whether this is deliberate, or if it is a result of the interaction between needle and tissue, or perhaps both. This makes interpretation of the forces difficult.

If a haptic simulator were developed for this procedure, the interaction between trainee and simulator would have to result in force and velocity characteristics like those presented in Figure 2.7. On the other hand, for the systematic investigation of needle-tissue interaction, experiments at constant velocity would be preferable.

A comparison between robotic insertion and manual insertion, both attempting to maintain the same constant velocity, is found in Figure 2.8 [75]. The inability of the human to maintain a desired constant velocity during manual insertion is evident from this figure. This emphasizes the necessity of using robotic insertion devices to ensure controlled experimental circumstances.

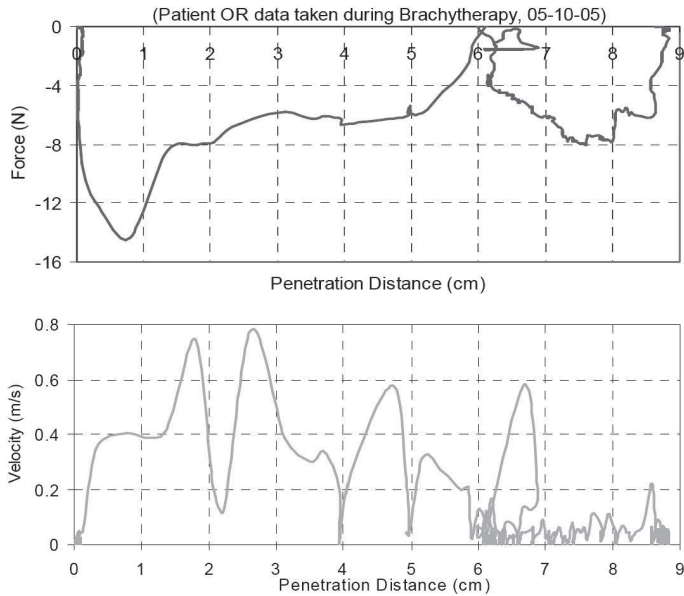


Figure 2.7: Force and velocity vs penetration distance measured during a clinical brachytherapy procedure [75] (©2005 IEEE). The needle seems to be inserted in short bursts.

2.3.2 Insertion velocity

The velocities encountered during actual clinical procedures may be relevant when investigating the influence of insertion velocity on axial force.

Insertion velocity during clinical procedures

A limited amount of information was found concerning typical velocities during clinical procedures.

Healey et al. [52] mention a speed of $500\text{mm}/\text{min}$ ($8.3\text{mm}/\text{s}$) as an approximation of the speed of needle insertion during interventional radiology procedures, but no source is provided. Hiemenz et al. [95] mention a video observation study of 20 epidural procedures which showed the insertion speed to range from $0.4\text{mm}/\text{s}$ to $10\text{mm}/\text{s}$.

Abolhassani et al. [42] consider the range from $1\text{mm}/\text{s}$ to $20\text{mm}/\text{s}$ to be representative for prostate brachytherapy, based on feedback of physicians. Podder et al. [20, 35, 75] measured the velocity during more than 25 actual prostate brachytherapy procedures and found *peak* velocities in the order of $1000\text{mm}/\text{s}$, which is two orders-of-magnitude larger. This may seem strange at first, but it is not uncommon in clinical practice to insert the needle in short bursts, and Figure 2.7 [75] shows that mean velocity during the initial phase of the insertion was

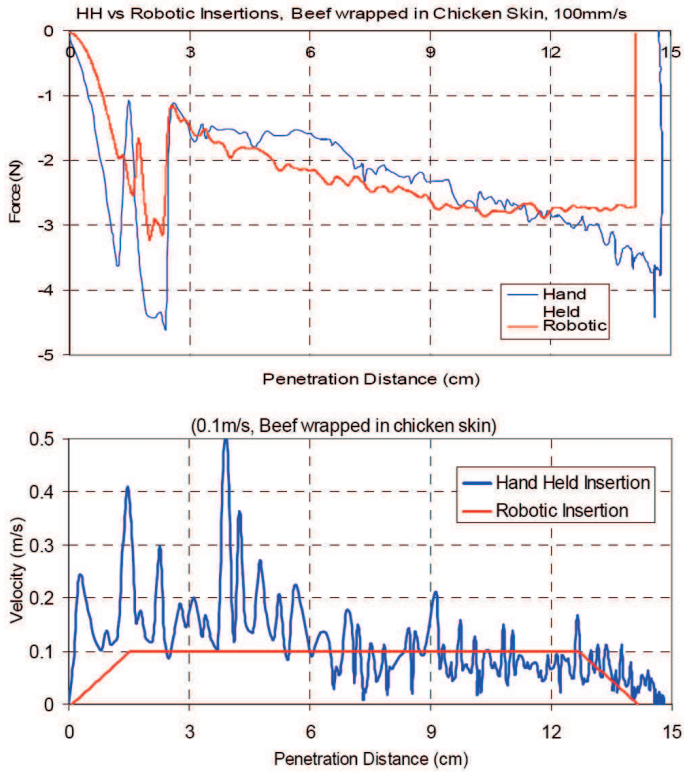


Figure 2.8: The result of trying to maintain a constant velocity during manual (hand held) insertion and during robotic insertion into beef wrapped in chicken skin (average of five insertions at different locations) as presented by Podder et al. [75] (©2005 IEEE)

in the order of 100mm/s , whereas during the final approach, mean velocity was reduced to the order of 1mm/s .

Whether or not based on these data, the majority of experiments included in this survey were performed at constant velocities in the order of 1mm/s to 10mm/s . Note that nearly all authors consider absolute needle insertion velocity, instead of that relative to tissue motion. This is not surprising given the practical difficulties in measuring relative motion.

In light of the differences between artificial materials and biological tissue, it is to be expected that velocity effects differ between the two types of material.

Velocity effects in artificial phantom materials

Five papers specifically investigated velocity effects during needle insertion into artificial phantom materials and presented results accordingly [26, 51, 66, 70, 74].

The latter considered the range from 5mm/s to 200mm/s , whereas the others all used velocities in the range from 1mm/s to 20mm/s .

Crouch et al. [26] considered insertion of an 18G diamond tip needle into silicone gel at velocities of 3mm/s to 21mm/s in steps of 3, with video based tissue deformation tracking. They found a logarithmic relation between insertion force (at a fixed depth) and insertion velocity and a similar relation for the slope of the force-position curve (both increase with speed).

DiMaio and Salcudean [51] show that insertion speed influences the load distribution along the shaft (shaft force density), as depicted in Figure 2.6. For a 17G Tuohy needle in PVC gel, not only does the total force (i.e. total area under the distribution curve) increase with speed, but the peak in the distribution becomes smaller and disappears altogether at 9mm/s , resulting in a fully uniform distribution. Thus, although cutting forces increase slightly with speed, friction forces increase much faster with speed and become dominant at higher speeds. The relation between shaft force density and velocity resembles the relation found for the total force vs velocity by Crouch et al. [26].

Meltsner et al. [66] investigated the effect of needle insertion velocity on insertion force for both rotating needles and non-rotating needles. Insertions of 17G bevel needles and conical needles into porcine gelatin at 5 to 20mm/s (non-rotating) showed an increased slope of the force vs position curve. The same trend appears to hold for rotating needles up to 5rpm, although overall slopes are lower here.

Podder et al. [74] investigated the effects of velocity on insertion force and tissue deflection, by inserting 18G diamond tip needles into PVC gel under fluoroscopic imaging. Axial velocities of 5 to 200mm/s were considered, also in combination with rotational velocities. The axial force vs position curves for the non-rotating case clearly indicate an increase in slope with increasing velocity. This effect seems to persist if the needle is rotated ($< 5\text{Hz}$) during insertion.

Naemura et al. [70] investigated the effect of tip shape on the slope of the force-position curve just after puncture (force drop), during insertion of an 18G Tuohy needle through silicone rubber membranes at 2 to 8mm/s . No clear effect of velocity was observed.

In short, axial force in artificial materials, like PVC, silicone, or porcine gel, increases almost linearly with position. The slope of the force-position curve also increases (non-linearly) with velocity, suggesting an increase in friction.

Velocity effects in biological tissue

Eleven papers examine velocity effects during needle insertion into biological tissue [14–17, 28, 30, 42, 53, 64, 66, 85]. Three of those, viz. [17, 53, 64], considered velocities larger than 25mm/s (up to 250mm/s).

Brett et al. [85] inserted Tuohy needles (unknown size) into porcine ligamentum flavum (2-5hrs old) at 0.83 to 2.50mm/s . Results indicate a decrease in puncture force with increasing velocity, but sample size is unknown. The puncture

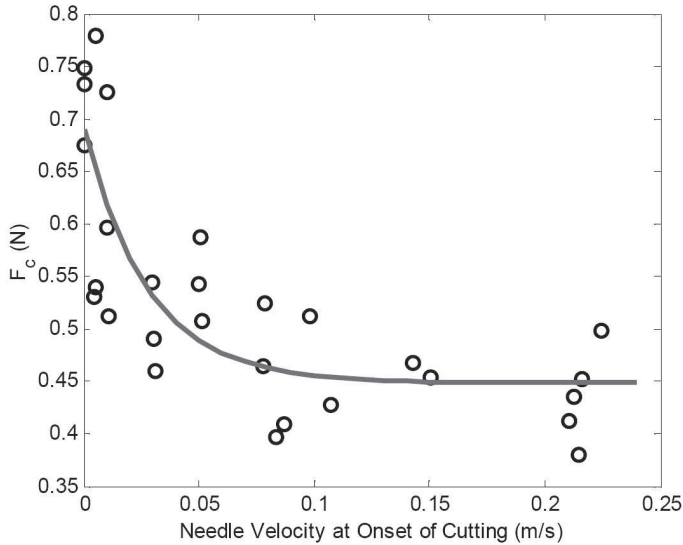


Figure 2.9: Force required to initiate cutting (i.e. puncture force), as a function of insertion velocity, using a 19G diamond tip needle in porcine heart tissue ex vivo ($n = 28$) as presented by Heverly and Dupont [53] (©2005 IEEE)

forces presented here are one order-of-magnitude higher than most of the other forces in this survey.

Heverly and Dupont [53] inserted a 19G diamond tip needle into porcine heart (epicardium and myocardium), ex vivo, at velocities between 5mm/s and 250mm/s . In the epicardial layer they found a decrease in puncture force (force required to initiate cutting) with velocity up to 75mm/s , and velocity independence at higher speeds, as depicted in Figure 2.9. It is concluded that cutting force and tissue displacement can be minimized by maximizing velocity.

Mahvash and Dupont [64] conclude that both puncture force and tissue displacement at the moment of puncture decrease with increasing velocity. These conclusions are based on insertions of a 19G diamond tip needle into porcine heart tissue, at speeds of 1 to 100mm/s (five insertions per velocity). The difference in mean puncture force at 50mm/s and 100mm/s is very small compared to the standard deviation.

Mahvash and Dupont [17] investigated the effect of insertion velocity on puncture force for 19G diamond-tip trocar needles and 18G beveled needles in porcine heart muscle, at speeds ranging from 1mm/s to 250mm/s . The results, based on 10 insertions per velocity, again show a decrease in puncture force with increasing velocity up to approximately 50mm/s , as depicted in Figure 2.10. At higher velocities the puncture force appears to remain constant. This trend holds for both needle types and is supported by statistical analysis.

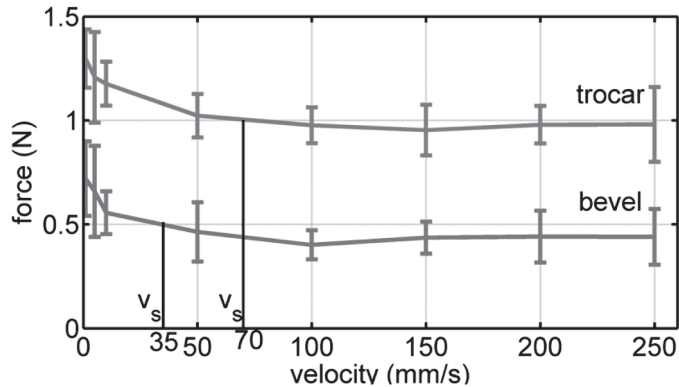


Figure 2.10: Mean peak axial force, with standard deviation ($n=10$), measured during insertion of 19G diamond tip trocar needles and 18G beveled needles into porcine heart [17] (©2010 IEEE)

Hing et al. [28, 29] investigated the insertion of 18G diamond tip needles into three different porcine liver samples, at 1.0 to 25.4 mm/s. Differences in mean cutting force and mean puncture force are small compared to their standard deviations, suggesting little or no effect of velocity. The variability in the puncture force does appear to decrease with increasing velocity.

Kobayashi et al. [16] performed needle insertions with a 17G needle into porcine liver samples at 0.5 to 8 mm/s (9 insertions per velocity). Here again the median puncture force seems independent of velocity, whereas variability in puncture force seems to decrease with increasing velocity. On the other hand the median tissue displacement at the moment of puncture appears to decrease with velocity, whereas the variability in puncture displacement remains constant.

Kobayashi et al. [30] investigate the velocity dependence of frictional force, by inserting 17G needles into 2cm thick sections of porcine liver at velocities ranging from 0.01 mm/s to 10 mm/s. Figure 2.11 shows the result for initial frictional force as a function of velocity, based on a total of 60 insertions and 24 livers. The increase in friction force appears to be logarithmic for speeds up to 2 mm/s and remains constant for speed higher than that.

Abolhassani et al. [40–42] considered the insertion of an 18G beveled needle into turkey breast (with skin) at 1 to 20 mm/s. Tissue displacement at the moment of puncture was found to decrease with increasing velocity.

Meltsner et al. [66] investigate the effect of needle insertion speed on total axial force for both rotating needles and non-rotating needles. Insertions of 17G bevel needles and conical needles into bovine muscle at 5 to 20 mm/s show no clear trend.

Frick et al. [14] investigated the effect of velocity on insertion force for a straight (0.88 mm) suture needle, inserted into sheep skin at different skin-tension levels. Five insertions were performed for each combination of speed (1, 5, 10 mm/s)

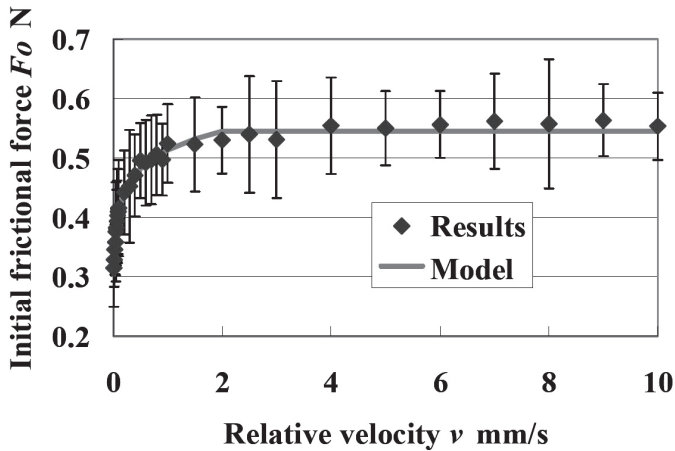


Figure 2.11: Increase in frictional force for a 17G needle in 2cm thick porcine liver at constant speed [30] (24 livers, 60 insertions per measurement point, error bars undefined) (©2009 IEEE)

and skin-tension load (1, 3, 5kg). This was repeated for three adjacent samples of skin, for a total of 135 insertions. No significant effect of velocity on axial force was found, although it is mentioned that statistical power is low. It should be noted here that this is the only study that considers statistical power or the number of insertions required to obtain sensible results.

In short, puncture force was found to decrease with increasing velocity in porcine heart, but remained constant at velocities over 50mm/s. In porcine liver the mean puncture force seems independent of velocity, but its variability was found to decrease with increasing velocity. Friction force in porcine liver was found to increase with velocity up to 2mm/s and remain constant at higher speeds. No effect of velocity on axial force was found in bovine muscle and sheep skin.

In addition to insertion velocity, axial needle rotation is also expected to influence the puncture force and the cutting force (due to drilling effects), as well as the friction force.

2.3.3 Axial rotation

Abolhassani et al. [40–43] inserted 18G beveled needles into turkey tissue with skin, at a constant translational velocity of 10mm/s with rotational frequencies ranging from 1rpm to 25rpm (0.02Hz to 0.42Hz). Continuous rotation was considered, as well as rotational oscillation with amplitudes of 10°, 30°, and 90° for each frequency. Based on 20 insertions per condition (rotation type and frequency), both tissue displacement before puncture and friction force were found to be reduced by rotational motion. Reductions for both variables were in the order of 10% with respect to the non-rotating case. No clear influence of rota-

tional frequency was found, but the range from 3 to 7rpm (0.05Hz to 0.12Hz) is suggested as optimal. Rotational oscillation is said to yield better results than continuous rotation, but it is not clear for which rotational speed.

Meltsner et al. [66] investigated the influence of needle rotation on needle placement accuracy and tissue damage. This was done by inserting 17G beveled needles and 17G conical needles into porcine gel and into beef phantoms, at insertion velocities of 5 to 20mm/s and rotational frequencies of 0, 3, and 5Hz (unidirectional rotation). In both materials, reductions in total axial force greater than 50% were achieved due to rotation of the (conical) needle.

Langevin et al. [60] investigate a phenomenon in acupuncture called needle grasp, referring to the sensation that the needle is grasped by the skin when pulled out. To this end, they measured pull-out force acting on 31G acupuncture needles, after subjecting them to a specific rotation pattern (no-rotation, unidirectional, or bidirectional rotation) at a prescribed depth. Insertion velocity was 10mm/s, rotational frequency 8rpm (0.13Hz), and pull-out velocity was 5mm/s. Measurements were performed on 60 human test subjects, at 16 locations on the body. Needle rotation was found to cause a statistically significant increase in pull-out force in the order of 50% for bi-directional and 150% for unidirectional rotation (compared to no-rotation).

In short, axial rotation was found to reduce friction force in chicken breast, typically by 10%. It was found to reduce total axial force in porcine gel and in beef by up to 50%. In live human skin, rotation of acupuncture needles before pull-out was found to increase pull-out force by up to 150%.

2.3.4 Insertion location and direction

Biological tissue is typically inhomogeneous and anisotropic, i.e. the (mechanical) properties depend on position and orientation respectively. Therefore, it is important to consider the location at which the needle is inserted, as well as the direction of needle insertion with respect to the tissue.

A new location is selected for every insertion by Hing et al. [28, 29], Matsumiya et al. [31], Tran et al. [38], Abolhassani et al. [42], Hiemenz Holton [54], Kataoka et al. [56], Lechner et al. [61], Mahvash and Dupont [64], Naemura et al. [70], but this was done to prevent the needle from following an existing path, not to investigate the influence of insertion location. Insertion location was randomized (within a specific area) by Westbrook et al. [24] and Mahvash and Dupont [17].

Three studies showed some form of systematic investigation of the influence of location on axial force:

Podder et al. [36] and Yan et al. [25] explicitly investigated differences in insertion forces between locations. This was done by inserting 18G diamond tip needles into three different zones of human prostate ex vivo (including cancerous tissue). Axial forces in the different zones were comparable, but no clear conclusions were drawn in this respect.

Langevin et al. [60] found some statistically significant differences (post hoc) in pull-out force for acupuncture needles inserted into the skin of human subjects at different locations of the body, but no conclusion was drawn from this observation.

Crouch et al. [26], Healey et al. [52], Howard et al. [55], Langevin et al. [60], Matsumiya et al. [31], and Westbrook et al. [24] inserted their needles perpendicular to the tissue surface. Okuno et al. [34], Saito and Togawa [78], Saito and Togawa [37], and Hiemenz et al. [96] investigated needle insertions at other angles. However, none of the above explicitly investigated the influence of insertion angle on axial force.

Suzuki et al. [23] investigated the influence of insertion angle (30° and 45°) on axial force and hole shape during penetration of a polyethylene membrane by two catheter tips with different multi-faceted bevels (“Lancet” and “Backcut”) at 3.3mm/s (20 insertions per condition). Only for the “Backcut” type, axial force at 30° was found to be significantly lower (approx. 40%) than for 45° .

In short, information concerning the influences of insertion location or direction is scarce.

2.3.5 Bevel orientation

When a needle with a tip that is not cylindrically symmetrical, e.g. a beveled or diamond tip, is inserted into an anisotropic material, then it is important to consider the orientation of the bevel(s) with respect to the material (i.e. the angle of rotation about the longitudinal axis of the needle). Although this is recognized by Reed et al. [76], Abolhassani et al. [42], and Westbrook et al. [24], the only systematic investigation into the effects of bevel orientation was performed by Lewis et al. [63].

Lewis et al. [63] investigated the effect of bevel orientation on force required to puncture human dura (ex vivo) using a 17G Tuohy needle. The needle was advanced at 20mm/min (0.33mm/s). The difference between puncture forces was investigated for bevel orientations parallel to and perpendicular to the dural fibers. The needle oriented perpendicular to the dural fibers required approximately 30% higher force to penetrate the dura than the parallel one. This difference was found to be statistically significant ($p < 0.05$), based on a total of 40 insertions into 10 different dura specimens.

In short, bevel orientation with respect to tissue fibers appears to have a considerable influence on axial force in human dura.

In addition to insertion method, needle characteristics may also play an important role in needle-tissue interaction.

2.4 Influence of Needle Characteristics

Needles come in many shapes and sizes, and are primarily defined by tip type, diameter (expressed in wire gauge G), and length. The latter is not discussed

here, although a longer needle could deflect more easily, which would influence the loads. Other factors that may influence the axial force are the presence of lubricants and the sharpness of the tip.

2.4.1 Diameter

The outer diameter of the cannula is specified according to the Stubs wire-gauge standard (ISO 9626), denoted by a capital G. Popular sizes range from 10G (3.4mm) to 30G (0.31mm), where a higher gauge indicates a smaller diameter.

Stellman [22] compared 18G, 22G, 26G and 30G beveled needles from different manufacturers, with different types of lubricant, by inserting them into polyurethane membranes at 1.7mm/s . An increase in puncture force with diameter was observed, irrespective of lubrication type and manufacturer.

Shergold and Fleck [80] inserted conical tip needles (60 degree tip angle) with diameters 0.5mm (25G), 1mm (19G), and 2mm (14G) into silicone rubber at 0.8mm/s . Peak axial force was found to increase with diameter.

Okamura et al. [18] and O'Leary et al. [73] investigated the influence of diameter on the average slope of the axial-force vs position curve by inserting the needles into silicone rubber (three insertions per needle) at 2.65mm/s (for 7 seconds). Two-way analysis of variance for three ranges of diameter ($0.59\text{-}0.75\text{mm}$, $0.95\text{-}1.0\text{mm}$, and 1.55mm) and three tip types (bevel, cone, diamond) showed statistically significant influence of diameter on force-position slope (slope increases with diameter). This is consistent with increased friction force. Significant interaction between factors was also found, suggesting that the effect of tip type is aggravated by increased diameter.

Okuno et al. [34] measured total axial force during puncture of human skin and vena mediana cubiti in ten human subjects, in vivo. Insertion was performed manually at approximately 15mm/s with 27G and 21G beveled needles. The results suggest an influence of needle diameter on peak axial force.

Podder et al. [20] measured total axial force during manual insertion of 18G and 17G diamond tip needles during clinical procedures on 20 patients (10 patients per needle size, with a total of 52 insertions). Results clearly suggest that peak axial force increases with needle diameter. In order to assess the influence of confounding factors, this conclusion was verified by inserting the needles into a PVC phantom under controlled circumstances. The effect was still present, albeit somewhat smaller. Similar results are found for 17G and 18G needles in 25 patients (72 insertions total) by Podder et al. [21, 35].

In short, puncture force was found to increase with diameter for beveled needles in polyurethane. Peak axial force was found to increase with diameter in human tissue in vivo as well as in silicone rubber. The slope of the force-position curve in silicone was found to increase with diameter, which is consistent with an increase in friction. In addition, increased diameter was found to aggravate the effect of tip type in silicone.

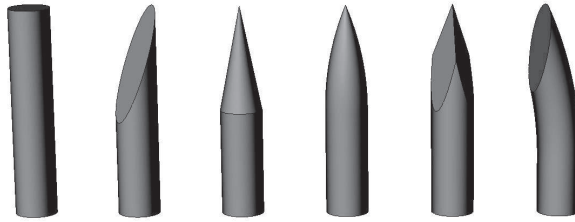


Figure 2.12: Basic needle tip shapes (left-to-right): blunt, beveled, conical, Sprotte, diamond (Franseen), Tuohy. Note that there are many variations of the basic beveled tip, characterized by the presence of multiple facets (e.g. Quincke).

2.4.2 Tip type

The function of the needle tip is to create a passage through tissue. This is typically achieved by a combination of cutting and wedging. The amount of force needed to cut a path, and the amount of tissue damage that arises as a result, depend on the shape of the needle tip. The most common needle tip shapes are depicted in Figure 2.12.

Basic tip shape

Westbrook et al. [24] found that conical needles of various size lead to higher peak axial force than Quincke needles (i.e. multi-faceted bevel) when inserted manually into excised bovine dura, with bevel parallel to the fiber direction.

Shergold and Fleck [80] compared the peak axial force and crack propagation mechanisms for 1.0mm (19G) blunt and conical tip needles in two types of silicone rubber, at 0.8mm/s. The conical needle showed a steady increase in peak axial force due to steady crack extension, the blunt needle exhibited much larger forces with unsteady crack extension.

Mahvash and Dupont [17] inserted 19G diamond tip trocar needles and 18G beveled needles into porcine heart ex vivo at a wide range of velocities. It was found that the diamond tip needle, despite its smaller diameter, consistently showed a peak axial force approximately twice as high as for the beveled needle. This is depicted in Figure 2.10. It is not clear from the text whether this is due to the actual puncture or to the transition from stylet to shaft.

Okamura et al. [18] and O'Leary et al. [73] inserted conical, beveled, and diamond tip needles into silicone rubber at 2.65mm/s. It was found that an increasing number of cutting edges (conical → beveled → diamond) leads to a decrease in slope of the axial-force vs position curve (which is consistent with a decrease in friction force). This effect was shown to be statistically significant, and was shown to become stronger for larger diameters.

Meltsner et al. [66] inserted 17G conical needles and beveled needles into porcine gelatin at 5, 10, and 20mm/s. Differences in axial force were minimal.

Photographs of the effect of tip type on gel damage are shown.

In short, conical tips produce higher peak axial force than Quincke bevels in bovine dura. Peak axial force for blunt tipped needles was much higher than for conical tips in silicone. Diamond tip trocar needles caused much higher peak axial force than beveled needles in porcine heart, despite smaller diameter. Furthermore, an increased number of cutting edges was found to decrease friction force in silicone.

Tip shape details

Details in the shape of the tip often lead to characteristic traits in the axial force.

Hing et al. [28, 29] inserted a diamond tip trocar needle into porcine liver at velocities up to 25.4mm/s . This kind of needle consists of a blunt cannula with a diamond tip stylet that protrudes fully from the cannula. It is observed that there are two peaks in the force-position curve: a small one due to the diamond tip (puncture) and a large one due to the transition from tip to shaft.

Stellman [22] discusses the detailed characteristics of the force-displacement curve during penetration of a polyurethane film using a 22G beveled needle. A small peak was typically found for initial puncture of the membrane, followed by a large peak associated with the transition from bevel to shaft.

Sources from industry show similar results. Mueller [33] measured the axial forces for 18G, 20G, and 21G multi-faceted bevel needles during 24 insertions into 0.4mm polyurethane membranes at 100mm/min (i.e. 1.67mm/s). Distinct force peaks were observed at the moment of initial puncture, at the transition between facets, and at the transition from bevel to shaft. Mayer et al. [32] found the same kind of result for 27G, 29G and 30G beveled needles. Both sources closely follow the methods described in the German industry standard DIN 13097 for hypodermic needle tips.

Nguyen et al. [72] present a force-displacement curve for a 25G multi-faceted bevel needle inserted into a 0.8mm thick neoprene membrane at a very low speed of 0.05mm/min (0.0008mm/s). It shows that, under these circumstances, crack initiation (i.e. puncture) occurs well before the peak force is reached. The peak force is found to occur at the moment the tip protrudes at the other side of the membrane.

Naemura [69] investigates differences in tip shape between six 18G Tuohy needles from different manufacturers, but no useful conclusions are drawn. Tuohy needles have a bent tip, which typically causes the cutting edge to be offset from the center of the cannula. Naemura et al. [70] found that a Tuohy needle with larger tip offset causes a steeper slope after puncture (larger drop in axial force), in both silicone rubber at 2, 4, and 8mm/s ($n = 10$) and porcine ligamentum flavum at 8mm/s ($n = 2$).

Suzuki et al. [23] compare the effect of tip shape details on axial force for two types of multi-faceted bevel tips ('Lancet' and 'Backcut', 20G). They associate the force fluctuations observed with specific geometrical traits of the tip, but their experimental equipment does not include a means to verify whether these asso-

ciations are accurate (e.g. synchronized imaging). No significant influence of tip type on peak forces was found.

In short, a diamond tip trocar needle was found to cause two distinct force peaks when inserted into porcine liver: a small one during puncture, and a large one during the transition from tip to shaft. Similar observations were made for beveled needles penetrating polyurethane and neoprene membranes at low speeds. A larger tip offset in Tuohy needles was found to cause a larger drop in force after puncture.

Bevel angle

Westbrook et al. [24] compared 26G Quincke needles (multi-faceted bevel) from two different manufacturers during manual insertion into bovine dura ex vivo. They found a significantly higher puncture force for larger bevel angles (mean/std: $0.15/0.03\text{kgf}$ vs $0.03/0.01\text{kgf}$ for $n = 10$). The bevel angles were not specified.

Okamura et al. [18] and O'Leary et al. [73] attempted to correlate axial forces and bevel angle for 1.0mm diameter beveled needles, with bevel angles of 10° , 14° , and 20° , inserted into silicone rubber at 2.65mm/s . No significant effect was found.

Azar and Hayward [46] found indications (based on small samples) that crack length in porcine liver is approximately equal to needle diameter for a 22° bevel, but larger than diameter for 45° bevel.

Misra et al. [105] inserted large needle models of 15mm diameter with bevel angles of 10° to 60° into three different Plastisol gels. The transverse force was found to decrease quickly with increasing bevel angle, starting at 4N for 10° bevel angle and approaching zero at 45° .

Kataoka et al. [98] and Naemura [69] also considered the effect of tip angles, but methods and results are not clear.

In short, there are some indications that increased bevel angle may lead to higher axial forces and greater crack length.

Influence of the stylet

Most needles are equipped with a stylet that fits inside the lumen and prevents the accumulation of tissue during insertion. This stylet is usually flush with the tip, but so-called trocar needles have a cutting stylet which protrudes from the cannula.

It is not unthinkable that the presence of a stylet could influence the cutting behavior of the needle, since it influences the size of the contact area between needle tip and tissue. However, the presence of a stylet is not explicitly considered in any of the publications discussed here (except for the diamond tip trocar needles).

2.4.3 Sharpness

A sharp needle cuts more easily than a blunt one. The question is whether this effect is large enough to be of importance.

Westbrook et al. [24], Frick et al. [14], and Langevin et al. [60] used a new needle for each insertion. Nguyen et al. [72] re-used their needles up to five times, and Lewis et al. [63] used each of their needles for eight insertions into human dura. The latter used needles that had already been ‘appropriately blunted’ during actual epidural procedures.

Stellman [22] presents the only systematic investigation of sharpness. This was done by performing three subsequent penetrations of polyurethane membrane with each needle, using 22G and 26G beveled needles from different manufacturers, in combination with various lubricants. Successive insertions showed a statistically significant (although quite small) increase in peak force compared to the first insertion for the 26G needle, irrespective of lubricant type. For the 22G needle no significant influence was found.

In short, for 26G beveled needles penetrating polyurethane membrane a small increase in axial force was observed in successive insertions.

2.4.4 Lubrication

Needles are typically covered with lubricant by the manufacturer.

Stellman [22] investigated the influence of different needle lubricants on peak insertion forces for (beveled) hypodermic needles, of different diameters (18G, 22G, 26G, 30G) and brands, inserted through a thin polyurethane membrane at $100\text{mm}/\text{min}$ ($1.7\text{mm}/\text{s}$). For all diameters a large (and significant) difference was found between peak forces for the lubricated needle and those for the bare needle (irrespective of lubricant type and needle manufacturer). The bare needles generated peak forces over two times as large as those for the lubricated needles. Variability was shown to be relatively small for sample sizes of 10 to 30 insertions per needle, and was smaller for lubricated needles than for bare needles.

Naemura et al. [70] found that the first insertion of their custom-made 18G Tuohy needles into 3mm thick silicone rubber membranes required consistently higher total axial force (in the order of 10%) than subsequent insertions (at new locations). Microscopic investigation of the needle surface after insertion showed traces of silicone, which may act as a lubricant.

In short, lubricant, irrespective of type, appears to have a large effect on peak axial force for beveled needles puncturing polyurethane membranes. However, it is not known whether this effect is also present in biological tissue. The fact that moisture is released due to cutting of biological tissue might play a role here. The influence of tissue properties is discussed next.

2.5 Influence of Tissue Characteristics

Of the 99 papers included in this survey, 38 considered artificial tissue in the form of porcine gelatin, PVC, Plastisol, silicone or similar materials.

In vitro measurements were performed on porcine tissue (25 papers), bovine tissue (12 papers), canine tissue (2), rabbit (1), chicken (4), turkey (3), sheep (2), and human (8) tissue, in a variety of organs, muscle being the most popular.

In vivo measurements were performed on human test subjects (14 papers), porcine subjects (8) and rabbits (5), again in a variety of organs, where skin (with underlying tissue) is most popular.

A table relating specific articles to combinations of organism, tissue type, and tissue condition is provided online as supplementary material.

The first question to be asked here is whether artificial tissue is a reliable substitute for biological tissue.

2.5.1 Artificial vs Biological

Artificial tissue offers many practical advantages over biological tissue, in terms of reproducibility, availability, visibility, etc. However, based on differences in microscopic structure between the two, most likely there will also be differences in needle-tissue interaction. For example, rubber or silicone phantoms may exhibit excessive frictional force. Whether the practical advantages of using artificial material outweigh the supposed lack of realism depends on the application.

The differences between artificial and biological tissue have not been investigated rigorously in any of the papers included in this survey. Nevertheless, the subject is touched upon in [18, 25, 66, 67, 70, 71, 73, 76, 80].

Meltsner et al. [66] inserted rotating and non-rotating conical needles into bovine muscle tissue and into a porcine gelatine phantom, at three different velocities. The axial force vs position relation for the artificial phantom was approximately linear, contrary to that for the bovine muscle tissue, which was highly non-linear. The effect of insertion velocity is clearly distinguishable in the artificial phantom, whereas no such effect is seen in the muscle tissue. The influence of rotation on axial force is clearly visible in both artificial phantom and muscle tissue.

Misra et al. [67] determined the (effective) modulus of elasticity and the rupture toughness for plastisol gel, porcine gel, and chicken breast. Although the mean modulus of elasticity was found to be comparable for all materials, mean rupture toughness for porcine gel was almost five times as high as for chicken breast. For plastisol it was approximately twice as high as for chicken breast.

Reed et al. [76] investigated rotational friction acting on the shaft of a 24G needle during rotational and translational motion, in various materials, by measuring the lag in rotation angle at the tip. Plastisol gel, porcine gel, ballistics gel, and chicken breast were investigated. Tip lag in chicken at a depth of 10cm was found to be negligibly small (in the order of 1°), followed closely by soft plastisol

and hard plastisol (in the order of 10°). In porcine gel the tip lag was approximately 30° and in ballistic gel it was as high as 45° . Porcine gel was found to exhibit the worst stick-slip behavior.

Shergold and Fleck [80] investigated insertion force and crack shape for beveled, conical, and blunt needles, inserted into two types of silicone rubber as well as into human skin *in vivo* and porcine skin *in vitro*. Inspection of microscopic images of the crack at the surface level indicated that crack shape depends on tip shape for both rubber and skin. This is the only paper found that attempts to justify the use of artificial phantoms using data from literature.

Naemura et al. [70, 71] compared axial forces for Tuohy needles inserted into silicone rubber membranes and porcine ligamentum flavum. Peak axial force for the silicone rubber was found to be approximately three times as high as for the ligamentum flavum. Forces in an artificial phantom composed of melamine foam and latex rubber were found to be qualitatively and quantitatively similar to those in porcine ligaments.

In short, force-position curves in porcine gelatine were found to be linear, whereas in bovine tissue they were highly nonlinear. Axial force in gelatine was influenced both by velocity and rotation, but in bovine muscle it was only influenced by rotation. Although modulus of elasticity was comparable for chicken breast and several artificial materials, the rupture toughness of chicken breast was several times smaller. Indications were also found that friction in artificial materials is much higher than for chicken breast. Crack shapes were found to be similar in skin and silicone rubber.

2.5.2 Human tissue vs other biological tissue

It would be useful to know to what extent animal tissue can be used as a substitute for human tissue, since the former can be obtained in greater quantities and is typically easier to work with. The difference between human tissue and tissue from other animals is discussed in [34, 54, 85, 86], but an extensive systematic investigation of the influence on needle-tissue interaction forces was not found.

Brett et al. [85, 86] investigated the force patterns encountered during epidural needle insertion (through skin and relevant ligaments). This was done by inserting Tuohy needles (unknown size) into recently deceased porcine samples (constant velocity) and into recently deceased human cadavers (manual insertion). The force-position curves were found to be qualitatively similar, but peak forces and friction forces in porcine tissue were much higher.

Hiemenz Holton [54] investigated insertion of 18G Tuohy needles into human skin and fat (0.2mm/s) and into porcine skin (0.1mm/s). Mean peak axial force for porcine skin, as well as variability (although unspecified), were found to be over twice as high as those for human skin.

Okuno et al. [34] inserted 27G and 21G hypodermic needles through the skin into rabbit veins and human veins, both *in vivo*. The rabbit insertions ($n = 24$) were automated, whereas the human insertions ($n = 10$) were performed manually. It is concluded that the force patterns (in time) are qualitatively similar.

In short, penetration of porcine skin using Tuohy needles was found to require higher force than penetration of human skin. In vivo penetration of blood vessel, through the skin, delivered qualitatively similar force-time relations for both human and rabbit.

2.5.3 Live vs dead biological tissue

In vivo measurements are typically more difficult to perform than ex vivo measurements, for practical as well as ethical reasons. Therefore it is very important to know if, and under which circumstances, ex vivo measurements can be used as a reliable substitute for in vivo measurements when investigating needle-tissue interaction.

No studies were found that systematically investigate the difference between living and dead tissue in terms of needle-tissue interaction. The subject is, however, touched upon in [53, 93, 99].

Heverly and Dupont [53] measured axial force during needle insertions into the hearts of very recently (10 minutes) deceased rabbits. They also performed ultrasound (US) guided needle insertions into rabbit hearts in vivo, without measuring force. It is concluded that puncture force is reduced at higher velocity both in vitro and in vivo.

Kobayashi et al. [99] inserted a 17G beveled needle into porcine liver, both in vitro and in vivo. Data were used to identify the parameters of a non-linear finite element model. In vivo, the stiffness parameters were two to six times as high as in vitro.

Elagha et al. [93] punctured porcine interatrial septum (internal heart wall), both in vitro and in vivo, but no conclusions are drawn with respect to the difference between living or dead tissue.

In short, there are indications that velocity effects are present in rabbit heart tissue, both dead and alive. Live porcine liver was associated with higher stiffness values in a FE model.

2.5.4 Decay time

Only Choy et al. [49] explicitly investigate the influence of decay time on instrument-tissue interaction force. Strictly speaking, they use a RF-ablation catheter tip instead of a needle. A 12G catheter was moved into porcine heart tissue (endocardium) in three different areas, from 0.5mm up to 4mm penetration depth. This was done 15min, 40min, 3h, 8h and 18h after death. The force at a given depth was found to increase with decay time. For example, at 4mm depth, the force after three hours was already twice as high as after 15 minutes, and after 18 hours it was eight times as high. It is concluded that tissue properties can already change considerably within minutes after death.

Other authors also recognized the necessity to minimize (or mention) decay time. The following decay times were achieved with various tissues: 10min human prostate [25, 36]; 10min rabbit heart [53]; 2h porcine liver [29]; 2h bovine

dura [24]; 2-5h porcine back [85]; 3-6h bovine liver [18]; 24h canine back [96]; 24h porcine liver [46]; 24-48h porcine back [38]; and 26h porcine back [54].

2.5.5 Freezing and tissue hydration

The influence of freezing and thawing tissue, despite its potential to inflict damage on the tissue at a microscopic scale, is not investigated in any of the studies included in this survey. The effects of temperature, tissue hydration or perfusion, or rigor mortis are also neglected. Several authors do mention storing tissue in saline to prevent moisture loss [24, 29, 39, 48, 49, 53, 63, 85].

Literature related to the food industry, e.g. Lawrie and Ledward [115] and Warriss [116], contains a wealth of information concerning the changes that take place in muscle tissue post-mortem. The influence of rigor mortis, moisture loss, and freezing are investigated there in relation to the tenderness of meat (after cooking).

2.6 Discussion

In the preceding sections, information regarding the influence of different variables on the axial force during needle insertion was presented, irrespective of classification.

However, in order to properly interpret the experimental data presented, information concerning sample size and variability is indispensable. Therefore only papers in the C2 and C3 classes are discussed here. The most important findings from these papers are summarized in Table 2.6, and a table with findings from all articles is available online as supplementary material.

2.6.1 Axial force characteristics

It is safe to say that the moment at which puncture (crack initiation) occurs depends on the stress levels in the tissue surrounding the needle tip, as described by Kobayashi et al. [16]. Moreover, in order to understand the puncture phenomenon, it is essential that tissue displacements are measured in addition to needle displacement, as done by Kobayashi et al. [30].

As far as composition of the axial force is concerned, the (practically) linear increase in force with needle position, as observed by Hing et al. [28, 29] in porcine liver, is consistent with the assumption that axial force is composed of a constant cutting force at the tip and a friction force that is uniformly distributed along the needle. The latter is also supported by the findings of Crouch et al. [26], for silicone gel.

Table 2.3: Main findings from C2-C3 articles (for puncture, cutting, friction, and total force)

		F_p	F_c	F_f	F_{tot}
Velocity	art			+	
	bio	0/-		+	
Diameter	art	+		+	
	bio				+
Bevel angle	art				0
	bio	+			
# Tip edges	art			-	
	bio	-			+
Tip details	art	+			
	bio	+			0
Sharpness	art				-
Lubricant	art				-
Patient crit.	bio				0
Location	bio	0	0		
Art vs bio					0

+ pos. correlation, - neg. correlation, 0 no corr. or inconclusive

2.6.2 Insertion method

It is clear that the mean *puncture force* in porcine heart decreases with increasing velocities up to 75mm/s , after which it remains more or less constant, as shown by Mahvash and Dupont [17]. The variability of the puncture force in porcine liver was also found to decrease with increasing velocity, according to Kobayashi et al. [16] and Hing et al. [28, 29].

On the other hand, velocity could not be shown to influence *cutting force* in porcine liver by Hing et al. [29], nor could a sound investigation by Frick et al. [14] uncover any influence of velocity on *peak axial force* when penetrating sheep skin.

It is likely that *friction force* in silicone gel is increased by increasing velocity, based on the increase in slope of the force-position curves found by Crouch et al. [26].

The investigation into the effect of insertion location in the human prostate by Podder et al. [36] and Yan et al. [25] came up inconclusive in this respect.

2.6.3 Needle characteristics

Quite some data, based on manual insertions in over fifty live human patients, is presented by Podder et al. [20, 21, 35] in support of the assumption that *peak axial force* is increased when needle diameter is increased. A similar conclusion was reached by Okuno et al. [34].

The type of needle also seems to be of influence: Conical needles were associated with a higher *peak axial force* than beveled needles when penetrating

bovine dura, and large bevel angles required more force than small bevel angles [24]. Furthermore, *peak axial force* for diamond tip trocar needles was consistently higher than for beveled needles during insertion into porcine heart, despite the fact that the beveled needles had larger diameter [17].

The latter should be considered in light of the findings presented by Hing et al. [28, 29], who observed that diamond tip trocar needles in porcine liver produce a small peak during puncture, followed by a much larger peak due to the transition from tip to shaft. A similar effect was found for beveled needles penetrating polyurethane film, e.g. by Stellman [22].

A decrease in slope of the force-position curve suggests that *friction force* in silicone rubber decreases with increasing number of cutting edges (conical → beveled → diamond) as found by Okamura et al. [18]. This effect was amplified by increased needle diameter.

Bevel shape details were not found to have a relevant effect on axial force by Suzuki et al. [23], nor was bevel angle [18].

2.6.4 Tissue characteristics

Forces during hypodermic needle insertion into human skin and into rabbit ears (both in vivo) were found to be qualitatively similar by Okuno et al. [34]. However, the actual influence of tissue characteristics on axial force during needle insertion remains a mystery.

2.7 Conclusion

A survey was presented of experimental needle-tissue interaction force data available in literature. This survey is organized in such a way that the reader can quickly find literature (useful for) investigating the influence of specific variables on axial force during needle insertion.

Although many studies did present force data, dedicated experimental investigations of the topics of interest were scarce and thinly spread. Therefore it was not possible to synthesize conclusive results from literature in the manner of a meta-analysis.

Nevertheless, good indications were found that puncture force decreases and friction force increases with increasing insertion velocity, and that needles with larger diameter typically cause higher peak forces, although the strength of these effects depends on the type of tissue. The highest force peaks during membrane puncture appear not to occur during initial penetration but slightly later, when the membrane is transferred from the tip to the shaft.

Many questions remain open for investigation, especially those related to biological tissue. For example, it is not clear whether artificial phantom materials provide a good alternative for biological tissue when investigating the effect of insertion velocity on axial force. Although the trends found for the influence of

velocity on friction force were similar in both types of tissue, there were considerable quantitative differences.

Moreover, measuring forces *in vivo* is substantially more difficult, both in a practical sense and in an ethical sense, than measuring forces *ex vivo*. Therefore it would be interesting to know to what extent *ex vivo* measurements can be used as a substitute for *in vivo* measurements. The same goes for using animal tissue as a substitute for human tissue. However, this survey was not able to shed sufficient light on these issues.

Seeing that variability is typically high when dealing with biological tissue, it is difficult to interpret experimental data without some indication of both the variability and the sample size. Out of 99 papers, 73 did not report these values.

Chapter 3

A data model for needle-tissue interaction experiments

Science is communicated by instruction, in order that one man may profit by the experience of another and be spared the trouble of accumulating it for himself; and, thus, to spare posterity, the experiences of whole generations are stored up in libraries.
—Ernst Mach, 1919

3.1 Introduction

The needle-tissue interaction process involves a great number of variables. The preceding chapter investigated the effects that some of these variables may have on the insertion force, by studying experimental data available in the literature. This task was complicated by the diversity of experimental methods, the sparsity of available data, and the variability in these data.

The current chapter presents a structured approach to storage and usage of experimental data, designed to deal with these complications. The challenge here is to represent experimental data from a variety of sources in such a way that reliable knowledge can be synthesized and specific questions can be answered.

3.1.1 Structured representation of experiments

To make experimental data tractable and comparable, it is necessary to provide a uniform description not only of measurement results but also of the experimental methods and materials used. Small details in the experimental approach can make a large difference in the observed results. Thus, a structured method for summarizing all relevant aspects of an experiment is required.

This requirement is met in the scientific literature, to a certain extent, by applying standard formats such as IMRaD (Introduction, Methods, Results, and Discussion) [117]. However, to allow proper assessment of experimental data, such uniformity of structure needs to be carried through much more rigorously.

In the present chapter, the generic needle-tissue interaction experiment is deconstructed into its basic components and interrelations, to serve as a blueprint for the construction of a database. Ponniah [118] defines a database as "... an ordered collection of related data elements intended to meet the information needs of an organization and designed to be shared by multiple users." The information needs in this case cover a broad spectrum, so that a considerable amount of detail is required. In fact, the database should capture at least the level of detail contained in a scientific publication, and preferably more.

The definition of the basic elements in the database and the relationships between these elements is contained in a data model. Common data models are the hierarchical model, the network model, and the relational model. The latter is adopted here because it offers the flexibility required to encode needle-tissue interaction experiments.

3.1.2 Relational data model basics

The relational data model represents the current standard for database solutions [118–120]. In a relational database, pieces of information (data elements) are stored in two-dimensional tables that represent an information entity or class (e.g. RESEARCHER). Table columns represent relevant attributes of that class (e.g. `first_name`, `last_name`) and rows (also referred to as records or tuples) represent unique instances (e.g. Charlie, Parker). These instances are uniquely identified by one or more of the table's attributes. Such a set of identifying attributes is called a primary key (PK) (e.g. a personnel number).

Relationships between tables, or between instances (rows) within a single table, can be established by adding attributes that refer to the primary keys of other instances. These reference attributes are called foreign keys (FK). The referencing table, i.e. the one with the foreign key, is called the child table, and the referenced table is called parent [120].

Relationships between tables or within a table, defined using foreign keys, may be either one-to-one (e.g. husband and wife) or one-to-many (e.g. relating father and daughter). Many-to-many relationships (e.g. relating brothers and sisters) can be established using an intermediate table which is here referred to as a link-table.

An important aspect of the relational data model is that it incorporates rules and constraints that ensure data integrity. For example, entity integrity is ensured by requiring that primary keys always need to be fully defined (i.e. no part of a primary key may have a null value), and referential integrity is ensured by requiring that a foreign key must either be null or refer to an existing primary key [118]. A practical example of data integrity is that a row (record) cannot be

removed from a table as long as there exist foreign keys that refer to it (either in the same table or in other tables).

3.1.3 Relational data model diagrams

Figure 3.1 presents an example diagram of a relational data model, as implemented in a MySQL environment¹. In this diagram, tables are represented as blocks interconnected by lines which represent relationships.

Each block shows the table name and the names of its attributes (columns). Names of general attributes are preceded by an open diamond. Attributes belonging to the table's primary key are indicated by light-bulbs, and attributes representing foreign keys are indicated by solid diamonds.

Note that the primary key in the LINK table consists of two foreign keys. Both are therefore represented as light-bulbs. This table defines a many-to-many relationship between the other two tables. The link table can incorporate attributes specific to that relationship.

Solid lines represent identifying relationships, and dashed lines represent non-identifying relationships. An identifying relationship implies that entity integrity of the child table depends on the parent table. This happens if the foreign key that defines the relationship is part of the primary key of the child table, so that the foreign key cannot be null.

Note that the lines in the figure have two symbols on either end, representing the minimum (0 or 1) and maximum (1 or many²) number of rows from the table associated in the relationship. Thus, they indicate the type of relationship: one-to-one, one-to-many, or many-to-many.

Let us now have a closer look at the structure of the relational data model for needle-tissue interaction.

3.2 A relational data model for needle-tissue interaction research

The diagram presented in Figure 3.2 represents a prototype of a relational data model for needle-tissue interaction experiments. The model may not be optimal, but it provides sufficient flexibility to encode the needle-tissue interaction experiments encountered in the literature and in the current thesis.

Although there is no strict global hierarchy in the model (no single root), local hierarchy is present in the form of parent-child relationships. Data integrity constraints require the parent to exist before the child.

To see how an experiment can be encoded using this data model, we will consider the most important components, starting with the experiment table.

¹SQL = Structured Query Language

²The symbol for "many" is a fork or "crow's foot"

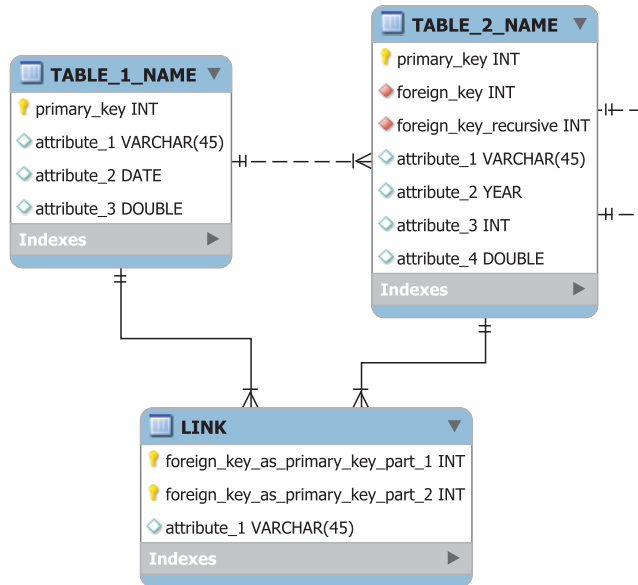


Figure 3.1: Diagram showing basic components of a relational data model (as implemented in MySQL)

3.2.1 Experiment

Without an experiment, there would be nothing to encode. Thus, in a conceptual sense, the experiment could be considered a starting point or root of the data model. Physically, however, the diagram in Figure 3.2 shows that the EXPERIMENT table itself is a child of the AFFILIATION table through the FK at_affiliation_id, thus, at least one affiliation needs to be stored in the database before an experiment can be defined.

The FK at_affiliation_id identifies the physical location where the experiment was conducted. An experiment is conducted in order to answer a specific research question, and usually yields some overall conclusions with respect to this question. Both can be stored in the table. The EXPERIMENT table has additional relationships with two “link” tables and with the CONDITION table. Recall that link tables are used to specify many-to-many relationships.

3.2.2 Researcher

Details of the people involved in an experiment are stored in the RESEARCHER table. A single researcher may be involved in several experiments, and each experiment typically involves several researchers. This many-to-many relationship is accommodated by the LINK_EXPERIMENT_RESEARCHER table. Note that this table also allows specification of the researcher’s affiliation and role, which may

be different for each experiment.

3.2.3 Publication

An experiment may or may not have been published in some form. It is quite common for data from the same experiment to be used in different publications, and it is also common to find data from several experiments in a single publication, hence the LINK_EXPERIMENT_PUBLICATION table.

3.2.4 Condition

The CONDITION table is a child of EXPERIMENT and acts as a hub, connecting various kinds of equipment with test specimens, factors, raw measurement data, and data summaries. This construction allows for a considerable amount of flexibility in encoding experimental designs.

Each needle insertion is unique and is conducted under a specific condition set, i.e. using a unique set of equipment, using specific levels for various factors such as speed and insertion location, and using a specific specimen. Each condition may relate to one or more insertions (repetitions), but each insertion may also relate to one or more conditions, thus allowing different ways of grouping insertions, as shown in Table 3.1. Measurement data from a single insertion (typically in the form of time histories of sensor output) may be stored in multiple files, depending on the various modes of data (e.g. force, position, video).

The measurement results from all insertions belonging to the same condition can be summarized using sets of statistics (e.g. mean, standard deviation, range). A statistic typically describes a specific metric.

Metrics must be specified in as much detail as possible, and may vary widely in definition depending on the research question. For example, one might be interested in the peak force relative to some baseline force in a specific part of a specimen, and perhaps also in the tangent slope (in the force-position plane) just before that peak force.

It is important to note that each metric is associated with its own sample size. The model allows this association to be implemented by defining sample size as a row in STATISTIC_TYPE. Ideally, the sample size would be implicitly known because it would equal the number of insertions associated with the condition. However, not every insertion has to yield a value for each metric. For example, in some insertions it may be possible to identify metric A but it may be impossible to identify metric B.

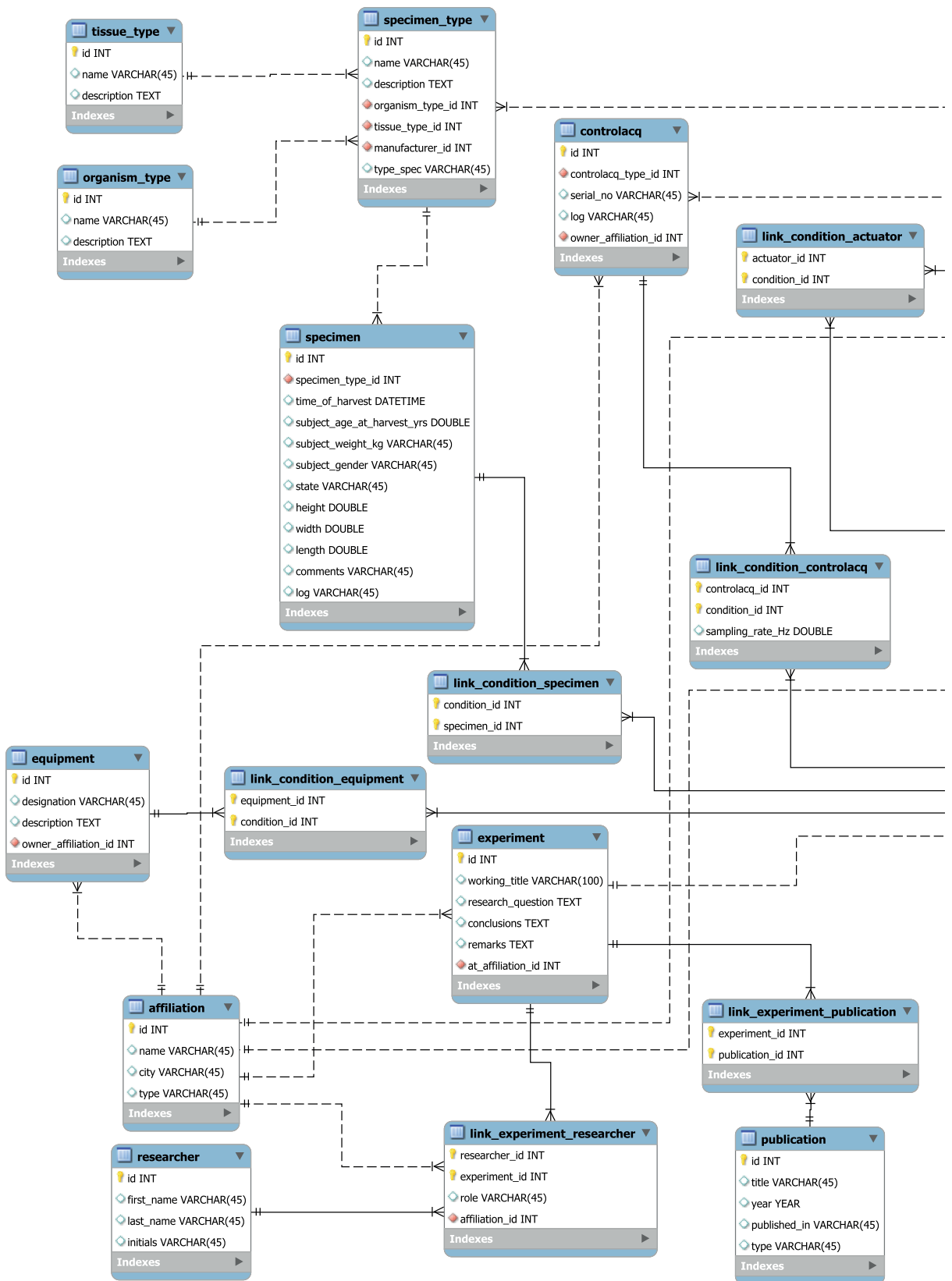
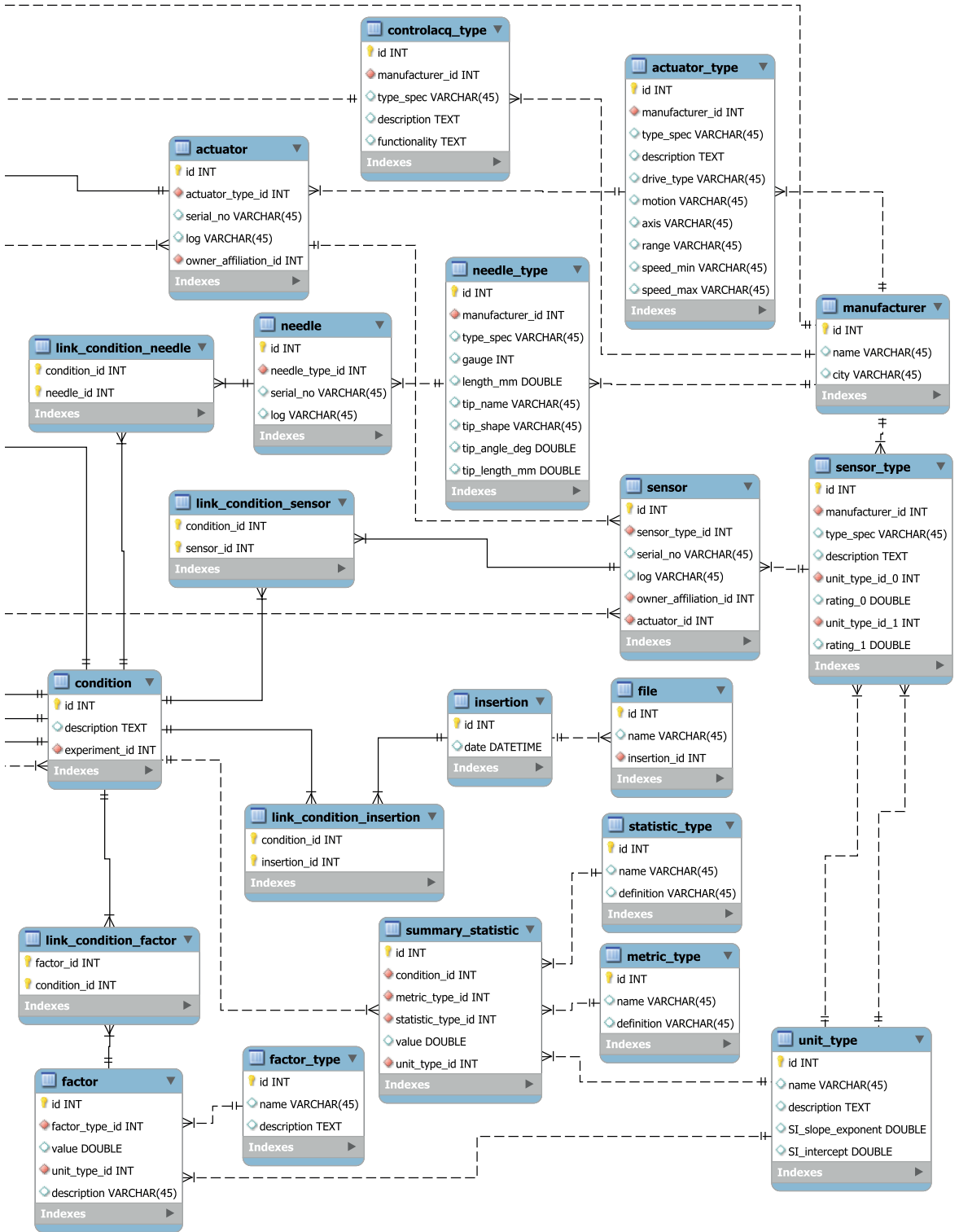


Figure 3.2: Relational data model



To illustrate the flexibility in encoding experimental designs, consider Table 3.1, which shows a design matrix for an hypothetical experiment. In this example, speed is constant, specimen and insertion location are varied in random order, and metrics A and B are summarized by their mean and sample size. Rows 1 to 8 represent the experiment as a 2-by-4 factorial design, rows 9 and 10 represent the same experiment as a 2-by-1 design, and row 11 represents the experiment in a pooled design. Any or all of these representations can be stored in the database by encoding the rows as individual conditions. Thus, different levels of detail can be accommodated.

Table 3.1: Hypothetical example of experimental design

#	insertion	speed	specimen	location	mean		sample size	
					A	B	A	B
1	6	1	1	1	1.2	10.6	1	1
2	1	1	1	2	0.5	-	1	0
3	3	1	1	3	2.6	8.3	1	1
4	8	1	1	4	1.0	7.1	1	1
5	7	1	2	1	0.8	-	1	0
6	4	1	2	2	-	11.0	0	1
7	5	1	2	3	1.1	9.2	1	1
8	2	1	2	4	1.9	8.4	1	1
9	1,3,6,8	1	1	1,...,4	1.33	8.67	4	3
10	2,4,5,7	1	2	1,...,4	1.27	9.53	3	3
11	1,...,8	1	1,2	1,...,4	1.30	9.10	7	6

3.2.5 Factor

The FACTOR table is used to specify unique factor-value combinations. Factor types, such as insertion speed, insertion location, specimen temperature, etc., are defined in the FACTOR_TYPE table. Separate type tables are required because it is not possible to specify all potential factors beforehand.

Many factors may be involved in a condition, and each factor can take many values or levels (note that factor_id may be used as level code). It is also possible that the same factor value is used in multiple conditions. Thus, a link table is required here.

Separate tables are provided for the factors SPECIMEN and NEEDLE, because they must be specified for all conditions and require a more detailed definition.

3.2.6 Specimen

The specimen definition is relatively complex. An individual specimen has various size and history attributes, and is tested in a certain state (e.g. in vivo, in

vitro, or something more specific), as defined in the SPECIMEN table.

A specimen belongs to a certain SPECIMEN_TYPE, which consists of a certain tissue type from a certain organism type. The specimen type also has more specific attributes such as manufacturer (or supplier), type specification (e.g. specific breed of animal, or manufacturer's code), and allows for a detailed description if necessary.

The ORGANISM_TYPE may be biological, such as human or pig, or artificial (synthetic). The TISSUE_TYPE may refer to a specific type of organ, or to a general tissue type such as connective tissue. In case of artificial materials, their general type may be specified as e.g. silicone gel, agar gel, polyurethane membrane, etc.

3.2.7 Needle

Each needle belongs to a certain class, with general size and shape characteristics as specified in the NEEDLE_TYPE table. In addition, each needle instance has its own specific history which is represented in the NEEDLE table.

A single needle may be used in several conditions, but a single condition may also involve several needles. Thus, a many-to-many relationship is established using LINK_CONDITION_NEEDLE.

If the experimental design is encoded in sufficient detail, it becomes possible to trace individual needles to individual insertions via the condition table. However, this does not necessarily have to be the case.

3.2.8 Equipment and instrumentation

The EQUIPMENT table represents various types of equipment. Typical examples would be (custom built) structures for the support of actuators, sensors, needles, or specimens.

The SENSOR table specifies measuring equipment (sensors in a very broad sense) such as load cells, position sensors, temperature sensors. It may also identify imaging equipment such as ultrasound probes or video cameras. Some sensors may be connected to specific actuators, hence the relation with the ACTUATOR table. this table specifies the actuators used to move the needle and/or specimen.

The CONTROLACQ table represents various kinds of electronics used for control and data acquisition. This may include servo-controllers, signal conditioning electronics, power regulation, AD/DA-conversion equipment, image processing equipment, but also general purpose computers.

All equipment and instrumentation tables have many-to-many links with the CONDITION table. Note that equipment settings such as sampling rate for an AD-converter can be specified per condition using the corresponding link tables. Each piece of equipment can be traced back to a specific owner through the FK owner_affiliation_id.

3.2.9 Unit type

One of the main reasons for setting up a needle-tissue interaction database is to allow comparison of experiments and measurement data. This requires that all values should be expressed in common units. For example, a value expressed in millimeters cannot be directly compared with a value expressed in meters: one of the two has to be converted first. The convention adopted here is to convert everything to SI base units³, which are *kg* (kilogram), *m* (meter), *s* (second), *K* (Kelvin), *A* (Ampère), *mol* (mole), and *cd* (candela).

To enable automated conversion, each user defined value has to be specified in conjunction with a unit type. The UNIT_TYPE table requires specification of SI-conversion parameters, viz. the slope and intercept required to convert that specific unit type to SI base units. For example, a value specified in degrees Fahrenheit [$^{\circ}F$] is converted to Kelvin [*K*] using slope $\frac{5}{9}$ and intercept 255.37, or a value in revolutions per minute [*rpm*] is converted to [*rad/s*] (i.e. [*m/m/s*]) using slope $\frac{\pi}{30}$ and intercept 0.

3.3 Model implementation

3.3.1 Data model implementation

The data model provides a blueprint for database implementation. An implementation language like SQL facilitates the conversion from the theoretical data model to a functional database and enables storage and usage of data [118]. SQL incorporates functions for defining the database structure, for adding, changing, and deleting data, and for retrieving data using specific queries. It also provides security functionality for restricting user access. Some general aspects of data manipulation for this specific database are discussed next.

3.3.2 Adding data

Data for the needle-tissue interaction database can originate either from experiments described in the literature, or from original experiments (in which case the database user has access to all information). In both cases, a lot of information needs to be entered by the user. This process needs to be streamlined with the help of a user interface that allows specification of data within the restrictions imposed by the data integrity constraints.

Such an interface can provide the user with the option to reuse existing data elements, such as equipment, factor type or unit type, or to add new ones if necessary. The user interface also needs to deal with the fact that information available in the literature is often incomplete. For example, summary statistics are usually presented, but information about individual insertions is typically not

³SI = Système International d'unités

available. Moreover, not all publications provide sufficient detail to reconstruct the experimental design used.

For data from original experiments, on the other hand, information is complete, and the problem is rather the opposite: Manual input of all available information for each and every insertion can easily become cumbersome. This problem can be avoided by providing batch processing capability on the basis of a specified experimental design. For example, the user can specify the experimental design by providing levels and number of repetitions for all relevant factors, and the user-interface application can then create the individual database records with the appropriate relationships.

3.3.3 Retrieving data

Data retrieval is possible with the help of SQL's extensive query functionality. Appropriate queries can be constructed using the data model as a guide. Default queries, called views, can be specified to reduce query complexity, if necessary.

Simple query examples are: "find all experiments involving bovine liver tissue in an in vitro setting", or "find all experiments using Tuohy needles longer than 80mm." A more complicated example would be "find values of mean friction force in polyurethane membranes with a thickness of 0.2mm from all experiments that use insertion speed higher than 10mm/s and take into account specimen temperature and fixed boundary conditions." It is also possible, for example, to extract all the results obtained using a specific piece of equipment, by a specific person, or at a specific institution (affiliation).

3.4 Discussion

In addition to providing an indispensable tool for reviewing the literature and performing meta-analyses, the database and data model described here represent a framework for storing data and experimental details of new experiments. Using this database approach, it becomes possible to define an experiment beforehand, selecting factor settings and equipment from the database. Moreover, by automating the experimental protocol, results can be added to the database automatically as an experiment progresses.

Thus, by implementing this database and adhering to its structure, not only experimental data but also the corresponding experimental design, methods, and materials can be encoded and stored for future reference.

Chapter 4

Observations of membrane puncture

4.1 Introduction

The preceding chapters discussed the great variety of factors involved in needle-tissue interaction, and their influence on the axial force. Moreover, it was found that there is no such thing as *the* axial force, as this force develops over time and can be characterized in many ways. The present chapter identifies typical characteristics of the axial force that arises during puncture of an artificial thin membrane.

4.1.1 Background

Membranous tissue structures are found throughout the body. These structures typically represent important anatomical boundaries. Think, for example, of the skin, blood vessels, fascia layers, fetal membranes, meninges, the capsules surrounding internal organs, and so on and so forth. To gain access to target sites inside the body, these structures inevitably need to be punctured.

Membrane puncture is defined here as the process from initial contact between needle and membrane up to the point where the membrane has been fully penetrated and the needle tip has passed through completely. The physical mechanism of membrane puncture is of interest in the study of tissue damage, patient discomfort, needle placement accuracy, clinical training, path planning, automated needle insertion, etc.

The most convenient way to study the membrane puncture mechanism is by studying the axial force that arises during puncture. However, the axial force provides only a limited amount of information, which, in itself, is not sufficient

to study the mechanisms at work. The present chapter explores the use of visual observation, in addition to force measurement, to study the puncture process in detail.

4.1.2 Problem statement

As puncture is facilitated by the needle tip, tip geometry must play an important role in the puncture process, and this is likely to be reflected in the axial force. To establish just how the axial force is influenced by tip geometry, it is necessary to relate this force to the actual needle insertion depth, i.e. the depth of the tip with respect to the deformed tissue boundary.

A visual account of the puncture process is required to establish this relation with an acceptable degree of confidence. However, the puncture process is typically difficult to observe visually because, by default, the needle tip is largely obscured by surrounding tissue. Moreover, at practically relevant insertion speeds the puncture process evolves too quickly for the human eye to follow.

Thus, the challenge is to visually observe the puncture process in such a manner that axial force characteristics can be related to geometric properties of the needle tip.

4.1.3 Related work

Naturally, the first step is to see whether this challenge has been met already in the literature. Analytical studies of tip geometry are available, e.g. [121, 122], but these studies do not present useful force measurement data. As described in Chapter 2, the influence of tip geometry on axial force during insertion is indeed considered in a number of studies [3, 22, 23, 28, 29, 32, 33, 69, 70, 72, 123].

All of these studies attribute details of the axial force to specific geometric traits of the needle, as described in Section 2.4.2. However, direct visual accounts of a supposed relation between force and tip geometry are only presented by two commercial sources [3, 33], which are rather brief in terms of methodological detail. Although it is highly likely that the required knowledge exists in industry, as suggested by e.g. [123–125], this information is typically unavailable to the public.

As accurate visual accounts of the puncture process were not found in the scientific literature, there is sufficient reason to pursue this investigation further.

4.1.4 Research question

The present investigation focuses on the puncture of a thin artificial membrane, using a needle with back bevel, under a strictly controlled set of conditions. A camera is used for close observation of the puncture process. To provide a clear field of view for the camera, the membrane is suspended in a unidirectional tension device.

The primary research question is how characteristic force metrics relate to needle tip geometry for the back(-cut) bevel needle, under the specified conditions. The use of specimens in unidirectional tension raises the secondary question whether the orientation of the bevel with respect to the direction of tension has an influence on the force characteristics.

4.1.5 Approach

To answer these questions, a total of 18 penetration tests were performed on three thin polyurethane membranes. The membranes were punctured repeatedly, at fixed speed, using the same needle. The puncture process was observed in detail with the help of a high speed camera, while needle position and axial force were measured. Membrane displacement and needle insertion depth were estimated using the video footage. Sudden changes in the rate of membrane displacement were identified, and the corresponding forces and geometric details were evaluated. Based on this evaluation, force metrics were established and rules were developed for their evaluation. Details of the approach are presented below.

4.2 Materials and methods

4.2.1 Instrumentation

The measurement apparatus, depicted in Figure 4.1, comprises a linear motion stage equipped with a force/torque sensor and mounted vertically on a steel frame. The base of the needle is attached to the force/torque sensor. Test specimens are supported by a uniaxial tensioning device, and placed directly below the stage. A high speed camera is placed a short distance from the specimen.

The linear stage is an Aerotech PRO115-400 with 400mm travel and 5mm/rev ball screw (Aerotech Inc., Pittsburgh, USA). The stage is powered by a Maxon EC40 brushless motor and 4-Q-EC servo-amplifier (Maxon Motor AG, Sachseln, Switzerland), using feedback from a Scancon 2RMHF-7500 incremental rotary encoder with 7500 pulses per revolution (Scancon A/S, Allerød, Denmark).

Loads on the needle are measured using an ATI nano17 six-axis force/torque sensor (ATI Industrial Automation, Apex, USA). The rated load in insertion direction is 17N, with an effective resolution of 0.003N for the complete system.

Data acquisition and position control of the linear stage are achieved using a dedicated PC (AMD Athlon 64 X2 5200+, 3GB RAM, MS Windows XP Pro SP3) equipped with a dSPACE DS1104 real-time controller board (dSPACE GmbH, Paderborn, Germany). Analog data signals are sampled at 1kHz with 12bit resolution.

Forces and moments along all axes are stored on the computer, together with time stamp, position, operating state (insert, pause, retract), and ambient temperature. Data analysis is performed using Matlab R2012b software (The Mathworks Inc., Natick, USA).

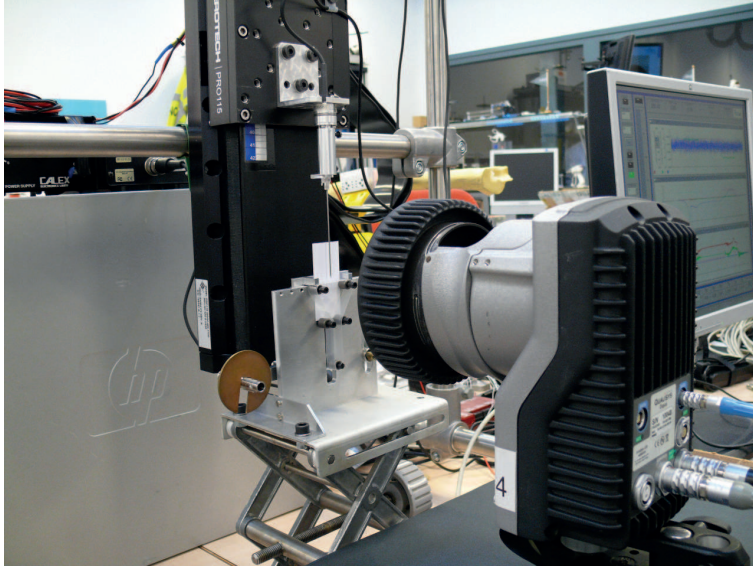


Figure 4.1: Equipment, showing linear motion stage with force sensor and needle, uniaxial tensioning device with specimen, and high-speed camera

A Qualisys Oqus 3 high-speed camera is used, in conjunction with Qualisys Track Manager software (Qualisys AB, Gothenburg, Sweden), to record the puncture process at 400fps (frames per second) with a 1024×1280 resolution. At an insertion speed of 20mm/s , this framerate yields a resolution of $\frac{20}{400} = 0.05\text{mm/frame}$. To synchronize with the force and position signals, video capture is triggered by the (rising flank) linear stage run-state (output from the dSPACE board).

4.2.2 Specimens

Specimens are cut from a single piece of Platilon U 4201 AU thermoplastic polyurethane film (Epurex Films GmbH, Walsrode, Germany). The film material has a Shore A hardness of 87. Material type, thickness, and hardness conform to the DIN-13097 [3] standard for testing needle penetration.

It is noted that thermoplastic polyurethane exhibits (strong) viscoelastic behavior Qi and Boyce [126]. Polyurethane (although perhaps in a different form) was also found to be a valid alternative to biological tissue by Pavlovich et al. [127].

Specimen size is $200\text{mm} \times 8\text{mm}$ with a thickness¹ of 0.3mm . Specimens are welded end on end to create a loop (similar to a rubber band) that fits in the specimen support. Specimens are cleaned with alcohol before use.

¹For comparison, thickness of a typical shopping bag (LDPE) is less than 0.1mm

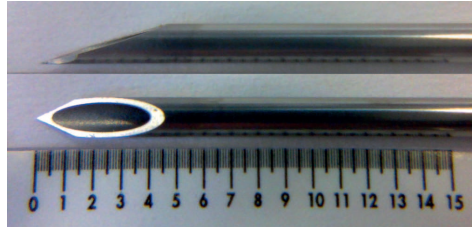


Figure 4.2: Side view and top view of the Vygon Biovalve needle tip (units *mm*)

4.2.3 Specimen support

The uniaxial tensioning device used to support the specimens is depicted in Figure 4.1. The device uses a fixed mass to apply uniaxial tension to the specimen. The specimen is clamped at two ends, with a free standing length of 30mm .

4.2.4 Needles

The needle from a Vygon Biovalve IV cannula (ref 106.21, Vygon SA, Ecoen, France) is used for this experiment because of availability (Figure 4.2). This needle has an outer diameter of 1.5mm (17G), wall thickness approximately 0.2mm , cannula length of 70mm , and a back(-cut) bevel tip. No stylet is used. The needle surface is covered with a silicone-based lubricant (no details available).

The tip is defined here as that part of the needle for which the cross-section shape depends on the axial coordinate, and the cannula as that part for which the cross-section is constant. The very end of the tip, where the cross sectional area becomes zero, is referred to as the needle point. Tip length is approximately 4.5mm , and the main bevel angle is approximately 18° . The tip has two so-called back bevels [121] at an included angle of approximately 50° . Back bevel length is approximately 1.4mm .

4.2.5 Insertion parameters

All runs are performed at a constant speed of 20mm/s (both for insertion and retraction) with a 20mm stroke, the needle moving downward along the vertical axis. Initial distance to the specimen is approximately 5mm , so that a constant speed is reached before making contact with the specimen.

The direction of motion is normal to the specimen surface, and the slip angle is close to zero (i.e. the velocity vector approximately coincides with the longitudinal axis of the needle). Orientation of the bevel with respect to the specimen, i.e. the rotation angle about the longitudinal axis of the needle, is manipulated.

4.2.6 Protocol

In the ideal case, a new needle would be used for each run, but because of limited availability of needles, a single needle is re-used for all runs. To limit the influence of re-use effects (e.g. wear), this needle is pre-conditioned before the start of the experiment. Pre-conditioning consists of 100 manual punctures up to 30mm depth in a piece of sample material.

Before use, specimens are wiped clean using alcohol. After placing a specimen in the tension device, tension is applied and the specimen is clamped. A small tension of 0.4N is used, just to keep the specimen taut. Tension is maintained after clamping. The tension device is placed under the stage so that the specimen is penetrated in the center between clamps.

The bevel orientation is changed before each run by manually rotating the needle about its longitudinal axis. Orientations are chosen according to the experimental design discussed in the next section.

Each run consists of an initial one-second pause, then insertion at constant speed, a two second pause, and finally retraction at the same speed. Video capture is triggered automatically at the start of the run, but needs to be primed manually before each run.

After each puncture, the clamps are released and the specimen is conveyed by 33mm to reveal an undamaged and unstretched part. Given a specimen length of 200mm this allows for a maximum of 6 runs per specimen.

4.2.7 Experimental design

Three specimens are used in sequence (not randomized). With a maximum of 6 runs per specimen this allows a total of 18 runs.

Two bevel orientations are applied, viz. 0° and 90° , because uniaxial loading is expected to cause anisotropic effects (despite the specimen material being homogeneous and isotropic). At 0° (bevel facing the camera) the incision produced by the tip is in line with the direction of tension, so that tension will tend to close the hole. At 90° the incision is perpendicular to direction of tension, so that tension will tend to open the hole.

To reduce the influence of variability between specimens on the evaluation of a bevel-orientation effect, specimens are blocked. That is, random allocation of treatments (bevel orientations) is performed separately for each specimen. This is done in such a way that each bevel orientation occurs three times for each specimen. The allocation is presented in Table 4.1. Since specimens are confounded with time, this blocking scheme also helps to reduce the influence time dependent effects.

The resulting experimental design is a generalized randomized block design (treatments are replicated in each block). It is noted that the runs represent (sequential) repeated measurements on the same needle.

Table 4.1: Allocation of treatments to runs (u_i) following a 3×2 generalized randomized block design

		bevel orientation	
		0°	90°
specimen	1	u_3, u_5, u_6	u_1, u_2, u_4
	2	u_7, u_8, u_{10}	u_9, u_{11}, u_{12}
	3	u_{13}, u_{17}, u_{18}	u_{14}, u_{15}, u_{16}

4.2.8 Data analysis

The experiment yields time-series of absolute needle position and axial force, 18 each, with corresponding high speed video recordings.

The main goal of the investigation is to relate the time-series of axial force to aspects of tip geometry based on the video observations. The axial force arises because the membrane resists deformation, so that axial force must be a function of membrane displacement. The first step, then, is to estimate the (absolute) membrane displacement by (manually) tracing the position of the lowest point on the membrane in each video frame.

Changes in the average rate of membrane displacement (i.e. changes in average membrane velocity) are assumed to represent interesting events. For example, as soon as the rate of membrane displacement starts to differ from the rate of needle displacement, which is constant, we know that the membrane must have failed and the needle is being inserted into the membrane. The points in time (t_{p_i} , where $i = 1, 2, \dots, m$) at which the average rate of membrane displacement changes are estimated automatically by constructing an optimal piecewise fit to the membrane displacement curve using an appropriate method (discussed later). The video frames corresponding to t_{p_i} are extracted for visual inspection and verification.

Subsequently, prominent features (e.g. stationary points) in the vicinity of t_{p_i} are identified on the force-time curve or its first or second derivative. These points represent the characteristic metrics we are looking for. Note that the numerical derivatives with respect to time are obtained from the force-time series, after smoothing², using a fourth-order central difference approximation.

The second goal is to determine to which extent bevel orientation influences the force characteristics. This is achieved by evaluating the most important metrics and comparing them between the 0° and 90° groups. Analysis of variance for the generalized randomized block design is used to strengthen the argument.

First, however, the physical results of the puncture process are examined by studying the needle point and punctured specimens under an optical microscope.

²Noise-robust numerical differentiators exist, but we use separate smoothing in combination with the basic central difference scheme

4.3 Results

4.3.1 Microscopic observations

Figure 4.3 shows close ups of the needle tip after preconditioning. The approximate radius at the point is in the order of micrometers. The point appears to be very slightly bent, but this is not necessarily due to preconditioning, as similar deformations were also observed on new needles. No changes were observed after the experiment.

The back bevel needle tip creates a v-shaped (or chevron-shaped) incision as depicted in Figure 4.4. The incision starts at the needle point and branches outward in two main directions. The inset shows a close up of the initial puncture location with a small third branch due to the edge where the back bevel planes intersect. The edges of the incision are smooth (at this scale), but striations are visible at the initial puncture location and at the ends of the incision, i.e. at the points of largest deformation. As the final incision width is lower than the needle diameter, the material must have been stretched considerably when the needle passed through. The incisions for the 90° orientation are approximately 10 – 15% wider than for the 0° orientation. This is consistent with expectation considering that the specimen is already elongated in the 0° direction when the incision is made.

4.3.2 High speed video footage, membrane displacement, and force response

The high speed video recordings for all 18 runs were found to be qualitatively similar, and so were the measured forces. The results for run 002 (90°) and run 003 (0°) are presented here as representative examples.

The estimated membrane displacement for both runs, which was extracted from the video footage manually, is presented in Figure 4.5. The displacement curve can roughly be divided into six parts, each approximately linear, i.e. with approximately constant slope (i.e. rate of displacement or speed). The transition points between these regions, indicated by black circles in the figure, were estimated automatically by constructing an optimal piecewise linear least squares fit with six line-segments. This was achieved with the help of a global optimization algorithm.

Figure 4.6 shows the axial force as a function of membrane displacement. The loading part of the curve, up to the point of maximum displacement (point 3), is approximated well by a polynomial of (at least) third degree. This figure shows that the axial force indeed behaves as a function of membrane displacement, because initial membrane failure (point 2) does not noticeably alter the loading curve. The unloading part of the curve appears to exhibit hysteresis loops, but it is noted that this type of shape is very sensitive to force-displacement synchronization errors, e.g. due to bias or drift in the estimation of membrane displacement.

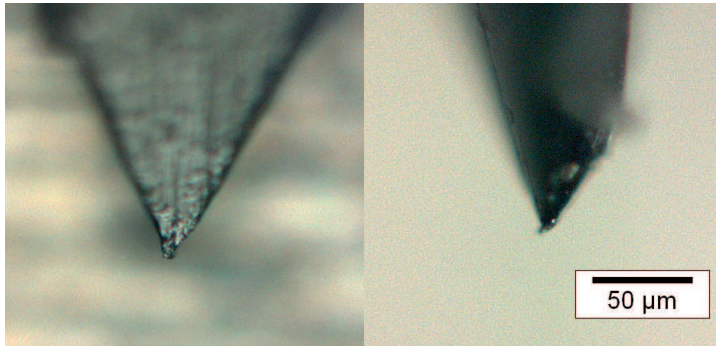


Figure 4.3: Optical micrographs of the needle point after preconditioning. Front view (0°) and side view (90°). Fuzzy appearance is due to limited depth of field, as the point is in focus

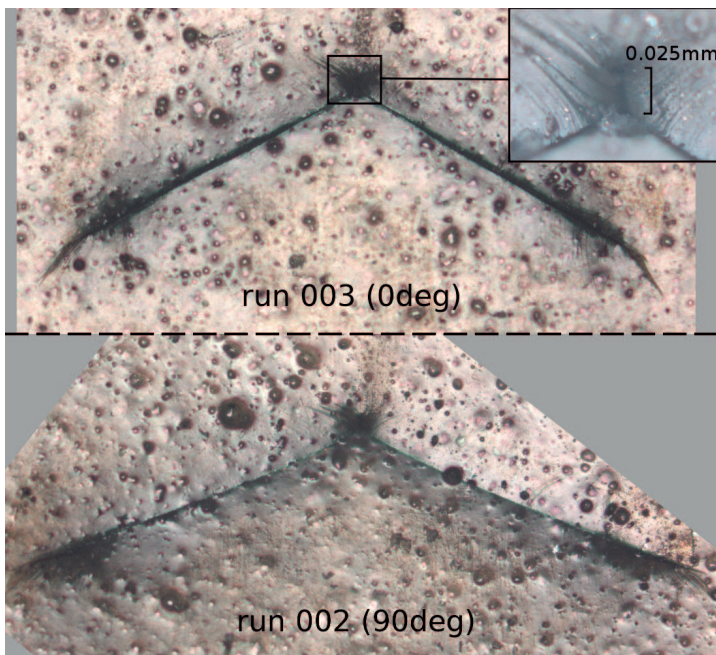


Figure 4.4: Optical micrographs of the incisions resulting from runs 002 and 003. Incision width is 1.45mm for run 002 (90°) and 1.24mm for run 003 (0°). The bubbles that are observed on the polyurethane are similar in size to human epidermal skin cells (typical diameter around 0.02mm [128, 129]).

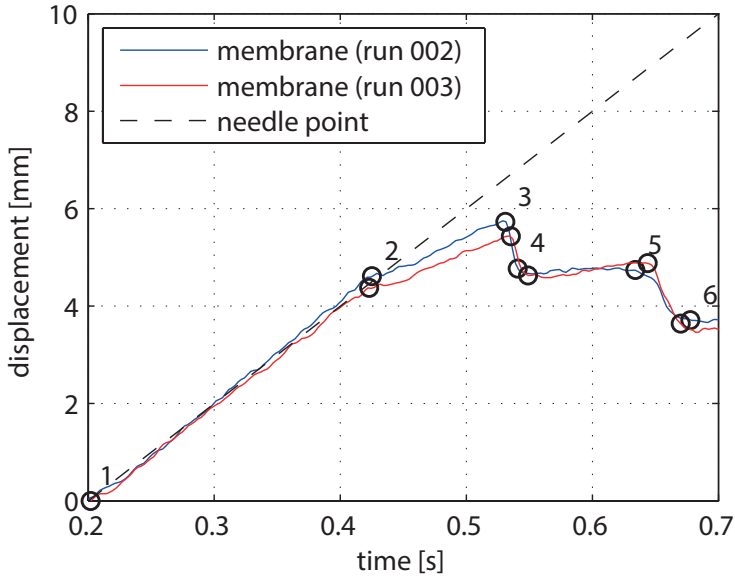


Figure 4.5: Absolute displacement of needle point and membrane for run 002 (90°) and run 003 (0°). Circles indicate estimated changes in rate of displacement

Figure 4.7 presents the axial force as a function of insertion depth and needle geometry. Note that insertion depth is defined as the difference between absolute needle position (measured from the initial contact point) and membrane displacement. This figure clearly shows that the largest force occurs at the end of the back bevel part of the tip (around 1.5mm). After passing the back bevel part, the force quickly drops, then increases slightly as the main bevel enlarges the hole, before dropping off gradually as the membrane passes onto the cannula. We refer to this process (hole enlargement without cutting) as wedging. The principle is illustrated by Figure 4.8.

To verify the relation between force and tip geometry, the video frames corresponding to points 1 to 6 from Figure 4.5 need to be examined more closely. Figure 4.9 shows the video frames in conjunction with the force-time curve. As expected, frame 1 shows the moment of initial contact between needle and membrane. Frame 2 corresponds to the estimated point of initial membrane failure. This initial failure cannot be observed directly, but the needle is seen to exit the membrane several frames later, which confirms that membrane failure has indeed occurred. Frame 3 shows the membrane just before reaching the end of the back bevel part of the tip. Frame 4 shows the membrane just after passing the end of the back bevel part and just before reaching the widest part of the tip. Between frames 3 and 4, both displacement and force drop considerably in a short amount of time. Frame 5 shows the membrane just before reaching the end of

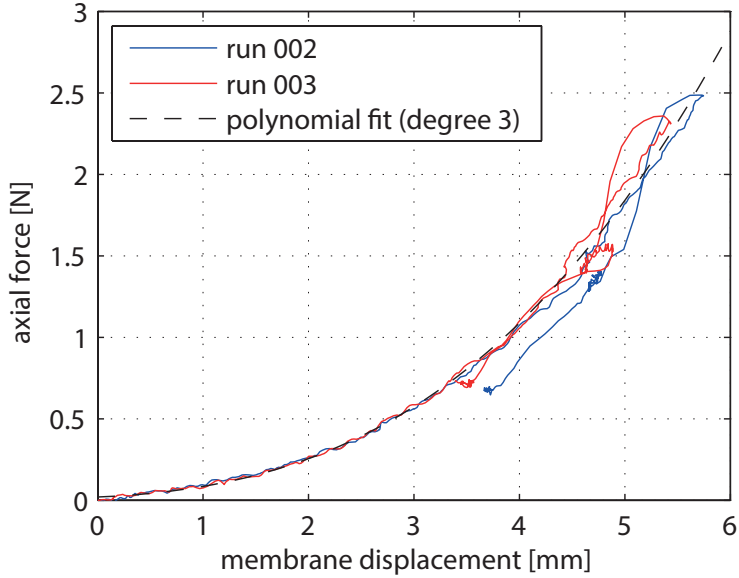


Figure 4.6: Axial force as a function of absolute membrane displacement for run 002 (90°) and run 003 (0°), with a third-degree polynomial fit to the pre-puncture loading curve

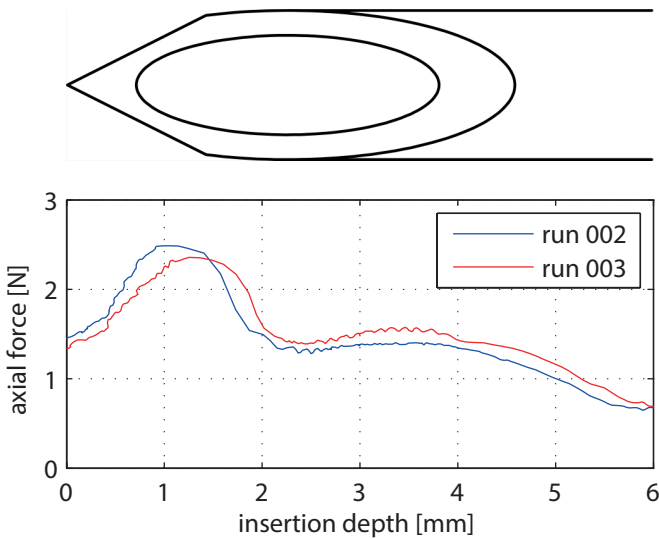


Figure 4.7: Axial force as a function of insertion depth and tip geometry (properly scaled)

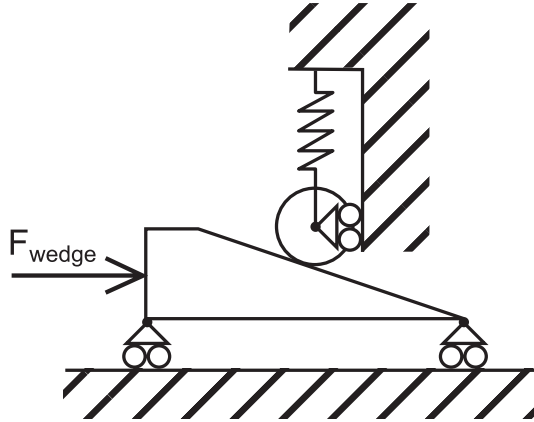


Figure 4.8: Idealization of the wedging process during membrane puncture, in which the bevel enlarges the hole without cutting, resulting in an axial force component. A spring is used to represent the specimen's resistance to hole enlargement, although this process need not be fully reversible.

the tip. Frame 6 shows the membrane just after passing the end of the tip. After frame 6, friction is the only mode of interaction (in axial direction) between needle and membrane (assuming that the angle of slip is zero). The friction force appears to remain constant until motion stops.

No obvious qualitative differences are observed between the two bevel orientations (0° and 90°), although a small difference in peak heights seems to be present. Thus, the same metrics can be used to describe both orientations. these metrics are discussed next.

4.3.3 Basic rules for the identification of characteristic points on the force response curve

To identify characteristic metrics on the force curve for the Biovalve needle we consider the raw force F , the smoothed force F_s , and its first and second derivatives with respect to time, F'_s and F''_s . These are depicted in Figure 4.10 (for run 003), and the six points of interest are highlighted (t_{p_i}). Smoothing of the force response is necessary because the basic central difference differentiator is sensitive to noise. A cascaded unweighted moving average filter, using four passes with a 10-sample kernel, was found to produce adequate results for the current dataset. The question now is whether the points of interest can be estimated on the basis of prominent features of the force signal.

Judging from Figure 4.10, the initial contact point, t_{p_1} , can be estimated directly from the smoothed force. The estimated time of initial membrane failure, t_{p_2} , approximately coincides with a local maximum of the first derivative F'_s , i.e.

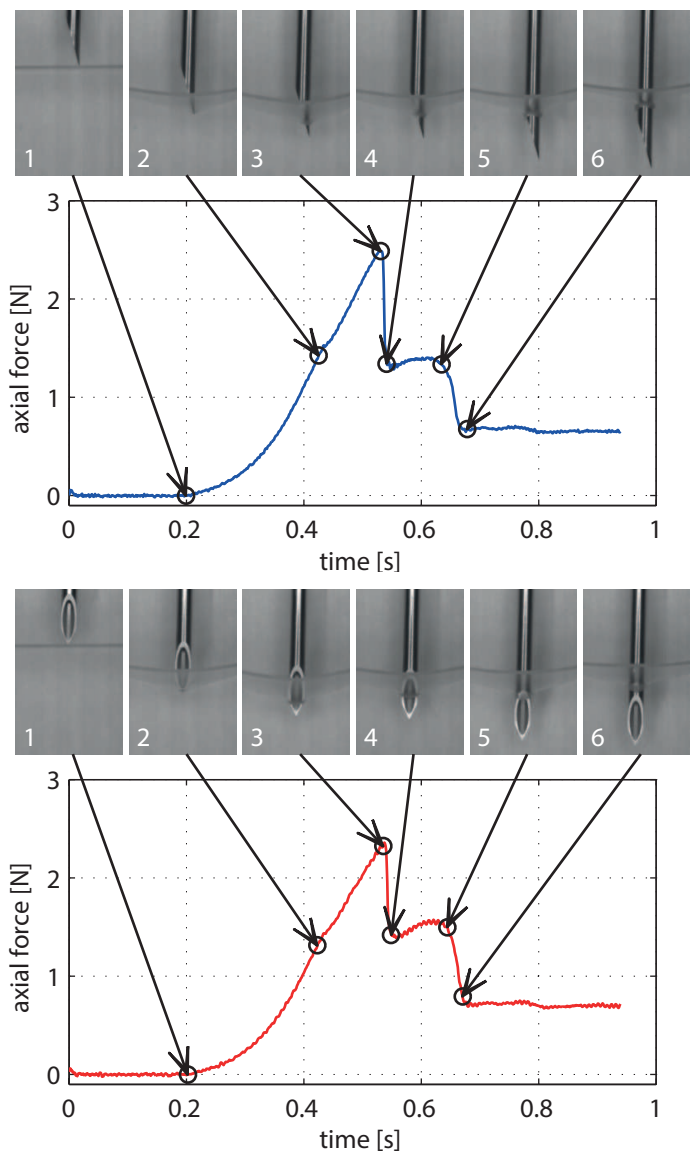


Figure 4.9: Development of axial force in time, with high-speed video stills, for run 002 (90°, top) and run 003 (0°, bottom)

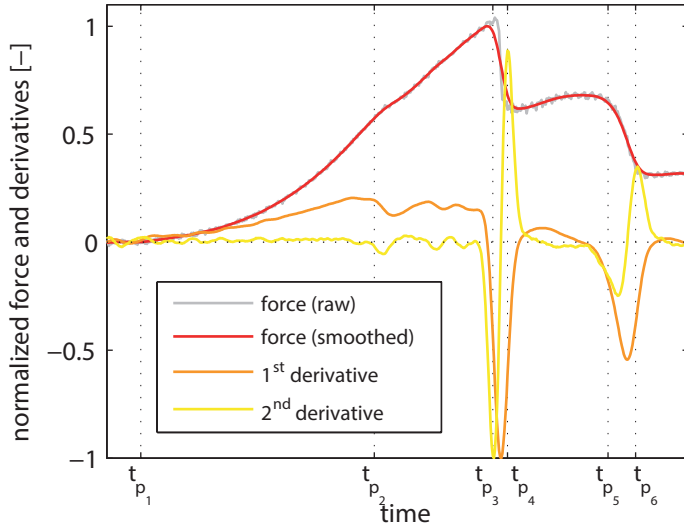


Figure 4.10: Force vs time, for run 003, with first and second derivative and time stamps corresponding to changes in membrane displacement rate

the maximum slope of F_s . Intuitively it would make sense to select the global maximum of F'_s , because a limit to the force-slope is a likely indication that the material is failing in some sense. However, this approach seems error prone due to the plateau in F'_s preceding t_{p_2} . The local minimum of F''_s just following t_{p_2} represents a more precise alternative, although perhaps not very robust. To identify this local minimum, we find the minimum of F''_s on the interval from t_{p_1} to the last zero-crossing of F''_s before its global minimum. The points t_{p_3} to t_{p_6} approximately coincide with the four strongest extrema of F''_s . For our purpose, however, it is more interesting to select the local extrema of F_s (or F). These can be easily found by locating the zero-crossings of F'_s surrounding its two most negative extrema.

Thus we have established rules for evaluating force metrics that correspond with the points identified on the basis of the video footage.

4.3.4 Evaluation of the metrics

By implementing these rules in an algorithm, the six metrics were evaluated successfully for all 18 measurement runs. Correct identification was verified using the camera footage. The results that we are most interested in are the force at start and end of incision (corresponding to t_{p_2} and t_{p_3}) and the maximum force during the wedging phase (corresponding to t_{p_5}). These three metrics are presented in Figure 4.11.

The figure shows that the force at the start of incision is much smaller than

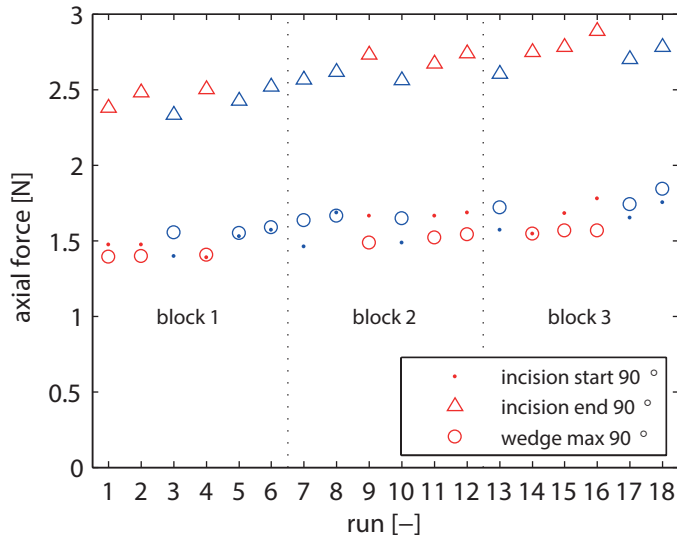


Figure 4.11: Force at start of incision, force at end of incision, and maximum wedging force, for all runs (blue 0°, red 90°)

that at the end of incision, and the maximum wedging force closely follows the former (similar experiments show this to be coincidental). All three metrics show positive trends, with linear regression slopes (95% confidence interval) of 0.017(0.010, 0.025), 0.026(0.019, 0.033), and 0.015(0.007, 0.024) respectively. Closer scrutiny of the data indicates that these trends are indeed functions of number of runs (re-use), and not of time.

No obvious influence of bevel orientation on the force at start of incision is observed, but the force at the end of incision does appear to be higher for the 90° group. The maximum wedging force, on the other hand, appears to be higher for the 0° group. These observations are supported by analysis of variance, taking into account the blocked design, with $F = 0.41$ ($p = 0.54$), $F = 7.69$ ($p = 0.02$), and $F = 127.2$ ($p < 0.01$), respectively. Block effects were present, although most likely due to the re-use trend ($p < 0.01$). No significant block-treatment interactions were observed ($p > 0.15$).

4.4 Discussion

4.4.1 Interpretation of the results

A needle with back bevel was used to puncture uniaxially tensioned polyurethane membranes at a speed of 20mm/s. The orientation of the bevel with respect to the membrane was varied in order to allow assessment of quasi-anisotropic ef-

facts of uniaxial tension. Membrane displacement was estimated on the basis of high-speed video footage. Knowledge of membrane displacement allowed calculation of the approximate needle insertion depth, leading to the establishment of an approximate relationship between axial force and details of needle tip geometry. On the basis of these observations, six force metrics were identified and related to initial contact, start of incision, end of incision, start of wedging, end of wedging, and friction. Subsequently, rules were established that allow objective identification and evaluation of these metrics on the basis of force alone, that is, without using the video information. Three of the metrics were examined for effects of needle reuse and bevel orientation.

The observed relation between axial force and estimated membrane displacement (Figure 4.6) suggests that the force is largely independent of the mode of interaction (contact, cutting, wedging, friction). This was expected because the axial force itself must arise from the membrane's overall resistance to deformation.

The rule-based identification of the initial contact point and local minima and maxima on the force curve, as implemented here, is sufficiently robust for the present dataset. However, the identification of the start of incision is more precarious, because the feature used for identification (a local minimum of the second derivative of force) can become indistinguishable after repeated use of the needle. Follow up experiments have shown that the start of insertion is more easily identified for new needles. With the proper caution, we expect the rules proposed here to perform well in similar puncture experiments with the same needle type.

Despite needle preconditioning, an effect of needle re-use was observed in the experiment. Although this effect is much smaller than with new needles, as found in similar experiments, it is still large enough to obscure the effect under study. Thus, if needles are reused, it is imperative that this factor be taken into account in the design and analysis of the experiment.

The reuse effect can be accounted for by experimental control (blocking) and by statistical control, e.g. by simple trend correction or analysis of covariance. In the current study, blocking by specimen ensured that at least part of the systematic variation due to reuse is explained, increasing the power of the analysis of variance. However, since variation between specimens appears to be negligible compared with effects of reuse, a randomized complete block design would probably have been a better choice in terms of statistical power.

Bevel orientation does not appear to influence the force characteristics in a qualitative sense, and no clear effect was observed in the video footage. Therefore, the same metrics can be used to characterize the force in either orientation. A quantitative effect of bevel orientation does appear to be present, affecting both the end-of-incision force and the maximum wedging force, but not the start-of-incision force. Although analysis of variance suggests that this effect is probably real, the effect size is relatively small. The fact that the end-of-incision force is slightly higher and that the maximum wedging force is slightly lower for the 90° case is in line with the expectation that the tension in the specimen tends to open

up the incision. The same goes for the observation that the final incision length for the 90° case is slightly higher, although it is not clear whether this is cause or consequence.

4.4.2 Limitations

If one is to establish a relation between axial force and geometric traits of a needle tip without resorting to pure speculation, some form of insertion depth measurement is indispensable. Direct visual observation, i.e. without recording, is perhaps easiest to accomplish, but this is only feasible at very slow insertion speeds ($v \ll 1\text{ mm/s}$). There is no guarantee that the force at higher insertion speeds has the same characteristics. At the insertion speeds typical for clinical procedures ($v > 1\text{ mm/s}$), synchronized measurement becomes necessary.

The manual estimation of membrane displacement from high speed video footage, although possible, has its limitations. Most importantly, the estimation process is subject to error due to limited image resolution and contrast, and due to selection bias and drift. Although video observations are more difficult to obtain and analyze than e.g. distance measurement using mechanical contact sensors or laser sensors, they have the advantage of providing much more insight in the actual process.

4.4.3 Conclusion

In conclusion, detailed video observation allowed us to identify force metrics and relate them to geometric details of the back bevel tip, without resorting to speculation. It proved possible to evaluate the same metrics on the basis of force alone, i.e. without visual corroboration, although the identification of the start of incision was less reliable. The sensitivity of the identified force metrics to variations in tip shape, membrane properties, and condition sets remains to be evaluated. Nevertheless, based on experience with similar experiments, we assert that identification of metrics based on video observation is a vital first step when experimenting with different needle shapes and specimen types. Under the present conditions the effect of needle reuse is strong, which implies that needle reuse has to be accounted for in experimental design and analysis. The use of a uniaxially tensioned specimen does not appear to restrict the generalizability of our findings. It remains to be seen whether these findings also apply during needle insertion into biological tissue.

Chapter 5

The effects of needle coating on puncture force

5.1 Introduction

The previous chapter identified and evaluated puncture force metrics for a specific needle tip geometry. In the present chapter, we investigate the influence of needle surface coating on these force metrics.

5.1.1 Background

A medical needle is largely defined by its tip geometry, and in the previous chapter it was shown that details of this tip geometry can be related to specific puncture force characteristics. However, tip geometry is not the only factor that influences the puncture force characteristics of a needle.

To improve penetration properties, medical needles are typically treated with a lubricant or coating. The ISO-7864 [4] standard for hypodermic needles suggests the use of surface coatings based on polydimethylsiloxane (PDMS), also known as silicone fluid. Some types of PDMS coating are used in liquid state [130], other types are cured (hardened) in order to improve surface adherence and robustness [131, 132].

A surface coating changes the interface between needle and tissue and thereby influences the interaction force, as confirmed by experiment in e.g. [22, 125, 133]. This raises the question to what extent the force metrics identified in the previous chapter are influenced by the surface coating.

5.1.2 Problem statement

The axial force during penetration of a polyurethane membrane using a back bevel tip was characterized in the previous chapter by three metrics: the force

at the start of incision, F_0 , the force at the end of incision, F_1 , and the maximum wedging force, F_2 . The end-of incision force, F_1 , was consistently the largest. All three metrics were found to increase with needle reuse.

Although these force metrics were related to geometric features of the tip, the influence of surface coating was not considered. It is possible that the force metrics change considerably due to surface coating, either qualitatively or quantitatively, or both. Moreover, the reuse effect observed in the previous chapter might be partially due to wear of the coating. Thus, in order to understand how the puncture force arises, it is necessary to investigate the influence of coating on the force metrics.

5.1.3 Related work

Some information concerning this topic should already be available in industry, as manufacturers are not likely to apply coatings without reason.

Contract research was performed as early as 1978 by Schneider et al. [133], who punctured human cadaverous skin with hypodermic needles of unspecified bevel type to investigate the influence of lubrication, among other factors. They found overall peak forces for unlubricated needles to be up to three times as high as those for lubricated needles. Similar results were found for unspecified artificial specimens in Schneider et al. [125]. Both studies considered only the overall peak force without explicitly relating this metric to geometric features of the tip.

The investigation by Stelman [22] specifically treated the influence of various lubricants on axial force, and showed that the maximum penetration force for bare needles in polyurethane membranes was up to three times as high as that for lubricated needles or coated needles. The relation between distinctive force characteristics and bevel geometry is discussed in that report, but only the overall peak force is considered in the investigation of the coatings.

Other sources investigate the effects of needle reuse [12, 134–136]. It is possible that wear of the coating is partly responsible for the reuse effect, but none of these sources explicitly considered the influence of surface coatings.

Thus, although the general influence of coatings has been investigated, the literature does not provide answers regarding the influence of surface coating on distinct force metrics.

5.1.4 Objective

The goal of the present investigation is to learn how the puncture force metrics for the back bevel needle, identified in the previous chapter as F_0 , F_1 , and F_2 , are influenced by surface coating. More specifically, we want to know whether wear of the coating represents an important contribution to the reuse effect.

5.1.5 Approach

Perhaps the most logical way to answer this question would be to compare the puncture force metrics for coated needles with those for uncoated needles. However, lacking the facilities to replicate medical-quality bevels and coatings, this was not an option. As an alternative, we devised a treatment that removes (or degrades) the existing coating from commercially available back bevel needles, and compare a treated group with an untreated group to see how the force metrics are influenced. Details of the investigation are provided below.

5.2 Materials and Methods

5.2.1 Equipment and instrumentation

Treatments are applied with the help of a 600ml glass beaker and an IKA RH BASIC laboratory heater (IKA-Werke GmbH, Staufen, Germany). The experimental set-up used to insert the needle and measure the forces is exactly the same as described in Chapter 4, except for the video camera, which is not used here. The set-up consists of an Aerotech PRO115-400 linear motion stage mounted vertically on a steel frame, equipped with an ATI nano17 six-axis force/torque sensor, and a custom built tension device to hold the specimens.

5.2.2 Specimens

Specimens too are the same as in the previous chapter. Six specimens are available. They are cut to a size of $200\text{mm} \times 8\text{mm}$ from a single piece of Platilon U 4201 AU thermoplastic polyurethane film, 0.3mm thick. Specimens are welded end on end to create a loop that fits the tension device. Specimens are suspended in uniaxial tension (0.4N), with a free standing length of 30mm and clamped boundary conditions.

5.2.3 Needles

As in Chapter 4, back bevel needles from a Vygon Biovalve IV cannula are used in this investigation. Six needles are available. Needle diameter is 1.5mm , length 70mm , and tip length is 4.5mm . It is known that these needles receive some kind of silicone-based lubricant or coating during the manufacturing process, but the specific type and the method of application are unknown.¹ This complicates the search for a surface cleaning treatment.

¹The needle manufacturer would not share this information

5.2.4 Surface treatment

Assuming that the needles comply with the ISO standard [3], it is likely that the lubricant or coating is based on polydimethylsiloxane (PDMS) [132], either uncured or cured. Suggested methods for breaking down *cured* PDMS coatings involve the use of strong (alkaline) detergents, e.g. based on potassium hydroxide, as typical organic solvents have no effect [131]. The same approach should work for *uncured* PDMS-based lubricants, although these could also be removed using organic solvents [130, 132]. As the use of a detergent should work in both cases, regardless of the type of PDMS coating, we adopt this approach.

Two treatment solutions are used here: a_1 and a_2 . Solution a_1 is the control and consists of 115ml tap water. Solution a_2 consists of 100ml tap water with 15ml (i.e. 13%v/v) RBS T 120 (Chemical Products R. Borghgraef S.A., Brussels, Belgium), which is a detergent based on potassium-hydroxide .

Directly after removal from their sterile packaging, the needles are suspended in a glass beaker, filled with 115ml treatment solution, so that the tips are submerged approximately 15mm. Treatment consists of soaking the needles at 60°C for 2.5 hours. This is followed by a thorough rinse using hot tap water (77°C). The utmost care is taken (before, during, and after treatment) to ensure that the needle tip does not touch anything other than the treatment solution, so as to prevent mechanical damage.

5.2.5 Insertion parameters

To evaluate the treatments, a total of 36 penetration runs were performed at a constant speed of 20mm/s, both for insertion and retraction, with a 30mm stroke. Initial distance to the specimen was approximately 5mm, to ensure that a constant speed was reached before making contact with the specimen. Puncture locations were 33mm apart, allowing six runs per specimen. The direction of motion was normal to the specimen surface, and the slip angle, i.e. angle between velocity vector and longitudinal axis of the needle, was smaller than two degrees. The bevel orientation was 0°, so that the incision was in line with the direction of tension in the specimen.

5.2.6 Experimental design

The experiment is designed with a focus on the interaction between surface treatment (factor A) and needle reuse (factor B), that is, we are mainly interested in the interaction $A \times B$.

Factor A (surface treatment) has fixed levels $a_1 = control$ and $a_2 = detergent$, as described in the previous section. Factor B (needle reuse) has fixed levels $b_1 = 1^{st}use$, $b_2 = 2^{nd}use$, ..., $b_6 = 6^{th}use$, which represent sequential repeated measurements . Blocking factor S (needle) is introduced to isolate effects of needle heterogeneity, which are considered a nuisance. As the available needles

represent a small sample from a large population, the levels of factor S are considered to be random.

Since each needle can only receive one surface treatment, the available needles are randomly divided into two groups of three needles, $s_{1(1)}, \dots, s_{1(3)}$ and $s_{2(1)}, \dots, s_{2(3)}$, and treatments are assigned randomly to these groups. Needles are then randomly allocated to runs with the restriction that each needle is used once per specimen, resulting in Table 5.1. This restriction confounds the reuse (factor B) with the specimen factor, but we observed in previous experiments that the variability due to specimens was negligible.

The resulting experimental design can be interpreted as a split-plot factorial design Kirk [137], Oehlert [138] with the following model:

$$y_{ijk} = \mu + \alpha_i + \pi_{k(i)} + \beta_j + (\alpha\beta)_{ij} + (\beta\pi)_{jk(i)} + \epsilon_{ijk} \quad (5.1)$$

where y_{ijk} is the observed response for needle k in surface treatment group a_i for reuse-level b_j , where $i = 1, \dots, p$, $p = 2$, $j = 1, \dots, q$, $q = 6$, and $k = 1, \dots, n$, $n = 3$. On the right hand side, μ is the overall population mean, α_i is the (fixed) effect of surface treatment, β_j is the (fixed) effect of needle reuse, $\pi_{k(i)}$ is the (random) effect of needle $s_{k(i)}$, $(\alpha\beta)_{ij}$ is the combined (fixed) effect of surface treatment and needle reuse, $(\beta\pi)_{jk(i)}$ is the combined (random) effect of needle reuse and needle, and ϵ_{ijk} is the (random) experimental error.

Thus, the model assumes that the effect of needle reuse may be different for each level of surface treatment (i.e. interaction between A and B), and also for different needles (i.e. interaction between S and B). Note that S implicitly includes A , i.e. $S = S(A)$, because each needle is associated with a single surface treatment.

Table 5.1: Random allocation of conditions to runs u_r ($r = 1, \dots, 36$)

		A (treatment) and needle number					
		water			detergent		
		2	5	6	1	3	4
B (use)	1	u_5	u_3	u_1	u_6	u_2	u_4
	2	u_8	u_{12}	u_7	u_{10}	u_8	u_{11}
	3	u_{18}	u_{13}	u_{16}	u_{17}	u_{15}	u_{14}
	4	u_{19}	u_{20}	u_{23}	u_{21}	u_{24}	u_{22}
	5	u_{27}	u_{28}	u_{25}	u_{26}	u_{29}	u_{30}
	6	u_{35}	u_{32}	u_{33}	u_{34}	u_{36}	u_{31}

5.2.7 Analysis

The force metrics, F_0 , F_1 , and F_2 , are evaluated for all runs, using the methods from Chapter 4. Analysis of variance is used to test for an interaction effect $A \times B$ ($H_0 : (\alpha\beta)_{ij} = 0$) and to test for main effects of B ($H_0 : \beta_j = 0$) and A ($H_0 : \alpha_i = 0$), based on Eq. 5.1.

5.3 Results

Figure 5.1 compares a single measurement from the control group with a single measurement from the detergent group. The figure illustrates that the metrics F_0 , F_1 , and F_2 can be distinguished in both groups. One striking feature is that the force peak related to wedging (F_2) is much higher and more pronounced for the detergent needle than that for the control needle. Another important observation is that the force increases dramatically after puncture is complete, i.e. after approximately 15mm , for both needles. This is contrary to the findings in Chapter 4, as will be discussed later. In the following analysis we consider only the first half of the time-series.

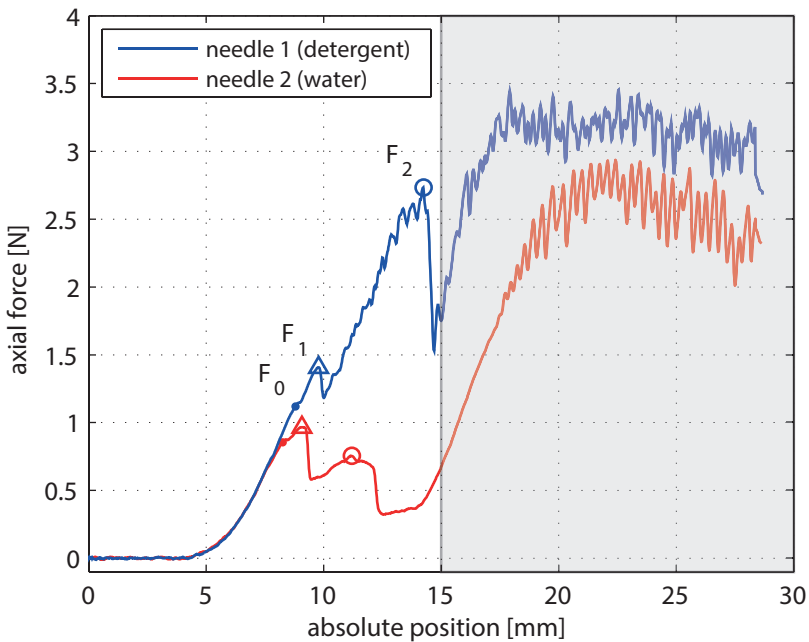


Figure 5.1: Representative examples of force response during first use (b_1) of needles from both treatment groups (a_1, a_2), showing automatically identified metrics.

To evaluate the consistency of the force response, the range of forces for all runs with all needles is presented in Figure 5.2. This figure shows that the characteristics for individual needles are consistent, but differences between needles are considerable. The control group and treated group can be distinguished clearly. Needle 4 from the detergent group shows aberrant behavior.

Focusing only on the first half of the time-series, the three force metrics F_0 , F_1 , and F_2 , were successfully evaluated using the rules proposed in the previous

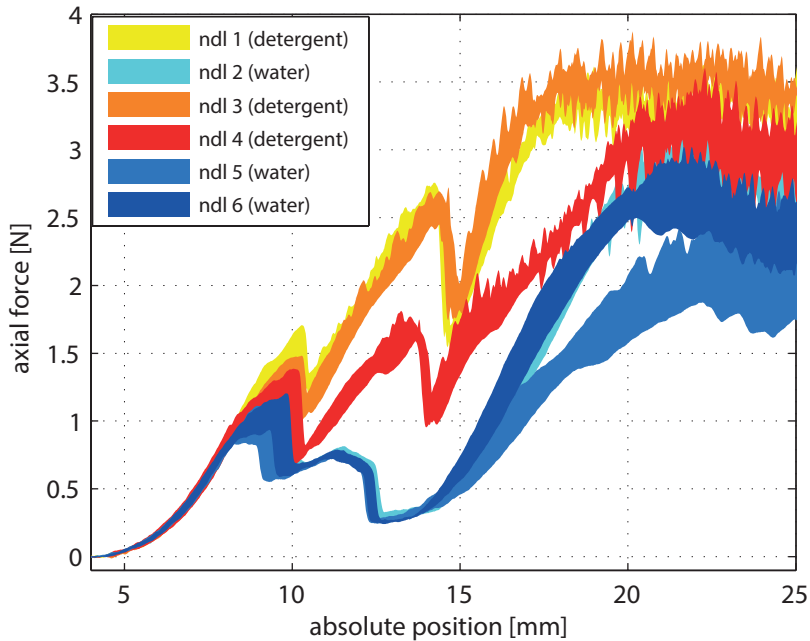


Figure 5.2: Range of force, based on six runs per needle ($q = 6$).

chapter. The resulting force metrics are presented in Figure 5.3 as a function of needle use. The figure clearly shows an upward trend in F_0 and F_1 , both for the control group and the treated group. For F_2 , however, this trend is not so obvious. The values of all metrics for the treated group are consistently higher than those for the control group, with the exception of three observations for needle 4. The observed differences between control and treated group are by far the largest for the F_2 metric, i.e. the maximum wedging force.

Interaction plots showing the marginal means² for each of the metrics are presented in Figure 5.4. A main effect for A (surface treatment) appears to be present for all metrics, and is especially strong for F_2 . There appears to be a slight upward trend in the control group and a slight downward trend in the detergent group for F_2 as a function of reuse (B), which could indicate a weak interaction. No obvious $A \times B$ interaction is observed for F_0 and F_1 .

The analysis of variance corresponding to Figure 5.4 is presented in Tables 5.2 to 5.2. Evaluation of the sample covariances showed that the multisample sphericity assumption is not tenable, as illustrated by the parameter $\hat{\epsilon}$ which should be close to 1 for spherical data. This implies that the F -test for B and $A \times B$ will be biased towards rejection [137, 139, 140]. For that reason, we consider the adjusted probability p_a , which is based on an F distribution with reduced degrees

²Marginal means for one factor are the pooled means over all levels of the other factors

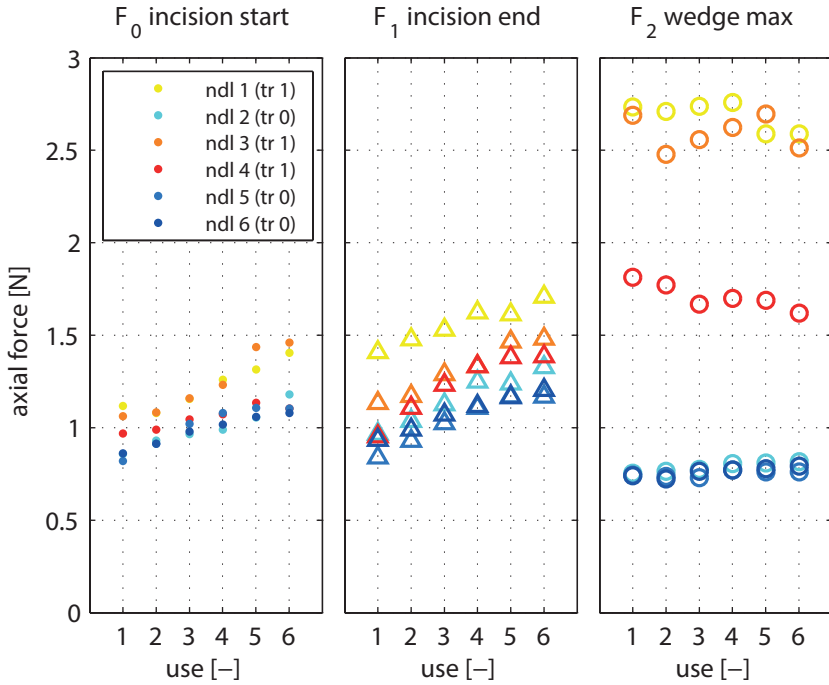


Figure 5.3: Individual puncture force metrics F_0 , F_1 , and F_2 as function of needle use, for all needles. Note that some points for F_0 overlap.

of freedom, i.e. the original degrees of freedom multiplied by $\hat{\varepsilon}$ [137].

Assuming a conservative level of significance, $\alpha = 0.01$, these tables show that the interaction effect $A \times B$ is not statistically significant for any of the metrics. The main effect of B is clearly significant for F_0 and F_1 , but not for F_2 . The main effect of A is significant for F_2 , but not for F_0 and F_1 . Based on these results we can reject $H_0 : \alpha_i = 0$ for F_2 , and we reject $H_0 : \beta_j = 0$ for F_0 and F_1 .

Table 5.2: Analysis of variance for F_0 , where p is the conventional probability and p_a is the adjusted probability for $\hat{\varepsilon} = 0.368$.

Source	<i>SS</i>	<i>df</i>	<i>MS</i>	<i>F</i>	<i>p</i>	<i>p_a</i>
A: surface tr.	0.275	1	0.275	8.60	0.043	
<i>S(A)</i>	0.128	4	0.032			
B: use	0.353	5	0.071	28.23	0.000	0.000
$A \times B$	0.012	5	0.002	0.95	0.472	0.423
$B \times S(A)$	0.050	20	0.003			
Total	0.817	35				

Table 5.3: Analysis of variance for F_1 , where p is the conventional probability and p_a is the adjusted probability for $\hat{\varepsilon} = 0.413$.

Source	<i>SS</i>	<i>df</i>	<i>MS</i>	<i>F</i>	<i>p</i>	<i>p_a</i>
A: surface tr.	0.683	1	0.683	6.94	0.058	
<i>S(A)</i>	0.394	4	0.099			
B: use	0.524	5	0.105	75.01	0.000	0.000
$A \times B$	0.002	5	0.000	0.29	0.912	0.761
$B \times S(A)$	0.028	20	0.001			
Total	1.631	35				

Table 5.4: Analysis of variance for F_2 , where p is the conventional probability and p_a is the adjusted probability for $\hat{\varepsilon} = 0.328$.

Source	<i>SS</i>	<i>df</i>	<i>MS</i>	<i>F</i>	<i>p</i>	<i>p_a</i>
A: surface tr.	21.993	1	21.993	25.25	0.007	
<i>S(A)</i>	3.485	4	0.871			
B: use	0.018	5	0.004	1.46	0.245	0.291
$A \times B$	0.036	5	0.007	2.86	0.042	0.132
$B \times S(A)$	0.050	20	0.002			
Total	25.581	35				

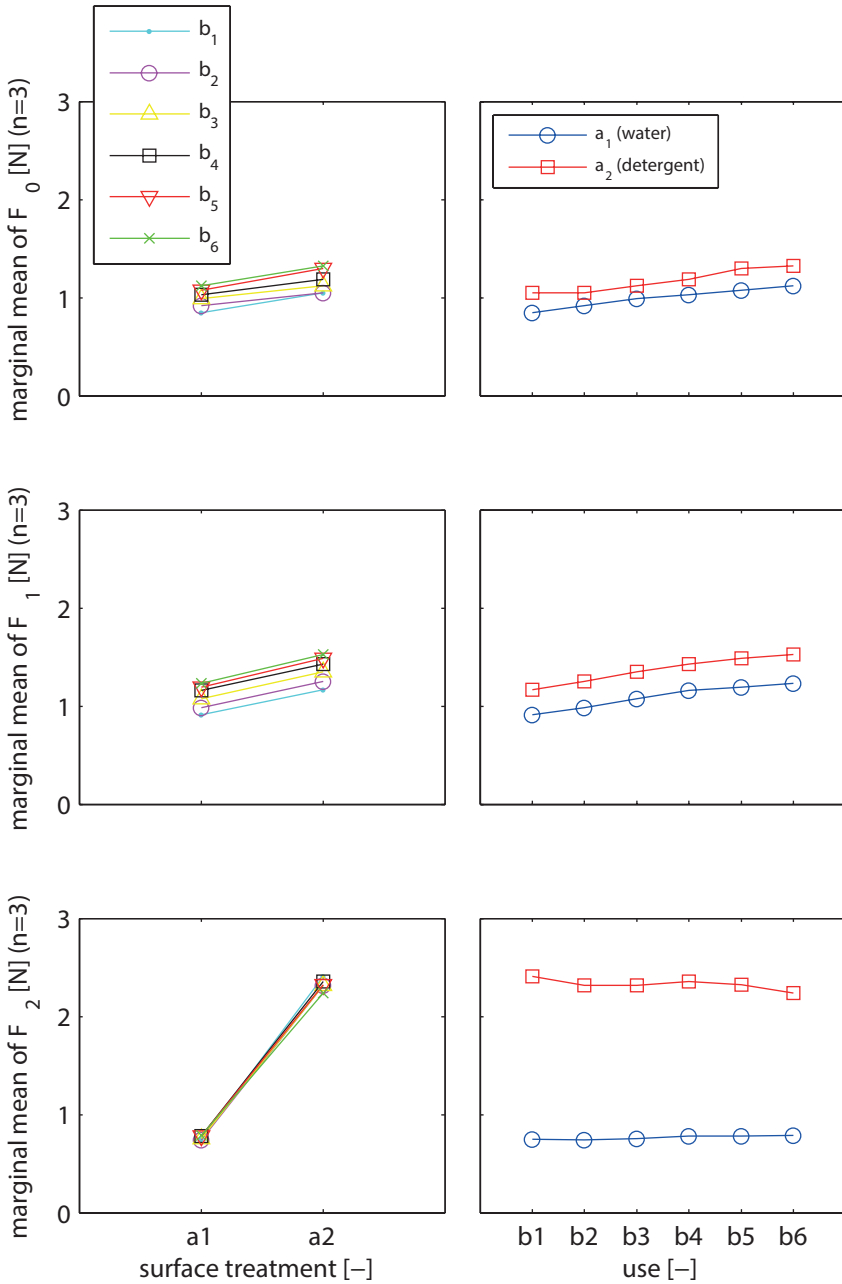


Figure 5.4: Interaction plot, showing the marginal means for the maximum wedging force (F_2). Note that each point represents the mean of three observations.

5.4 Discussion

5.4.1 Interpretation

To investigate the influence of needle surface coating on puncture force metrics F_0 , F_1 , and F_2 for the Biovalve needle, we compared the puncture forces from two groups of needles. The control group was treated with water, which should have no effect on the coating. The other group was treated with a detergent based on potassium-hydroxide which should remove the coating from the needles. To evaluate the effects of these treatments, a total of 36 insertions were performed.

Needles from the detergent group were easily distinguished from those in the control group by inspection of the force response. The observed values of the force metrics for the detergent group were consistently higher than those for the control group. The large increase in maximum wedging force F_2 , up to 200%, was particularly striking.

From 5.3 it appears that a rather strong main effect of reuse is present for F_0 and F_1 in both treatment groups. Analysis of variance suggests that this was not by accident (both $p_a < 0.0005$). The figure also suggests that there may be a small effect of reuse for F_2 in the control group, as in Chapter 4, and that there is an opposite effect for the detergent group. However, the analysis of variance did not detect a main effect of reuse for F_2 . It is possible that a small effect is obscured by the relatively large variability in the detergent group.

A main effect of A was not detected for F_0 and F_1 , but judging from the interaction plots it seems likely that this effect is indeed present, but that it is obscured by the systematic variance caused by reuse.

No interaction was detected between surface treatment (A) and reuse (B) for any of the metrics. This implies that, although there is a considerable main effect of surface treatment, it does not noticeably influence the reuse effect. If there is an influence for F_0 and F_1 , it is likely to be small. For F_2 it is again possible that a small interaction effect is obscured by the variability in the detergent group. Assuming that the surface treatment successfully removed the coating from the needles, it can be concluded, tentatively, that the presence of a coating does not noticeably influence the reuse effect.

5.4.2 Limitations

The matter of test validity requires some attention. Instead of directly manipulating the coating (e.g. application vs no application), we applied a surface treatment that was supposed to remove an existing coating. The efficacy of this removal treatment, however, is difficult to assess [131]. Moreover, it is possible that the treatment not only removed the coating but also modified the metal surface in some way. Investigation by optical microscopy did not show noticeable differences in surface appearance between the needles in the control group and the detergent group. However, large differences in penetration force were observed between groups. The fact that the forces were altered considerably by the

detergent implies that the treatment must have had some effect on surface quality, but we cannot say with certainty that the coating was completely removed.

The split-plot design, although well suited for the evaluation of the interaction effect, is relatively inefficient for the evaluation of the main effect of surface treatment A . This implies low power, which not only limits the detectable effect size, but also tends to exaggerate effects that *are* detected [141]. Nevertheless, the main effect of surface treatment, on the wedging force in particular, is difficult to deny: In over a hundred insertions using the same needle type with original coating, as e.g. in the previous chapter, the wedging force peak (F_2) was always much lower than the incision peak (F_1), but the opposite was observed for the detergent group in the current experiment. For the control group the global maximum peak corresponds to F_1 (cutting), whereas for a needles in the detergent group the global maximum corresponds to F_2 (wedging). Thus, direct comparison of overall peak forces, as in e.g. [22, 125], amounts to comparing the results of two different phenomena, like comparing apples and pears.

The force after puncture was found to increase dramatically for all needles, as illustrated by Figure 5.2 (after 15mm). This behavior was consistent within needles but varied between needles, and it is contrary to the observations from the previous chapter, in which the force after puncture appeared to remain constant. However, it is possible that the insertions in Chapter 4 were stopped before the increase could occur. Attempts to recreate a constant force response with other needles were unsuccessful.

After puncture, the transfer of force can only be due to a combination of friction and normal forces on the cannula. The observed increase in force, then, could be due to increased friction or due to a nonzero slip angle (angle between velocity vector and longitudinal axis of the needle). The latter seems the most likely, as both needle and specimen are clamped, and the hole created by the asymmetric bevel is not exactly in line with the longitudinal axis of the needle. Fortunately, this problem does not appear to influence the puncture process and the corresponding findings.

5.4.3 Conclusion

The use of detergent was found to produce small increases in the incision force metrics F_0 and F_1 , and a large increase in the maximum wedging force F_2 . Both treatment groups showed a large effect of needle reuse for F_0 and F_1 , but not for F_2 . Interaction between surface treatment and reuse was not observed for any of the metrics. This suggests that normal wear of the needle surface coating does not represent a noticeable contribution to the reuse effect.

Chapter 6

Kidney puncture forces in a human cadaver

6.1 Introduction

Chapters 4 and 5 dealt with needle insertion experiments using artificial specimens of uniform quality in a well controlled laboratory environment. However, actual needle interventions are performed on living organisms (humans), which are much more difficult to control and have a high degree of intrinsic variability. The measurement of needle-tissue interaction forces in such an environment, or in any kind of biological tissue, is quite challenging. To illustrate this point, the current chapter presents an exploratory study aimed at characterizing the variability encountered when puncturing human cadaverous kidneys.

6.1.1 Background

Needle interventions are characterized by a lack of direct visual feedback: there is no direct view of the needle tip inside the body. This makes needle interventions difficult to perform. In the absence of direct visual information, the clinician needs to rely on other sources of information, and one of those is the insertion force. As the insertion force arises from needle-tissue interaction, it stands to reason that this force may contain information that can help determine which type of tissue the needle is located in. Kidney catheterization (nephrostomy) is one example from clinical practice where clinicians are taught to use this information [142].

The nephrostomy procedure is carried out in case of blockage inside the kidney, in order to drain excess urine. The procedure involves the insertion of a long needle into the patient's back, through skin and underlying tissue and into one of the kidney's calyces. A catheter can then be placed for drainage.

For an impression of the anatomical structures that are punctured during the

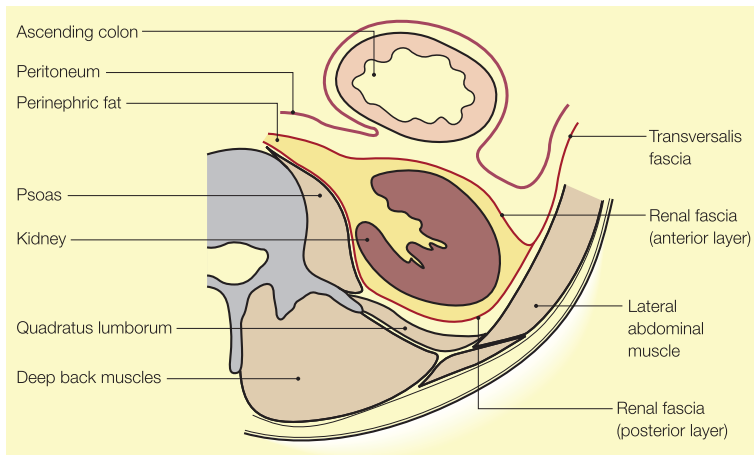


Figure 6.1: Transverse section of the kidney and surrounding anatomy, showing the muscles of the back with their fascia, the posterior renal fascia, the renal capsule, and part of the collecting system (adapted from [143], © 2002 Elsevier).

procedure, Figure 6.1 presents a transverse section of the kidney and the surrounding region. Inspection of this figure shows that there may be between three and seven fascia layers (muscle and renal) that need to be traversed before entering the kidney through the renal capsule.

To facilitate the training of clinicians for the needle insertion part of the nephrostomy procedure, training simulators with force feedback may be used. However, if force feedback is to be presented as a source of information, then it is imperative for this feedback to be grounded on empirical data.

6.1.2 Problem statement

In order to establish and/or validate mathematical models of the interaction between needle and tissue during the nephrostomy procedure, it is necessary to gain insight into the forces that arise during needle insertion into human patients.

One may wonder, for example, how large the puncture forces are during needle insertion, and whether the forces that arise during fascia puncture are different from those during capsule or calyx puncture. Dyer et al. [142] describe two “tactile pops” that are said to occur when the needle punctures the renal capsule and the collecting system (calyces) respectively.

This implies that force data from needle insertions into human kidneys need to be obtained and analyzed.

6.1.3 Related work

It is natural to look to the literature first, to see whether this problem has already been tackled [12]. Force measurement data from needle insertions into *kidney* tissue appear to be scarce in literature. Such data are presented by [52, 108] (porcine kidney in vitro), [65] (porcine kidney in vivo), and [48] (bovine kidney in vitro, unpublished source).

However, no data were found in literature related to needle insertions into human kidney. Thus, original data need to be gathered.

6.1.4 Research Objective

The current work represents a preliminary investigation of the forces that arise during needle insertion, through the skin, into one of the kidneys of a human cadaver. The objective is to obtain an initial characterization of the forces that arise during needle insertion into the human kidney. The forces are characterized in terms of friction force, peak force, and perceived stiffness. Where possible, these metrics are to be related to specific tissue structures.

6.2 Materials and Methods

6.2.1 Materials

Test specimen

A single female specimen was available for the test, 85 years old at the time of death, with a height of 158cm and weight of 50kg. Subject had a history of osteoporosis, rheumatism and arthrosis, and had an open skull defect and a rectus-sheath hernia in the lower abdomen. The right renal pelvis was dilated.

Environment

The measurements were performed in a dissection room at the Maastricht University Medical Center's Department of Anatomy and Embryology. Temperature in the dissection room was maintained at a steady 16°C.

Technical equipment

The specimen was placed on a mobile dissection table with adjustable working height (Thalheimer Kuehlung GmbH, Ellwangen, Germany).

The measurement apparatus, depicted in Figure 6.2, consists of a linear motion stage equipped with load sensor, mounted to a frame composed of steel tubing. The frame allows adjustment of the needle-insertion direction within a range of approximately $\pm 70^\circ$ from vertical.

An Aerotech PRO115-400 linear stage with 400mm travel and 5mm/rev ball screw (non-backdrivable) is used to move the needle (Aerotech Inc., Pittsburgh, USA). The stage is driven by a 48V 120W Maxon EC40 brushless motor controlled by a Maxon 4-Q-EC servoamplifier (Maxon Motor AG, Sachseln, Switzerland). Motor position is measured using an optical Scancon 2RMHF-7500 incremental rotary encoder with 7500 pulses per revolution (Scancon A/S, Allerød, Denmark). The positioning-accuracy of the linear stage in combination with this encoder is at least 12 μ m with a repeatability of 1 μ m, according to manufacturer's specifications.

The needle is attached to an ATI nano17 six-axis force/torque sensor (ATI Industrial Automation, Apex, USA), with a rating of 17N and resolution of 0.003N in insertion direction (calibration SI-12-0.12), which is mounted to the moving platform of the linear stage by means of a bracket.

Data acquisition and position control of the linear stage are achieved using a dedicated PC (AMD Athlon 64 X2 5200+, 3GB RAM, MS Windows XP Pro SP3) equipped with a dSPACE DS1104 real-time controller board (dSPACE GmbH, Paderborn, Germany). Data signals are sampled at 2.5kHz with 12bit resolution. Capture time was limited to 40s maximum, due to system specifications.

The following variables were stored on the computer: 1. forces and moments along all three axes; 2. time stamp; 3. stage position; 4. operating state (run, pause, retract).

In addition to the force measurements, images from a video camera and an ultrasound (US) machine were recorded at 25fps (frames per second) using a custom-made video capture system (Noldus Information Technology, Wageningen, The Netherlands). An audio signal produced by the force measurement system was recorded with the ultrasound images, for data synchronization purposes.

An Acuson Sequoia 512 ultrasound machine was used, equipped with a convex Acuson 6C2 6MHz probe (Siemens AG, Erlangen, Germany). The ultrasound probe was held in position by an experienced clinician, so as to maintain a clear view of the needle during insertion and to ensure that the needle reached the desired location. It was verified that varying pressure from the ultrasound probe did not noticeably affect the insertion force measurements.

Needles

Two 20cm-long 18G Trocar Needles with Echotip (Cook Medical, Bloomington, USA) were available for the measurements. This type of needle is typical for the nephrostomy procedure Dyer et al. [142], and consists of a blunt 1.3mm diameter cannula, with an ultrasound-reflecting grating (Echotip), and a 1.0mm diameter stylet with a diamond-shaped cutting tip (three faces). A close-up of the needle point is presented in Figure 6.3.

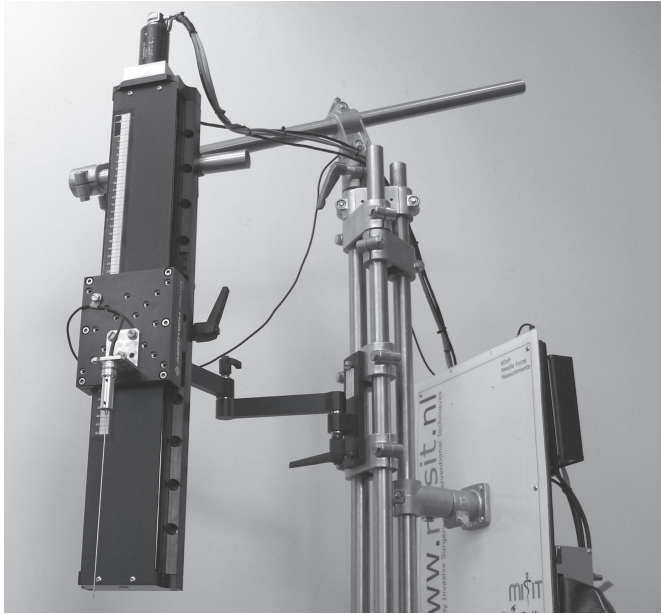


Figure 6.2: Measurement apparatus consisting of linear motion stage with six-axis force/torque sensor mounted to adjustable frame

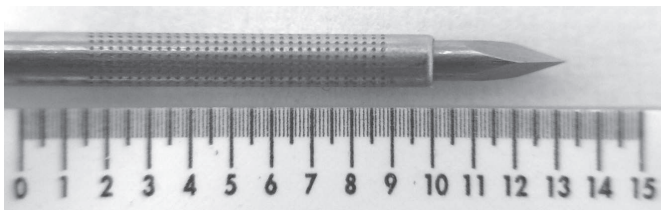


Figure 6.3: Close-up of the trocar-needle point, clearly showing the blunt cannula with ultrasound-reflecting grating and the diamond shaped cutting stylet (scale in *mm*)

6.2.2 Methods

Preparation of test specimen

The subject was injected six hours post-mortem with a 2% formalin solution (total 1.0l). This was followed by a solution of 2% formalin, 5% x-ray contrast (Telebrix Gastro), and 12.5% PEG300 (total 2.25l) injected ten hours post-mortem. For use in another study, CT-images of the whole body were obtained 12 hours post-mortem, directly followed by MRI-imaging of the torso. Fourteen hours post-mortem the subject was frozen at -30°C , after which it was kept in frozen condition for eighty days. After this period, during the three days leading up to the measurements, the subject was defrosted at 16°C inside a closed bag.

Test procedure

After ensuring that core temperature of the specimen had reached ambient room temperature (16°C), measurements on the kidney were performed over a period of one day.

At least three people were present at all times during the measurements, one operating the measurement apparatus and video equipment, one operating the ultrasound equipment, and one or more for positioning the specimen and orienting the linear stage.

Before starting the measurements, the region of interest was examined using ultrasound and a needle was inserted manually so as to obtain a reference for positioning and orienting the linear stage. A grid was drawn on the skin in the region of interest, for reference when choosing an insertion point.

Kidney measurements were performed in the morning, over a period of three hours, with the specimen in prone position (i.e. lying face-down). Measurements were obtained from the right kidney. The needle was inserted below the costal margin, in cranial direction, at approximately 30° (about the anteroposterior axis) with respect to the sagittal plane, as depicted in Figure 6.4. The smallest angle between needle and skin was approximately 50° (measured with a protractor). In accordance with the clinical procedure, a scalpel was used to make an incision through the epidermis and dermis before each needle insertion. Due to anatomical restrictions, the ultrasound probe was positioned for an out-of-plane approach of the needle (i.e. the angle between ultrasound plane and longitudinal needle axis is non-zero).

A constant speed of 10mm/s was used for needle insertion and retraction, to ensure repeatability of the motion. This value was based on both the opinion of the experienced clinicians present and on data available in the literature [12].

Insertion locations were chosen (in quasi-random order) by the clinician, with several millimeters in between so as to ensure that the needle would not follow an existing path. The needle was replaced by a fresh one halfway through the experiment, following difficulties during insertion.

Within the limited time frame, the needle was inserted (and retracted) a total of 19 times in the kidney region. This was done according to the protocol outlined

Table 6.1: Protocol for a single needle insertion/retraction run

1. determine desired insertion location and orientation based on ultrasound footage of previous insertion
2. reposition and reorient the linear stage and the specimen (if necessary)
3. advance needle until almost in contact with tissue
4. specify needle insertion distance
5. start video capture
6. start needle insertion at constant velocity (data capture starts automatically)
7. maintain US view of needle to assess whether target is reached
8. if necessary, advance needle further
9. assess needle placement using ultrasound (find approximate tip location)
10. fully retract needle at constant velocity
11. stop video capture (data capture stops automatically)

in Table 6.1.

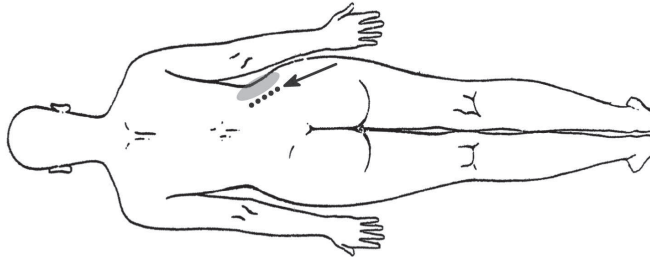


Figure 6.4: Location and direction of needle insertion (dots and arrow, respectively) and location of US-probe (gray spot) (posterior view)

Data pre-processing

The dataset obtained from this experiment consists of time histories of needle loads and positions, with corresponding ultrasound images and video recordings. An audio signal produced by the dSPACE system during needle motion was recorded with the ultrasound images.

Using the audio signal, force and position data are synchronized with the ultrasound and video data. This is done manually. Subsequently the ultrasound data are examined in order to identify any noticeable events, such as puncture of the renal capsule or calyces. For every such event, the time stamps from the ultrasound recording are used to find the corresponding insertion force and posi-

tion. Video recordings are used to investigate any anomalies and to review voice comments where necessary.

Of the loads acting on the needle hub, only the force in the direction of needle insertion is considered in the analysis (henceforth simply referred to as force). For the sake of discussion, compressive forces are taken positive, contrary to common convention.

For every measurement, reference values are established for both force and position. The median of the force during initial free-air movement is used as the zero-reference for the force signal. The point of first contact between needle and tissue is used as zero-reference for the position.

A two-pass (zero-lag) moving average filter is employed to reduce noise in the digitized signal. A minimal window size of two samples is used (for each pass) to limit attenuation of the peaks.

Since only the (local) extrema of the insertion part of the filtered force signal are of interest, these extrema are identified by differentiating and then locating zero-crossings. The resulting subset is referred to as the insertion-extrema-signal.

A line-simplification algorithm (following [144]) is subsequently employed to reduce the number of points in the insertion-extrema-signal, so as to enable automated peak selection. Simplification is necessary in order to distinguish relevant extrema in the signal, e.g. those due to major puncture events, from irrelevant extrema, e.g. those due to small fluctuations and noise. Note that this distinction is subjective.

The simplification algorithm produces a subsample of the original data signal (i.e. an interpolating approximation), based on a user specified error threshold ϵ , that retains the most important qualitative aspects of the signal. The maximum normal distance from the simplified line to the original signal is used as the error metric. This metric is evaluated in dimensionless force and position coordinates, using force sensor rating (17N) and needle length (200mm), respectively, as the scaling quantities.

Examples are given in the results section. Evaluation of the peak force metrics is based on the simplified insertion-extrema-signal, whereas evaluation of the friction metric is performed on the filtered retraction signal.

Evaluation of the force metrics

At this point, a modeling assumption is made: The insertion force is assumed to consist of two (potential) contributions, as described in Chapter 2, viz. a force concentrated at the tip, representing pre-puncture loading, puncture or cutting interactions, and a force distributed along the length of the needle, representing friction. For each needle insertion, both the friction and puncture components are analyzed.

The force measured during needle *retraction* is assumed to be due to friction alone, since the tip does not do any work in this phase (consistent with e.g. [28]). The friction force is approximated here by a constrained piecewise linear least-squares fit to the filtered retraction data. This friction force approximation is used

as a baseline for correction of the peaks that occur during needle *insertion*.

The approximated friction force during retraction is adjusted for position, such that the position of the global maximum force during retraction coincides with the end position of the insertion phase, and is then used to correct the simplified insertion-extrema-signal. The resulting (friction-)corrected force signal is assumed to be a rough approximation to the tip force (i.e. due to cutting and puncture only).

It is stressed here that the corrected force signal is a subselection of the filtered force signal during insertion, reduced by the estimated friction at corresponding insertion positions. We interpret each local maximum (henceforth referred to as peak) of the corrected force signal as an indication of a puncture event, i.e. a local tissue-failure event.

The slope of the simplified line segment just before the peak, which is a secant line to the original (friction-corrected) signal, is used to represent the perceived stiffness. Note that this is a compound stiffness measure that may include actual stiffness contributions from all the tissue structures surrounding the needle, but may also include non-elastic friction and cutting components.

The estimated friction slopes are evaluated for each run, and friction-corrected peak forces and slopes are evaluated for all peaks in each run. The distribution of the pooled metrics (i.e. all peaks from all runs combined) is approximated by fitting a lognormal distribution. This corresponds to fitting a normal distribution to the (natural) logarithm of the observed data. Note that a normal distribution cannot apply because it is defined on the entire real line, whereas our metrics are all strictly non-negative.

The goodness-of-fit of the estimated distributions is assessed using the Anderson-Darling test for normality (on the log-transformed data) [145, 146]. The Anderson-Darling statistic, A^2 , represents the discrepancy between the theoretical and empirical distribution functions (smaller is better).

Individual observations that can be related to specific tissue structures, on the basis of ultrasound, are discussed separately.

6.3 Results

Out of nineteen runs, ten (runs 4 to 11, 13 and 14) were successfully completed. Incomplete runs (due to e.g. missing retraction data, needle buckling, etc.) are not considered here.

6.3.1 Ultrasound

A single ultrasound frame (from run 13) is presented in Figure 6.5. This is one of the clearest examples obtained. The figure shows the approximate location of the needle tip inside the kidney. Due to the out-of-plane approach, only a small part of the needle is visible at any time, so the clinician had to search for the approximate tip location at the end of every insertion.

It is important to realize that, by manipulating the position and orientation of the ultrasound probe in real time, it is possible for the experienced clinician to construct a three-dimensional (mental) image so as to confirm whether the needle is indeed located inside a calyx. After the fact, using only ultrasound recordings, this becomes much more difficult, especially if the corresponding positions and orientations of the probe are not known.

The actual moment at which the needle contacts the kidney cannot be seen directly in the ultrasound footage, due to the out-of-plane approach. However, it can be estimated, roughly, by retracing the path of the needle, taking into account its constant speed.

Moreover, from separate ultrasound and force observations it was found that, as the needle tip is retracted through what is probably the kidney capsule, the needle's echogenic grating tends to cause a local increase in friction, resulting in a slight bump in the retraction-force signal (as depicted in Figure 6.6). This bump occurs in every run, and its location is consistently close to the ultrasound-based estimate of kidney contact.

For this reason, the bump location is used as an estimated boundary location. This boundary divides the insertion data into two regions, region 1 for subcutaneous tissues, and region 2 for kidney tissue. The estimated boundary position (approximate distance from skin) ranged from 31mm to 46mm , with a median of 38mm ($n = 10$). It is emphasized that these are very rough estimates, with errors as large as $\pm 5\text{mm}$.

In addition to the estimation of the tissue boundary location, thus creating a rough division between forces related to the intermediate tissues and those related to the kidney, an attempt was made to identify which force peaks correspond to calyx entry. Calyx entry was confirmed by the experienced clinician, based on ultrasound examination, in all but two runs (runs 8 and 11).

Calyces appear in the ultrasound image as dark (hypo-echoic) spots, whereas the needle appears as a bright (hyper-echoic) spot, as depicted in Figure 6.5. If at one point in time a bright spot (representing the needle) appears inside a dark spot (representing a calyx), then it should be safe to assume that the needle has entered the calyx. However, this could only be confirmed during needle retraction.

The positions at which needle presence in a calyx was confirmed (during retraction) ranged from 47mm to 91mm with a median of 55mm ($n = 8$). The error in this position estimation, due, in part, to differences in tissue displacement during insertion and retraction, may be as large as $\pm 10\text{mm}$.

6.3.2 Force-position history

A typical force-position diagram for a needle insertion and retraction is presented in Figure 6.6. The force-position curve during insertion is jagged, showing a large number of peaks, whereas the retraction curve is relatively smooth. Note that the retraction force is initially positive, due to an elastic component in the tissue displacement.

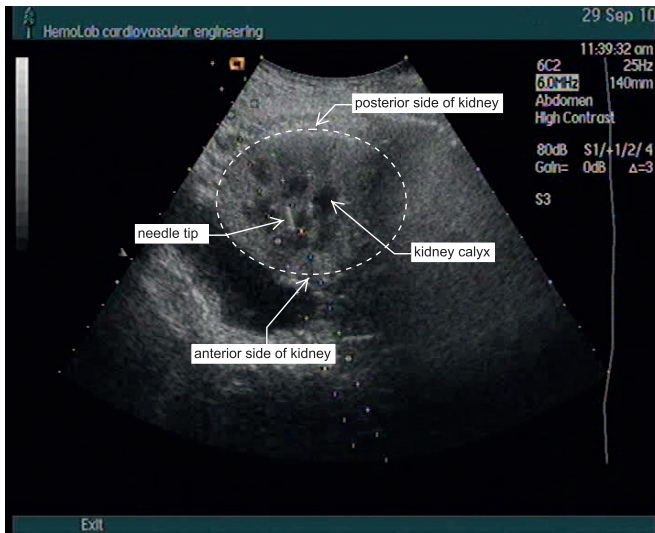


Figure 6.5: Ultrasound still from run 13 showing the approximate location of the needle tip inside the kidney

The boundary between regions 1 and 2 is highlighted in the figure. To the casual observer it would seem that this allows us to relate a force peak to a specific anatomical structure such as the renal capsule. However, the error in the estimated boundary position estimate large enough that it becomes impossible to determine which of the three peaks in the vicinity of the boundary line should be selected. Moreover, it is not clear from the ultrasound images whether the boundary is formed by the renal fascia, the renal capsule, or perhaps both.

It does become clear that the slope of the retraction curve differs between the two regions. Thus for each region a separate linear approximation to the friction force can be constructed. The approximated friction from the retraction phase (mirrored about the horizontal axis) is used as the baseline for analysis of the peaks that occur during the insertion phase, as depicted in the figure.

The approximate position at which the needle was observed inside a calyx is also highlighted. Judging from this specific figure, one would be tempted to classify the two closest peaks as being due to calyx entry and calyx exit, respectively. However, we are again limited by the rather large error in position estimation. Moreover, the remaining runs were not so clear.

Thus, we are limited to evaluating the peak metrics (corrected force and slope) per tissue region, stating that region 1 contains mostly muscle and fascia layers, and region 2 contains mostly kidney tissue. The peak metrics are evaluated after pre-processing.

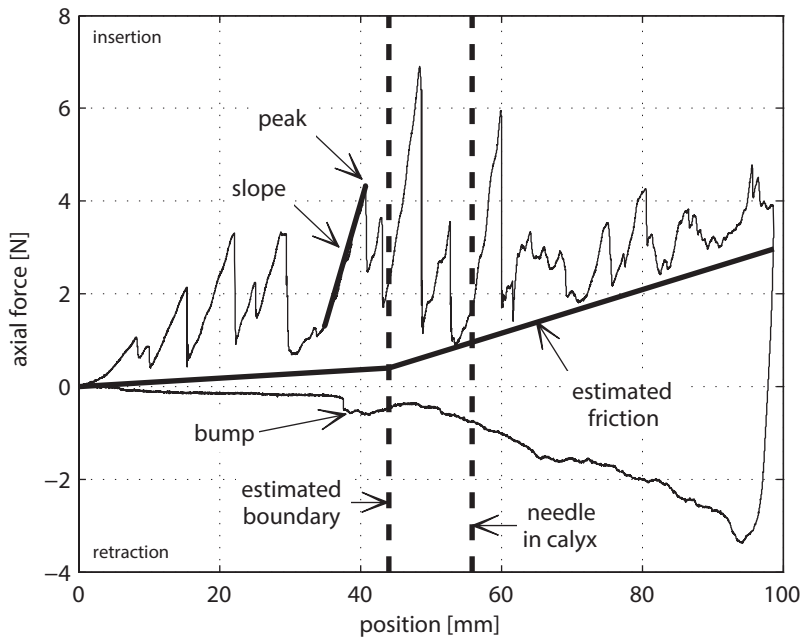


Figure 6.6: Example of force-position diagram (run 4) for insertion and retraction, showing the (filtered) data, estimated location of boundary between tissue regions, and the linear approximations to the total friction for each region. Examples of force peak and secant line are also highlighted, as is the location at which the needle was observed to be in a calyx (from ultrasound footage).

6.3.3 Pre-processing

The process of converting raw data to simplified data is illustrated in Figure 6.7, which shows time histories of force vs position during the insertion phase in run 4. This process inevitably requires some subjective decisions that establish the required level of signal detail. The number of subjective choices made here is limited to two: selection of a filter window size and selection of a simplification threshold. It is even possible to skip the filtering stage if high frequency artefacts are not an issue.

To reduce noise content, a minimal two-pass (zero-phase shift) moving average filter is applied. The term minimal implies that the filter window size for each pass equals two samples. The worst case reduction in peak force due to filtering is much smaller than 0.1%, thus negligible for our purposes. High frequency artefacts, such as visible in the raw signal at position 15mm , are removed successfully.

For line simplification, we assume that the bevel length (2mm) represents an appropriate characteristic length. Thus, the nondimensional bevel length $\varepsilon = \frac{2}{200} = 0.01$ is used as simplification error threshold. The figure shows that this threshold value removes relatively small peaks while preserving the general characteristics of the curve.

The local maxima of the simplified curve and the line segments leading up to these maxima are considered to be relevant peaks. Their characteristics are evaluated next.

6.3.4 Evaluation of metrics

As described in Section 6.2.2, two tissue regions were identified for each run, and a (piecewise) linear friction baseline is estimated based on the retraction force. The friction slopes for each region, representing the increase in friction force per unit contact length between needle and tissue, are presented in Figure 6.8. Clearly, the friction slope in region 2 is consistently much higher than that in region 1.

The number of force peaks (small and large) in each region depends on the tissue structures that are encountered, and may therefore depend on insertion depth (which differs between runs). Moreover, the number of peaks that are actually considered for evaluation depends on the simplification error threshold ($\varepsilon = 0.01$). As a rough indication, the number of peaks in region 1 ranges from 3 to 9 with median 4 ($n = 10$), and that in region 2 ranges from 4 to 11 with median 9 ($n = 10$). Individual peak positions varied widely between runs.

Figure 6.9 presents the corrected peak forces for individual peaks in each run. With the exception of the extreme outlier in run 14 region 2, the difference in distribution between regions 1 and 2 is small, as illustrated by the boxplots for the pooled data. There is no obvious systematic difference between runs.

Figure 6.10 presents the corrected slopes for individual peaks in each run. In this case, the difference in distribution between regions 1 and 2 appears consid-

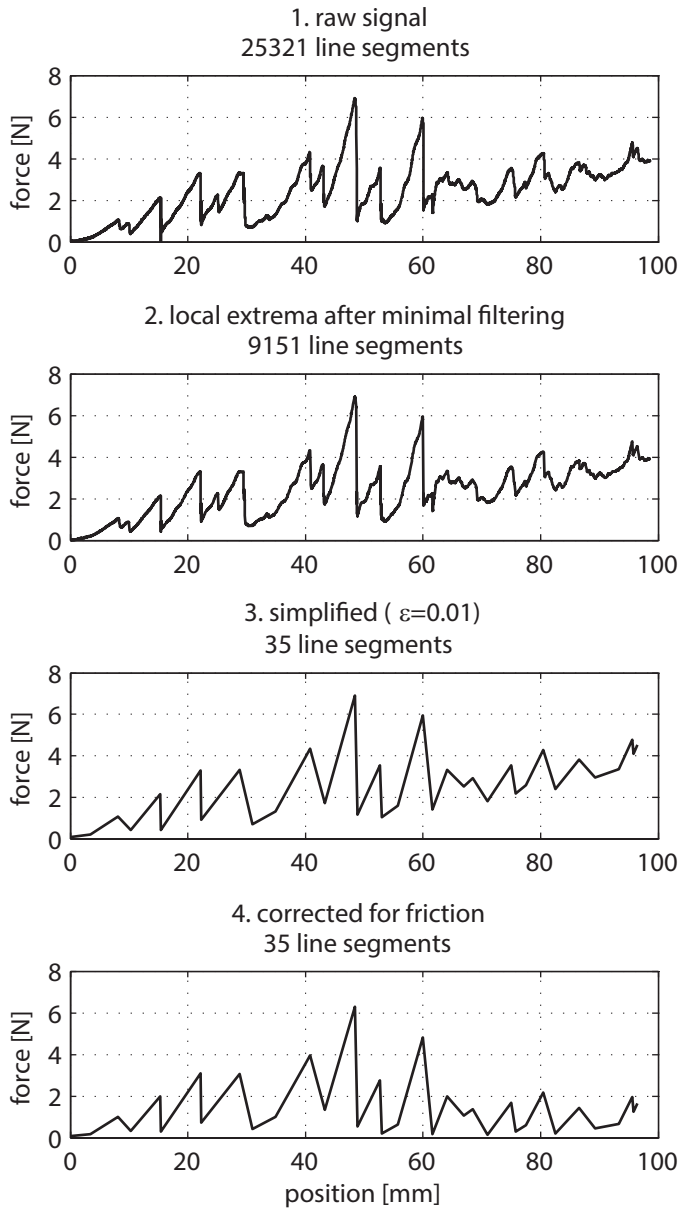


Figure 6.7: Pre-processing stages (run 4): 1. raw data signal; 2. local extrema of minimal-moving-average-filtered signal; 3. simplified signal; 4. friction corrected signal

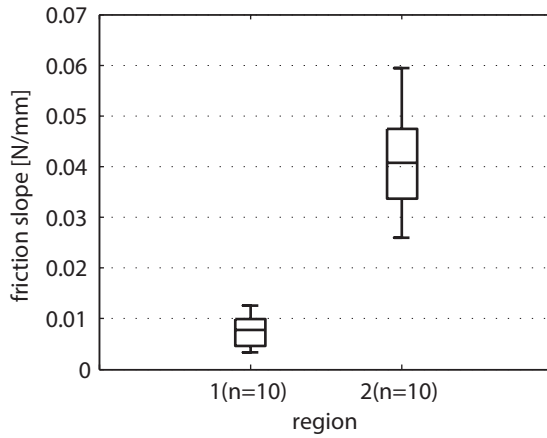


Figure 6.8: Boxplot of the estimated friction slope (i.e. force per unit needle-tissue contact length) in regions 1 and 2, for all 10 runs.

erably larger.

The distributions of the pooled data from Figures 6.9 and 6.10 are summarized here by fitting lognormal distributions. The resulting (dimensionless) parameter estimates, $\hat{\mu}$ and $\hat{\sigma}$, together with the Anderson-Darling statistic A^2 and the corresponding probability p_{A^2} , are presented in Tables 6.2 and 6.3.

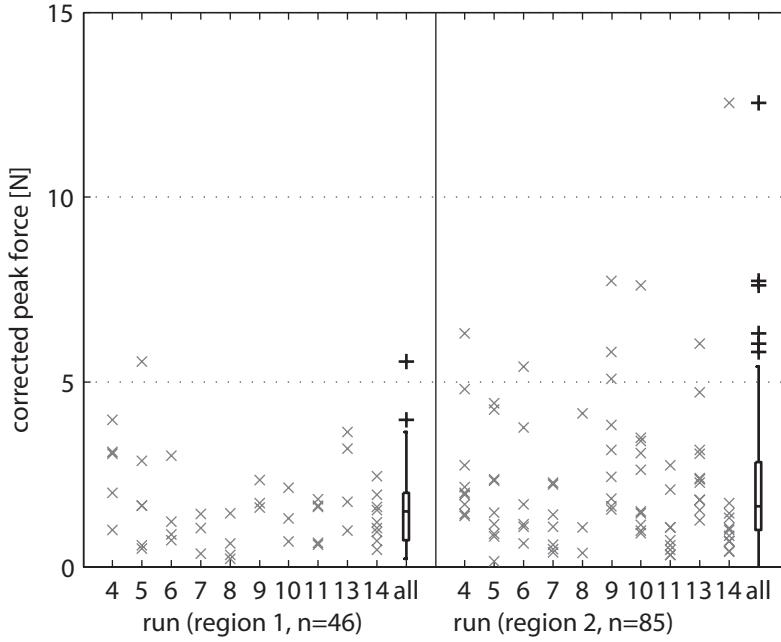


Figure 6.9: Friction-corrected *peak force* values for individual peaks in each run, with boxplots for all runs pooled, grouped by region ($\varepsilon = 0.01$)

Table 6.2: Lognormal parameter estimates for the friction-corrected *peak force* for all peaks pooled ($\varepsilon = 0.01$)

	$\hat{\mu}_p$	$\hat{\sigma}_p$	A^2	p_{A^2}
region 1 (n=46)	0.26	0.71	0.31	0.544
region 2 (n=85)	0.49	0.84	0.16	0.952

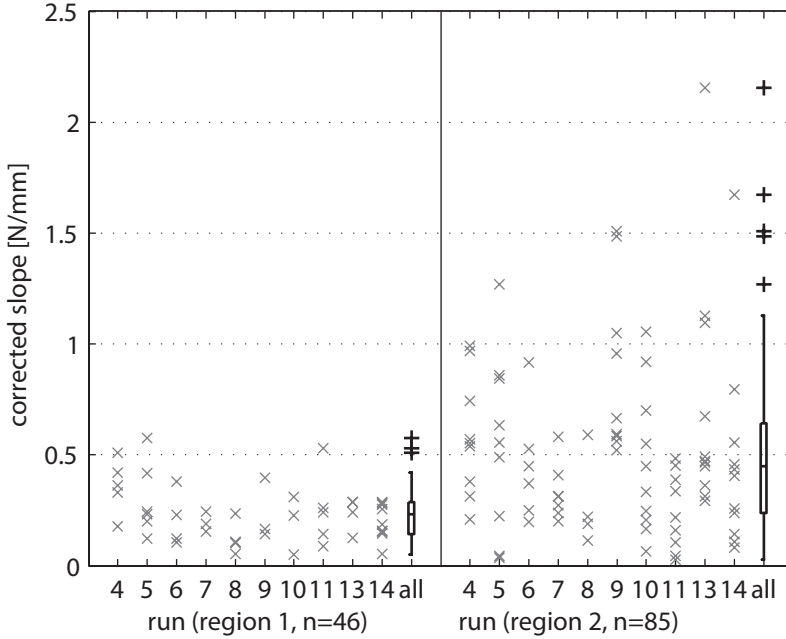


Figure 6.10: Friction-corrected *slope* values for individual peaks in each run, with boxplots for all runs pooled, grouped by region ($\varepsilon = 0.01$)

Table 6.3: Lognormal parameter estimates for the friction-corrected *slope* for all peaks pooled ($\varepsilon = 0.01$)

	$\hat{\mu}_s$	$\hat{\sigma}_s$	A^2	p_{A^2}
region 1 (n=46)	-1.60	0.58	0.43	0.307
region 2 (n=85)	-0.96	0.87	1.11	0.007

Table 6.4: Sensitivity analysis for the lognormal parameter estimates, showing the percentage change in parameter values as a result of a change $\Delta\varepsilon$ around threshold value $\varepsilon = 0.01$ (n is the number of peaks)

	$\Delta\varepsilon/\varepsilon$	Δn	$\Delta\hat{\mu}_p$	$\Delta\hat{\sigma}_p$	$\Delta\hat{\mu}_s$	$\Delta\hat{\sigma}_s$
	%	%	%	%	%	%
region 1	-10	+4	-7	+5	-11	+4
region 2	-10	+6	-2	-0	-11	+1
region 1	+10	-4	+13	-6	+23	-7
region 2	+10	-7	+3	-6	+9	-0

The value of the simplification threshold ε determines the size and number of peaks included in the evaluation. For example, a smaller value of ε will lead to a larger number of small peaks. Thus, the value of ε must influence the pooled distribution and corresponding parameter estimates. To assess the sensitivity of the estimated parameters to changes in ε , the lognormal parameter estimates were obtained for a $\pm 10\%$ variation in ε , i.e. $\frac{\Delta\varepsilon}{\varepsilon} = \pm 10\%$. Results of this sensitivity analysis are presented in Table 6.4,

6.4 Discussion

6.4.1 Interpretation of the results

The goal of this investigation was to obtain a preliminary characterization of the axial forces that arise during needle insertion into a human kidney, in terms of friction, peak force and perceived stiffness, and to attribute observed force peaks to specific tissue structures. To achieve this, we inserted needles, at constant speed, into the right kidney of a human cadaver, while measuring force and position, and capturing ultrasound footage.

Based on ultrasound we distinguished two tissue regions, and characterized forces for each region. The friction slopes in regions 1 and 2 were clearly different, with medians of $0.008N/mm$ and $0.041N/mm$, respectively, and no overlap in range. The difference in slopes is a clear sign that the distinction between the two regions is meaningful. This result shows that the increase in friction, as a function of insertion depth, is typically higher in the kidney than in the related muscle and fascia layers.

We assume that force peaks are due to puncture events (local tissue displacement followed by sudden tissue failure). To isolate the force component acting at the tip (i.e. due to the current puncture event) from the force component due to previously punctured tissue, we corrected the total force by subtracting the estimated friction. This approach is based on the notion that previously punctured tissue layers can only contribute to the total axial force through the mechanism of friction (any elastic contribution is also limited by friction).

To justify our implementation of this friction-correction, we argue that: 1. friction must be present and nonzero (opposed to the direction of motion); 2. the force during retraction must be due to friction alone; 3. both qualitative and quantitative similarity between friction during insertion and that during retraction is to be expected; and 4. as long as the true (unknown) friction force is larger than half the estimated friction force, the residual error after the friction-correction must be smaller than the error in the uncorrected data, so that the correction will yield an improved estimate of peak characteristics.

The number of force peaks observed in regions 1 and 2 differed widely between runs, with median values of 4 and 9, respectively. Based on anatomical considerations (Figure 6.1), three to seven peaks were expected to occur in region 1, and two or more in region 2 (depending on the number of internal kidney structures punctured). The expectation for region 1 is met, to a degree, but that for region 2 is not. Possible explanations for the discrepancy in peak numbers are that multiple membranous tissue layers may be punctured at the same time, and that the shape of the needle tip may give rise to multiple peaks for a single tissue layer. Moreover, the objective peak selection method, based on simplification threshold ϵ , influences the number of peaks by design.

For comparison, purely subjective evaluation based on the original force data (i.e. counting peaks by hand) yields similar numbers of peaks for region 1, but slightly lower numbers for region 2. However, despite the apparent simplicity of this counting task, it proved difficult for the same observer to produce the same count twice in a row, because it is not clear from the force data alone which peaks constitute actual puncture events. Thus, in the absence of clear (absolute) anatomical references, we chose to adopt an objective approach to peak selection, and we chose to equate force peaks to puncture events.

It is noted that the ultrasound footage did provide some anatomical reference, but this was mostly indirect, and was not precise enough to attribute force peaks to specific tissue structures. For this reason, we characterized only groups of peaks, for all runs pooled per region.

Pooling the peaks from all runs is not strictly correct, as there must be some dependence between peaks. However, it is not likely that e.g. puncturing a fascia layer at one point will influence the failure strength of that same layer at another point several diameters away.

Looking at the pooled results, we find that the range for the peak force in region 2 is twice as high as that in region 1, although the medians are approximately equal. The range of slopes in region 2 is three times as high as that in region 1, and the median is almost twice as high. The peak slopes are also at least an order of magnitude larger than the friction slopes. These findings suggest that there may indeed be a considerable difference between puncture events in muscle and fascia and puncture events in the kidney, at least in terms of perceived stiffness. Whether such a difference is noticeable by humans remains to be seen.

The lognormal parameter estimates for the pooled results provide a very concise description of the typical peak characteristics in each region. The lognormal distribution provides an adequate fit to the data, judging from the Anderson-

Darling test results, except for the pooled slopes in region 2 ($p_{A^2} = 0.007$, Table 6.3). Qualitative inspection of the slopes in this region suggests that some of the smallest slope may be due to friction or cutting instead of puncture. To test this, leaving out e.g. the two smallest slopes (making $n = 83$) already improves the fit to $A^2 = 0.59$ with $p_{A^2} = 0.12$.

As expected, the lognormal parameter estimates are sensitive to changes in the simplification threshold (Table 6.4). It is important to keep in mind that the table reflects stepwise changes around the nominal values (for $\varepsilon = 0.01$). The change in $\hat{\mu}_s$, i.e. $\Delta\hat{\mu}_s$, is larger than 10%, whereas most other changes are smaller than 10%. The main point conveyed by this table is that the estimates are not excessively sensitive, percentage changes all being of the same order of magnitude.

6.4.2 Limitations of the study

The experiment was conducted on a human cadaver that had been fixed (with a mild solution) and frozen for a prolonged time. These treatments are known to influence tissue properties, as described by e.g. [147–149]. The question remains to which extent the current results can be extrapolated to live human patients.

The needle was inserted at constant speed using a position-controlled, non-backdrivable linear actuator. This is very different from manual insertion, which may be force-controlled and is subject to different system dynamics. Thus, the current characterization cannot be generalized to the manual insertion case without further research. It should also be noted that manual insertion allows for additional information to be extracted from the force signal. For example, a clinician can use the needle to assess elastic tissue behavior.

Lacking precise methods to classify peaks, we used a naive classification based on a single parameter (the simplification threshold). This inevitably leads to false positives, e.g. slopes that are due to friction or cutting are classified as puncture peaks, single tissue layers may give rise to multiple smaller peaks that are classified as individual puncture events, or peaks from multiple tissue layers may merge into one.

These issues need to be taken into account when interpreting the results.

6.4.3 Conclusion and recommendations

The current investigation was intended to provide a preliminary characterization of the axial forces that arise during needle insertion into a human kidney. These forces were successfully characterized in terms of friction and typical peak forces and slopes in two distinct tissue regions containing muscle/fascia and kidney tissue respectively. However, the data did not allow individual force peaks to be attributed to specific tissue structures, such as renal capsule or calyces.

The resulting dataset may serve as a basis for modeling needle-tissue interaction forces, to be used, for example, in needle-insertion simulators or robots. Several questions remain unanswered and need to be addressed in a more strictly

controlled setting. For example, what are the force characteristics for renal capsule and calyces? To what extent can these measurements (in human cadaver) be generalized to live human tissue?

Acknowledgements

The authors wish to thank Arno Lataster and Andreas Herrler from the Anatomy and Embryology department at Maastricht University for facilitating the experiment and for sharing their general expertise. We thank urologists Ad Hendriks and Irene Tjiam from Catharina Hospital Eindhoven for assisting in the experiments as the clinical expert and for providing the needles, respectively. Last but not least we thank Sjoerd van Tuijl from Hemolab Eindhoven for assisting in the experiment and for providing the ultrasound equipment, and Arjan van Dijke from Delft University of Technology for developing the instrumentation.

Chapter 7

Stochastic modeling of kidney puncture forces

(This chapter is an adaptation of [150], reprinted with permission)

7.1 Introduction

As described in the previous chapter, it is quite a challenge to obtain useful needle-tissue interaction force measurements from organs inside the body. This is particularly true if one aims to relate the measured forces to specific tissue structures. The current chapter presents an attempt to characterize the forces that arise during puncture of isolated porcine kidneys, and to relate these forces to the anatomical structures of the kidney.

7.1.1 Background

Percutaneous nephrostomy (kidney catheterization) is a complex clinical intervention in which a needle has to be inserted precisely into a specific region of the kidney. Like most clinical skills, the ability to perform this difficult procedure can only be acquired by practicing on real patients. This approach puts at risk both patient and clinician.

Simulator training could reduce this risk [108, 151], allowing novices to tackle the first part of the learning curve safely before going into clinical practice. An important training challenge is to familiarize the novice with the forces required to advance the needle, and specifically with the high levels of variability that are typical for real patients. We believe this challenge can be met using a computer-based simulator with force-feedback based on stochastic models of tissue failure strength, i.e. models that take into account random variability.

The current study is aimed at constructing these stochastic models on the basis of forces measured during needle insertion.

7.1.2 Problem description

The problem at hand is that we wish to model the axial forces that arise as the needle travels through the kidney as depicted in Fig. 7.1. These axial forces can be characterized by a variety of metrics, so, to understand which metrics are most useful, we need to consider the clinical procedure.

The goal in percutaneous nephrostomy is to place a catheter inside the renal pelvis so as to drain urine from the kidney. This catheter is placed with the help of a needle which is inserted into one of the calyces. The preferred approach is through the top-end (fornix) of a calyx, as shown in Fig. 7.1, because this reduces the risk of blood vessel puncture [152, 153]. The needle therefore has to puncture the renal capsule and travel through the cortex and through a renal pyramid (medulla). There is also a good chance that the needle will traverse a calyx wall or blood-vessel wall.

The renal capsule consists mostly of connective tissue, and the calyces and pelvis consist of a combination of connective tissue and smooth muscle fibers, making them relatively tough compared with the cortex and medulla [154, 155]. When punctured, these tougher structures tend to produce a tactile “popping” sensation. It is common for clinicians to count the number of these sensations during the procedure, expecting one to occur as the needle passes the capsule and another when the needle enters a calyx [142]. The forces associated with these popping sensations are the ones that need to be characterized here.

Based on observation, the popping sensation is associated with an increase in force as the tissue is loaded, followed by a sudden decrease in force as the tissue fails. Thus we assume that a pop is characterized by a local force peak F , indicative of tissue failure strength, and a corresponding force drop ΔF , indicative of the strength of the popping sensation. The challenge is to model these two metrics for different tissue structures in the kidney, on the basis of force measurements.

7.1.3 Related work

The first step, then, is to search the literature for evaluations of these peak force metrics and force drop metrics. A survey by the authors [12] showed that force data obtained from needle insertions into kidney tissue are scarce:

Maurin et al. [65] inserted 18G trocar needles (type not specified) into porcine kidney in vivo, both manually ($n = 5$) and automatically at 15mm/s ($n = 4$). Healey et al. [52] present a single force-position curve for automated insertion into porcine kidney in vitro at 8.3mm/s (needle type and size not specified). Vidal et al. [108] performed insertions up to 50mm depth into porcine kidney, at 8.3mm/s , using a Chiba needle (size unspecified). In addition, Zhai et al. [156] present data from a single insertion into porcine kidney, at 3mm/s and up to 20mm depth, using an 18G trocar needle.

None of these studies relate detailed force characteristics to specific parts of the kidney, nor do they evaluate the desired metrics. Moreover, the presented

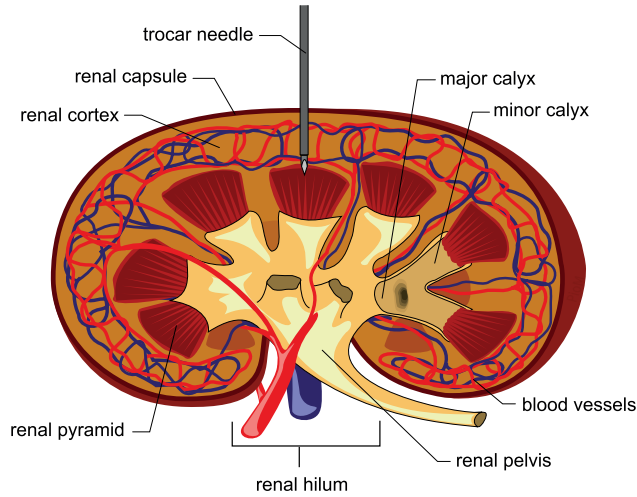


Figure 7.1: Schematic representation of kidney anatomy, showing the needle inserted towards renal pyramid (adaptation of illustration by Piotr Michal Jaworski, Creative Commons license CC BY-SA 3.0)

data are difficult to appraise because methodological details, such as needle type and sample size, and measures of variability are often unavailable.

Even the most strictly controlled needle insertion experiments suffer from a relatively low signal to noise ratio [12]. This implies that the resulting data cannot be properly analyzed without taking into account the (unexplained) variability. This was recognized by Kobayashi et al. [16], who investigated the stochastic behavior of the puncture force metric F for unspecified 17G needles inserted at speeds up to 8mm/s into porcine *liver* (not kidney). A gamma distribution is used to model the puncture force. Their results suggest that the variability of the puncture force decreases with higher insertion speed.

As the required information was not found in literature, a dedicated investigation is justified.

7.1.4 Research objective and approach

The goal of the current investigation is to construct stochastic models of the peak axial force (F) and corresponding force drop (ΔF) resulting from the puncture of kidney capsule, calyx walls and pelvis, using a needle typical for the percutaneous nephrostomy procedure. To simplify implementation we base these models on well known parametric distribution functions, so the problem is reduced to one of parameter estimation. To reach this goal, we inserted trocar needles into porcine kidneys as discussed in detail below.

7.2 Materials and Methods

7.2.1 Measurement protocol and experimental conditions

For practical reasons, isolated porcine kidneys were used in the experiment. Porcine kidneys are slightly larger than human kidneys, but are otherwise very similar in structure and function [157].

Three porcine kidneys were available in total. Each kidney was punctured in five random locations before switching to another kidney in random order. This was repeated up to a total of 60 insertions. All measurements were performed on the same day.

The kidneys were encased in rectangular blocks of gel, placed on a rigid support submerged in water, and were oriented with the renal hilum pointed downwards, as depicted in Fig. 7.1. Needle orientation was fixed at 90° (i.e. vertical), but the insertion angle varied by as much as 30° depending on the kidney curvature at the insertion location. A fixed insertion speed of 10mm/s was deemed appropriate on the basis of literature [12]. The insertion distance was such that the needle passed completely through the kidney. This ensured that the capsule was punctured both proximally and distally during each insertion. Water temperature was maintained at 20°C (room temperature).

7.2.2 Test specimens

The porcine kidneys were obtained from the slaughterhouse the day before the experiment. They were excised immediately after death, and perinephric fat was removed, leaving the kidney capsule intact. The pigs were female Dutch Landrace Hybrids, ages approx. 4-6 months, weight approx. 90-110kg. No distinction was made between left and right kidneys.

Within eight hours after death the kidneys were cast into blocks of high gel-strength Agar (Sigma-Aldrich, Zwijndrecht, the Netherlands), 2% concentration, roughly $20\times 10\times 7\text{cm}$ in size, as depicted in Fig. 7.3. Gel temperature (before casting) did not exceed 45°C . In between actions the specimens were stored at 4°C , and before use the specimens were restored to room temperature (20°C).

7.2.3 Instrumentation

A schematic diagram of the instrumentation is presented in Fig. 7.2. The measurement apparatus, depicted in Fig. 7.3, comprises a linear motion stage, mounted vertically on a frame composed of steel tubing, and equipped with a force/torque sensor and an ultrasound probe. The test specimens are placed directly below the stage and are submerged in water, together with the ultrasound probe, to ensure proper ultrasound transmission. The ultrasound probe is attached to the moving platform (similar to [90]), so that it moves along with the needle during insertion.

An Aerotech PRO115-400 linear stage with 400mm travel and 5mm/rev ball screw was used to move the needle (Aerotech Inc., Pittsburgh, USA). The stage

was equipped with a Maxon EC40 brushless motor and 4-Q-EC servo-amplifier (Maxon Motor AG, Sachseln, Switzerland), and a Scancon 2RMHF-7500 incremental rotary encoder with 7500 pulses per revolution (Scancon A/S, Allerød, Denmark). Positioning-accuracy of the linear stage in combination with this encoder is in the order of 0.01mm .

The needle hub was attached to an ATI nano17 six-axis force/torque sensor (ATI Industrial Automation, Apex, USA), with a 17N rated load and resolution of 0.003N in insertion direction, which was mounted on the moving platform of the linear stage.

Data acquisition and position control of the linear stage were achieved using a dedicated PC (AMD Athlon 64 X2 5200+, 3GB RAM, MS Windows XP Pro SP3) equipped with a dSPACE DS1104 real-time controller board (dSPACE GmbH, Paderborn, Germany). Forces and moments along all axes were stored on the computer, together with time stamp, platform position, and operating state (run, pause, retract). Analog data signals were sampled at 2kHz with 12bit resolution. Data analysis was performed using Matlab R2012b software with Statistics Toolbox (The Mathworks Inc., Natick, USA).

In addition to the force measurements, ultrasound images were captured at 18fps (frames per second) using a dedicated video capture system (Noldus Information Technology, Wageningen, The Netherlands). An audio signal generated on the dSpace board was recorded with the ultrasound images for data synchronization purposes (operating states were characterized by specific audio frequencies).

Ultrasound imagery was provided by an Acuson Sequoia 512 with convex Acuson 6C2 6MHz probe (Siemens AG, Erlangen, Germany). The probe is oriented for an in-plane approach of the needle.

A HASCO Z251/1 digital thermometer (Hasco Hasenclever GmbH, Lüdenscheid, Germany) was used to monitor the temperature of the water containing the test specimen.

7.2.4 Needle characteristics

All measurements were performed with 18G Echotip Trocar Needles of 20cm length (Cook Medical, Bloomington, USA). This type of needle is typical for the nephrostomy procedure [142] and consists of a blunt 1.3mm diameter cannula, with a special grating for increased ultrasound reflection (Echotip), and a 1.0mm diameter stylet with diamond shaped cutting tip. The bevel angle, i.e. the angle between longitudinal axis and grinding plane, is approximately 11° . Microscopic images show that the radius at the very tip is approximately 0.01mm .

The shape of the tip cross-section varies along the length of the tip as depicted in Fig. 7.4 (regions A to D). In a preliminary experiment we used synchronized video to investigate how this tip geometry influences the axial force characteristics during puncture of a thin polyurethane membrane. The result is depicted in Fig. 7.5.

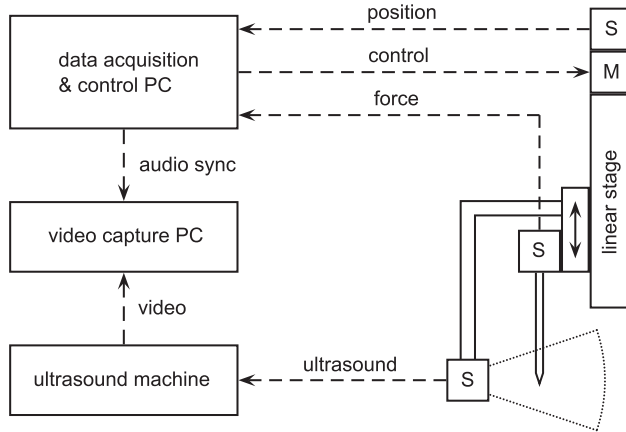


Figure 7.2: Instrumentation diagram showing the ultrasound beam in-plane with the needle (S=sensor, M=motor)

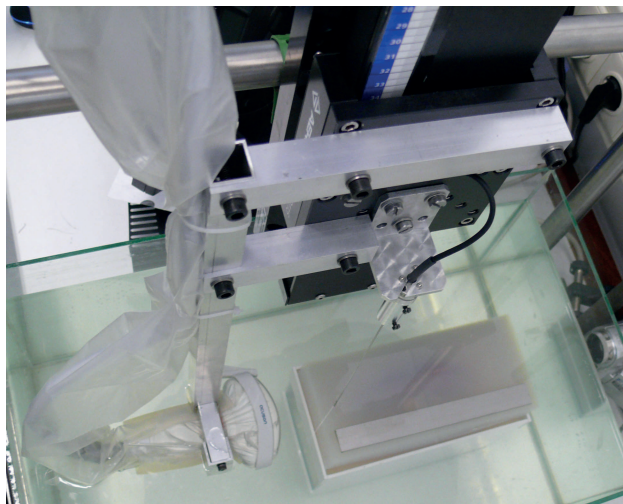


Figure 7.3: Linear motion stage with force sensor, needle, ultrasound probe, and test specimen encased in agar gel and submerged in water. Note that the ultrasound probe is in the out-of-plane configuration in this image, whereas during final measurements it was in the in-plane configuration.

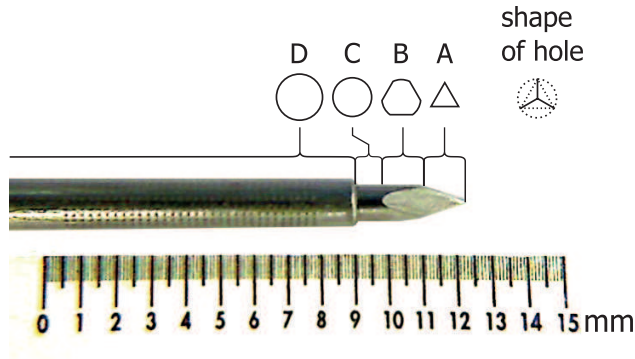


Figure 7.4: Close-up of the 18G Echotip Trocar Needle with grating for increased ultrasound reflection. Regions with different cross-sections are indicated together with the shape of the resulting hole. Diameters: $\varnothing_C = 1.0mm$, $\varnothing_D = 1.35mm$

Three distinct force peaks arise while puncturing this artificial membrane: one at the very tip (start of region A), where the needle starts cutting into the membrane, one near the transition from A to B, where the hole is wedged open, and one at the transition from C to D, where the membrane encounters the edge of the cannula. The second, smaller peak was not always present.

Based on this puncture force characteristic, the trocar needle is expected to produce at least two force peaks for every membranous tissue layer punctured: one due to the tip and one due to the cannula edge. We refer to this as a double-peak. To allow objective identification of these double-peaks, the force signal needs to be pre-processed.

7.2.5 Force signal processing

Objective identification of force peaks is complicated by the noise that is typically present in measurement signals. Therefore the noise in the digitized insertion force signal is reduced using a double-pass moving average filter (zero phase shift). A narrow window (10 points or $5ms$) is used to limit peak attenuation to a maximum of $0.1N$. This choice of threshold value is inevitably subjective. After filtering, the signal still contains local peaks that are irrelevant to the current investigation, so another step is necessary to distinguish between those and the peaks that *are* of interest.

To prepare the signal for objective identification of relevant peak forces, a top-down data reduction algorithm is used, similar to the Douglas-Peucker algorithm [144]. In essence, this algorithm reduces the number of data points used to represent a signal while retaining its most striking features (peaks and valleys). An error threshold value, ϵ , determines the relevant peak size.

The algorithm seeks to approximate the original signal using a subset of its

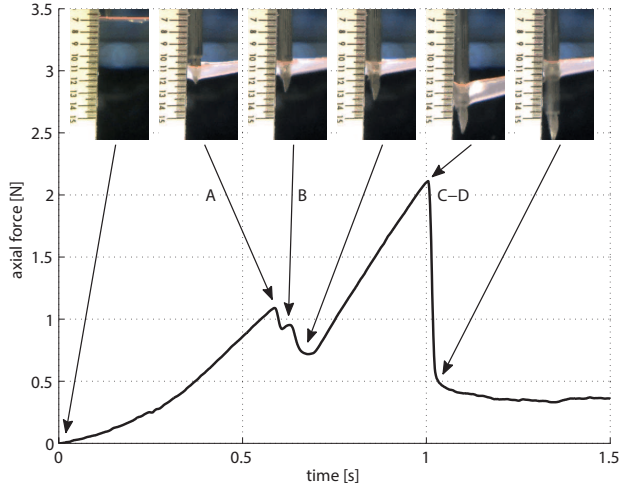


Figure 7.5: Typical force characteristic for the 18G Cook diamond tip trocar needle (puncturing a 0.1mm thick polyethylene membrane under constant uniaxial tension, at an insertion speed of 10mm/s). A-D refer to the regions from Fig.7.4. Similar characteristics for beveled needles are described in the DIN 13097-4 standard.

data points. Initially the entire signal is approximated by one line segment, connecting the first and last point. The algorithm then starts adding data points to this list until a specified approximation accuracy is reached. In each iteration, the data point that has the greatest normal distance to the approximation line is added to the list. In our implementation, the dimensionless normal distance (l^2 -norm) between the line segments and the corresponding data points is used as the error criterion ϵ .

Force and position are normalized with respect to the force sensor rating (17N) and the needle length (200mm), respectively, so that ϵ is dimensionless. We assume that the diameter of the cutting part of the tip (1.0mm) is a useful characteristic length for the level of detail that we are interested in. Thus, we let the error threshold equal the dimensionless tip diameter, i.e. $\epsilon = \frac{1.0}{200} = 0.005$. For this threshold value, the number of points in the signal is typically reduced by three orders of magnitude (from 10^4 to 10) as in Fig. 7.8.

The force peaks that remain after simplification are cross-checked with the ultrasound data.

7.2.6 Ultrasound signal processing

Synchronization of ultrasound data and force data is achieved using the audio signal from the control PC, which was recorded with the ultrasound data. This is done automatically by detecting frequency changes in the audio signal with

the help of fast Fourier transforms. Given the ultrasound frame rate of 18 fps , a synchronization uncertainty of approximately 0.06 s (i.e. 0.6 mm at 10 mm/s) has to be taken into account.

After synchronization, the ultrasound frames corresponding to the vertices of the simplified force signal are extracted for visual inspection.

7.2.7 Peak classification

Membrane puncture events are identified by visual inspection of both the selected ultrasound images and the simplified force-position data. These puncture events are expected to manifest in the force-position data as double-peaks similar to the one depicted in Fig. 7.5. Only distinct double-peaks are taken into account.

Double-peaks occur either when the needle moves into the capsule or some internal structure, or when it moves out of one of those structures. Thus, based on the ultrasound information, each double-peak is classified as one of four groups: (*ci*) capsule in, (*ii*) internal structure in, (*io*) internal structure out, or (*co*) capsule out.

Single force peaks or multiple peaks that are not clearly identifiable, i.e. not distinct and not similar to Fig. 7.5, are not considered in the analysis.

7.2.8 Definition of force metrics

For each double-peak identified, four metrics are evaluated: the tip-peak F_t , tip-drop ΔF_t , cannula-peak F_c , and cannula-drop ΔF_c . These metrics are defined in Fig. 7.6.

The peak forces are defined with respect to an estimated friction baseline, which is represented by vertex 1 in the figure, i.e. the estimated point of initial contact between the needle tip and the membranous tissue layer.

Since F_t occurs first in time, it is treated as independent. The other metrics are then dependent by definition. For example, $F_t = F_2 - F_1$ and $F_c = F_4 - F_1$, so that $F_c = F_t + F_4 - F_2$. As a result, both ΔF_t and F_c have a component that is directly proportional to F_t , and ΔF_c has a component that is directly proportional to F_c .

There are also physical reasons to expect association between the metrics. For example, it is plausible that the quality of the cut made by the tip depends on F_t and that it will influence both F_c and ΔF_c , as well as the remaining friction after puncture (vertex 5). Similarly, tissue toughness is a probable confounding factor, as it can be expected to influence both F_t and F_c , and may also influence the corresponding drops in force.

Sample correlations between metrics are quantified using Spearman's rank correlation r_s , which is more robust than Pearson's coefficient [158].

7.2.9 Stochastic modeling of the force metrics

As stated in the introduction, our goal is to model the observed force metrics in terms of parametric distribution functions. For each tissue class *ci*, *co*, *ii*, and *io*,

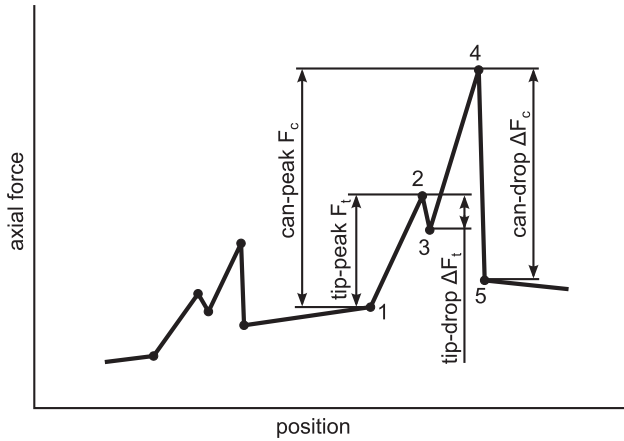


Figure 7.6: Definition of force metrics and vertices 1 to 5

we wish to establish a multivariate model that describes the distribution of the four metrics F_t , ΔF_t , F_c , and ΔF_c .

A convenient approach would be to model each metric as an independent random variable. However, as discussed in the previous section, the metrics are mutually dependent in such a manner that linear correlation can be expected, so that this naive approach is not appropriate. One alternative would be to take the dependence into account for each variable (metric), but this would require assumptions regarding the unknown relations between variables. Another alternative would be to use a multivariate distribution such as a multivariate (log-)normal distribution, but this did not yield satisfactory performance.

Instead we apply a coordinate transformation that reduces the sample correlations to zero, and then model each new variable as an independent random variable (the disparity between correlation and dependence is discussed later). This descriptive modeling process is illustrated in Figure 7.7 and involves three steps.

Step 1 is to determine the orthogonal rotation matrix P (4×4) that transforms the original correlated variables $\mathbf{X} = [F_t \ \Delta F_t \ F_c \ \Delta F_c]^T$ into a new set of uncorrelated variables \mathbf{Y} , where $\mathbf{Y} = P\mathbf{X}$. This is achieved by principal component analysis (PCA) 159. The columns of P are called the principal components (PC1 to PC4), and they consist of the unit eigenvectors of the sample covariance matrix.

Step 2 is to apply the coordinate transformation (rotation) $\mathbf{Y} = P\mathbf{X}$ to the observed data, thereby removing the sample correlations.

Step 3 is to select parametric distribution functions for the transformed data and estimate their parameters. This is done independently for each of the new variables in \mathbf{Y} . For convenience we use either the normal distribution function $\mathcal{N}(\mu, \sigma)$ or the lognormal distribution function $\ln \mathcal{N}(\mu, \sigma)$. If the transformed

observations take negative values, a normal distribution function is used. Otherwise, the choice between normal and lognormal distribution function is based on goodness-of-fit in terms of the Anderson-Darling statistic [145, 146], (a measure of discrepancy between theoretical and empirical distribution functions). Parameters μ and σ are estimated in the maximum likelihood sense.

The final model for each tissue class (ci , co , ii , or io) now consists of a transformation matrix P , and the distribution types and corresponding estimated parameters $\hat{\mu}$ and $\hat{\sigma}$ for each of the four transformed variables.

7.2.10 Simulation of the force metrics

To simulate puncture events using the proposed models, the process is reversed as depicted in Figure 7.7. This involves two steps:

Step 4 is to independently draw sets of (quasi-) random numbers from each of the estimated distributions (either $\ln \mathcal{N}(\hat{\mu}, \hat{\sigma})$ or $\mathcal{N}(\hat{\mu}, \hat{\sigma})$). This yields a simulated dataset in terms of the transformed variables \mathbf{Y} .

Step 5 is to transform this simulated dataset back to the original variables, using the inverse rotation $\mathbf{X} = P^T \mathbf{Y}$. Negative values are discarded, as discussed later.

The proposed models should produce simulated data with probability distributions similar to those of the measured data, and the principal components of the simulated data should, on average, have the same orientation as those of the measured data. These two criteria are evaluated in a Monte-Carlo study using $N = 10^5$ random datasets of size $4 \times n$ for each group. The two-sample Kolmogorov-Smirnov (KS) test [160, 161] is used, for individual metrics in each simulated dataset, to determine the probability that the simulated data and measured data are samples from the same distribution. A conservative significance level of $\alpha = 0.01$ is employed to account for the fact that four metrics are tested. To uncover possible bias in the principal component orientations, we evaluate the mean difference between the first principal component of each simulated dataset and the first principal component of the original dataset.

7.3 Results

7.3.1 Raw data

An example of raw force-position data from a single kidney insertion is presented in Fig. 7.8, together with its simplified representation. The horizontal axis represents the absolute position of the needle base, so tissue displacement is not taken into account. A position of zero corresponds to the point of initial contact with the gel enclosing the specimen. The absolute maximum force encountered during the entire experiment was $12N$.

Fig. 7.8 shows a number of double-peaks that are very similar in shape to the one depicted in Fig. 7.5. The tip-peaks and corresponding can-peaks described in

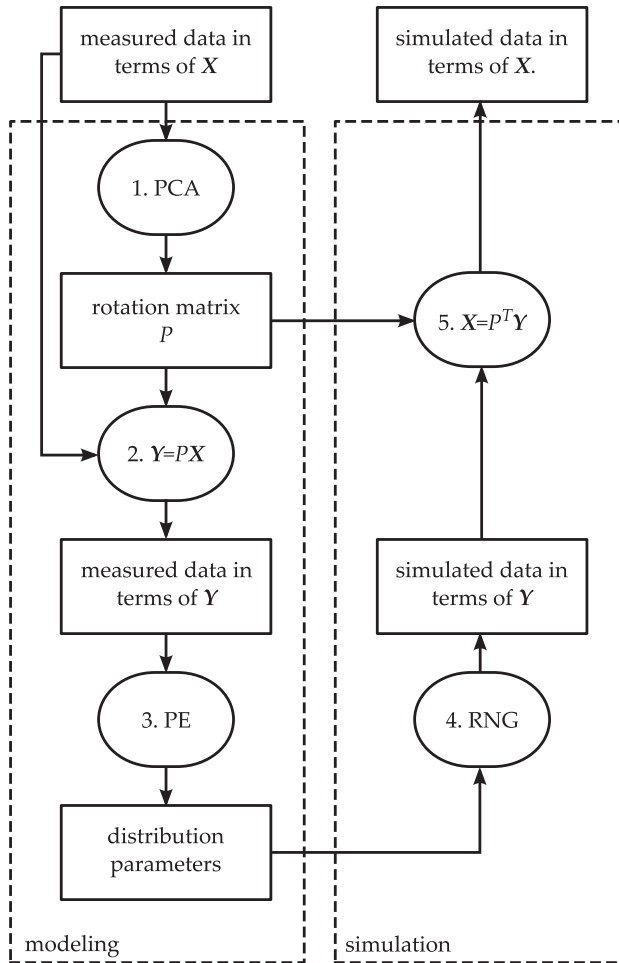


Figure 7.7: Flow diagram of the descriptive modeling process and corresponding simulation process (PCA=principal component analysis, PE=parameter estimation, RNG=random number generation).

the methods section are easily recognized by the human eye, but a set of rules by which to identify and classify these peaks consistently was difficult to establish. To ensure objective and reproducible peak identification, the analysis is based on the simplified representation of the raw data, as depicted in Fig. 7.8. The corresponding ultrasound data are used for verification.

Fig. 7.9 shows the sequence of ultrasound frames corresponding to the markers in Fig. 7.8. The first frame represents the point of contact between needle and kidney, and subsequent frames show the point of maximum displacement for each membranous layer, i.e. the point where the cannula edge pops through (vertex 4 in Fig. 7.6).

In the ultrasound images, the renal capsule is recognized as a thin white (hyper-echoic) line enclosing the cortex. In the center we recognize some dark spots surrounded by white lines that are likely to belong to the collection system. Based on these images, it is clear that some kind of internal structure is pierced, but it is difficult to determine the specific type or part of that structure (e.g. calyx, pelvis, blood vessel). Thus we are limited to a crude distinction between capsule and internal structures.

Judging from the force data in Fig. 7.8, it seems reasonable to state that the needle punctures four distinct membranous structures. The ultrasound images confirm that these puncture events correspond to capsule entry (ci), entry into and exit from some internal structure (ii and io), and capsule exit (co), respectively.

However, this clear-cut example represents only a small minority of the measurements, as illustrated by Fig. 7.10. Only four measurements have double-peaks that can all be uniquely identified as in the example. In eight cases, double-peaks appear only for the capsule, suggesting that no internal structures were encountered. In forty-eight cases, one or at most two double-peaks can be identified, whereas the other peaks are discarded because they cannot be distinguished from each other (without resorting to imagination). The capsule-in group (ci) is easily recognized in most cases, even without ultrasound, and is most reliable, with minimal error in terms of estimated friction baseline (vertex 1). The resulting sample sizes, i.e. the number of double-peaks identified, are $n_{ci} = 55$, $n_{ii} = 10$, $n_{io} = 7$, and $n_{co} = 47$. For each of these groups we evaluate the force metrics.

7.3.2 Force metrics

Figure 7.11 shows scatter plots for all combinations of metrics for the ci and co groups (capsule in/out), with corresponding sample correlations r_s . In both groups, ΔF_t vs F_t and ΔF_c vs F_c show considerable (linear) correlation, whereas the other combinations do not. In both groups, F_c is mostly larger than F_t . Furthermore, ΔF_t is considerably smaller than F_t , whereas ΔF_c is approximately equal to F_c . The co group shows greater variability in general.

Figure 7.12 shows similar scatter plots for the ii and io groups (internal structures in/out). All combinations of variables for ii and io show large sample cor-

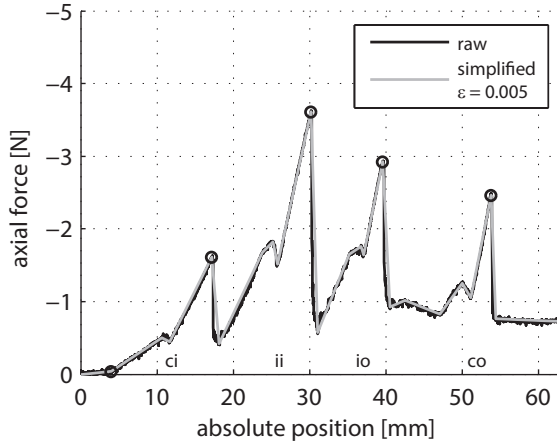


Figure 7.8: Example of raw force-position data and the corresponding simplified representation. Circles correspond to the ultrasound frames in Fig. 7.9. Peaks are classified as *ci* (capsule in), *ii* (internal in), *io* (internal out), *co* (capsule out), based on ultrasound data.

relations, but these correlations are unreliable due to small sample size (width 95%-confidence intervals for r_s ranges from 0.6 to 1.4). As before we see that, for most observations, $F_c > F_t$, $\Delta F_t < F_t$, and $\Delta F_c \approx F_c$.

Comparing the capsule groups (*ci* and *co*) with the internal-structures groups (*ii* and *io*), we find that ΔF_{iip} takes similar values in both capsule and internal structures, but the other metrics reach much higher values in the internal structures (e.g. $F_{c,io} < 8N$ whereas $F_{c,co} < 2N$).

7.3.3 Stochastic models of the force metrics

The principal component matrices (P) and estimated distributions ($\mathcal{N}(\hat{\mu}, \hat{\sigma})$ or $\ln \mathcal{N}(\hat{\mu}, \hat{\sigma})$) for all groups are presented in Tables 7.1 to 7.4. The tables also show the percentage of total variance explained by each of the principal components, which can be used to select reduced models, if necessary. Note that the parameters for normal distributions and lognormal distributions cannot be directly compared, because the latter are dimensionless whereas the former are in Newtons.

7.3.4 Simulation results

The Monte-Carlo performance evaluation ($N = 10^5$) showed that 1.6% of the simulated observations were rejected by the two-sample Kolmogorov-Smirnov test, at a significance level $\alpha = 0.01$, as not being likely to come from the same distribution as the original dataset. Maximum directional bias in the first principal component of the simulated data was found to be $0.002N$. The percentage

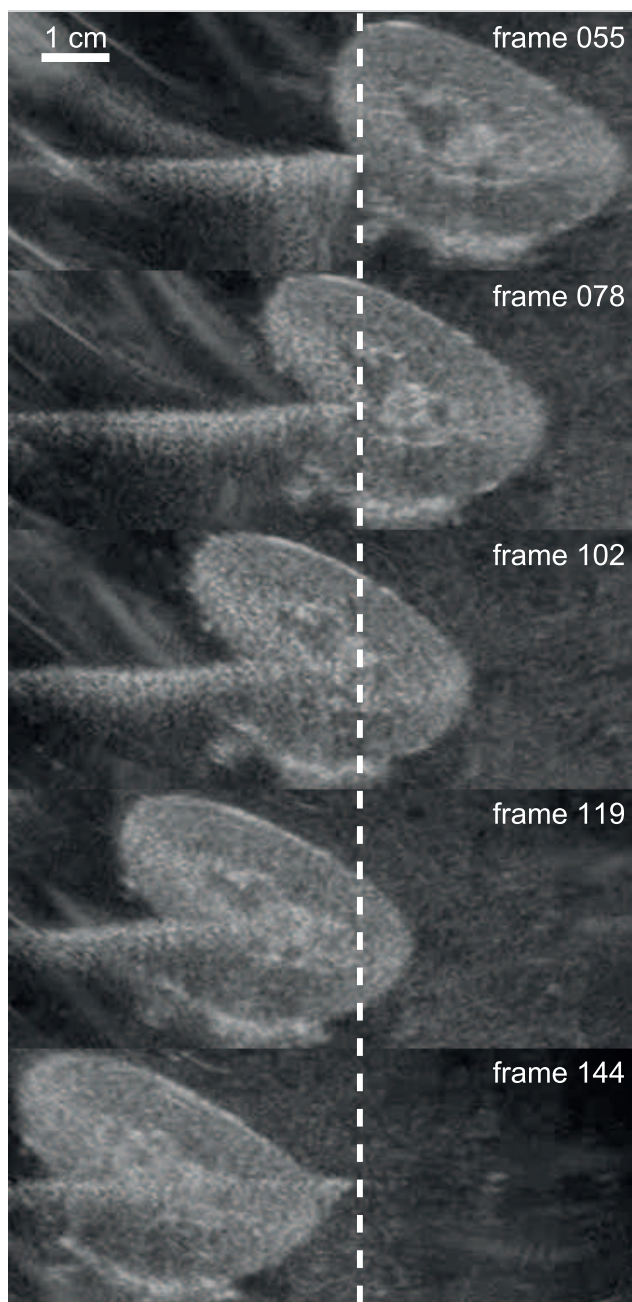


Figure 7.9: Sequence of ultrasound frames corresponding to the positions highlighted in Fig. 7.8. The dashed line represents the location of the needle tip.

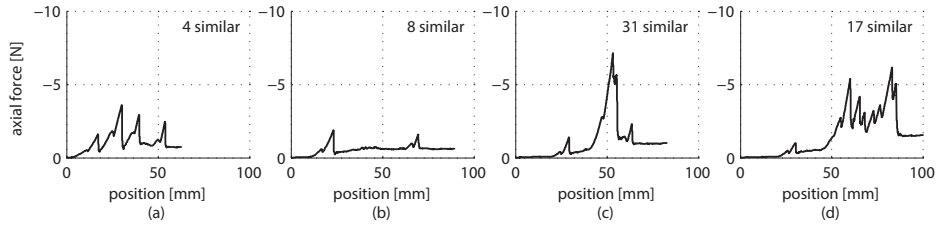


Figure 7.10: Examples of measurements: (a) peaks corresponding to both capsule and internal structures can be identified; (b) capsule peaks can be identified, but no internal peaks found; (c) and (d) some peaks can be identified, but no clear distinction possible between remaining peaks

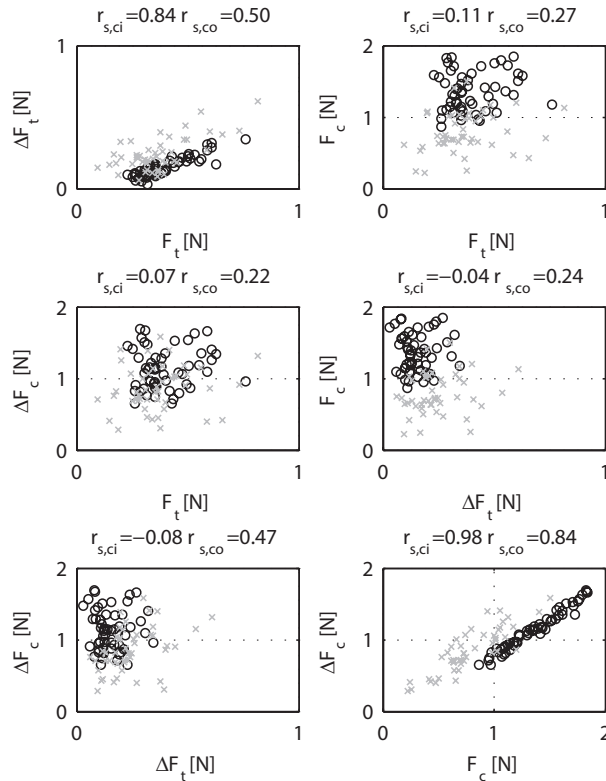


Figure 7.11: Scatter plots showing all possible combinations of metrics for the *ci* group (\circ) and *co* group (\times), with corresponding Spearman rank correlations r_s ($n_{ci} = 55$ and $n_{co} = 47$).

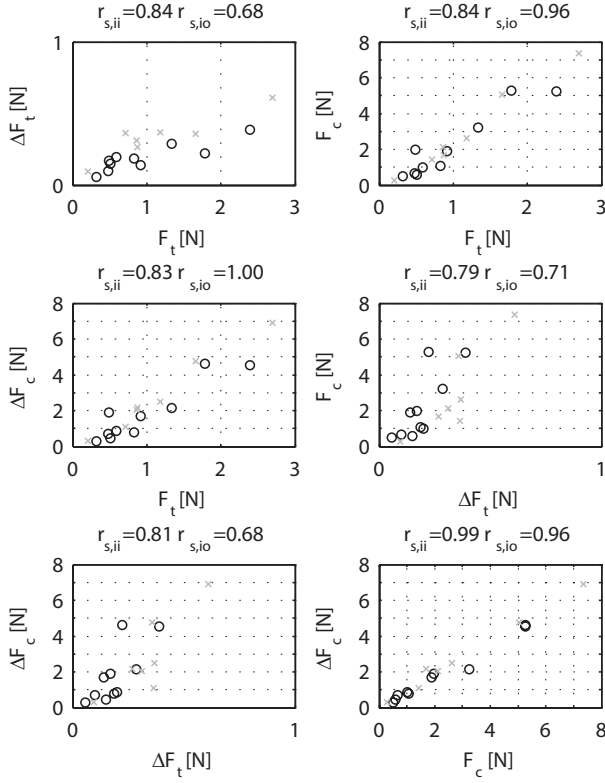


Figure 7.12: Scatter plots showing all possible combinations of metrics for the ii group (\circ) and io group (\times), with corresponding Spearman rank correlations r_s ($n_{ii} = 10$ and $n_{io} = 7$).

Table 7.1: Descriptive model for the ci group

	PC1	PC2	PC3	PC4
variance explained	88.6%	10.2%	0.8%	0.4%
P_{ci}	0.043	0.863	0.119	-0.489
	0.001	0.498	-0.350	0.793
	0.691	0.030	0.668	0.275
	0.722	-0.080	-0.646	-0.236
distribution	$\ln \mathcal{N}$	$\ln \mathcal{N}$	$\ln \mathcal{N}$	\mathcal{N}
$\hat{\mu}_{ci}$	0.552	-1.046	-1.833	0.033
$\hat{\sigma}_{ci}$	0.222	0.343	0.224	0.026

Table 7.2: Descriptive model for the *co* group

	PC1	PC2	PC3	PC4
variance explained	79.1%	12.7%	6.9%	1.3%
P_{co}	0.088	0.817	0.323	-0.470
	0.105	0.557	-0.359	0.741
	0.660	-0.141	0.659	0.332
	0.739	-0.050	-0.576	-0.346
distribution	\mathcal{N}	$\ln \mathcal{N}$	\mathcal{N}	\mathcal{N}
$\hat{\mu}_{co}$	1.211	-1.434	0.059	-0.026
$\hat{\sigma}_{co}$	0.412	0.590	0.122	0.052

Table 7.3: Descriptive model for the *ii* group

	PC1	PC2	PC3	PC4
variance explained	98.6%	1.0%	0.4%	0.0%
P_{ii}	0.255	0.816	-0.496	-0.151
	0.030	0.162	-0.019	0.986
	0.732	0.166	0.660	-0.037
	0.631	-0.529	-0.564	0.058
distribution	$\ln \mathcal{N}$	\mathcal{N}	\mathcal{N}	\mathcal{N}
$\hat{\mu}_{ii}$	0.777	0.214	-0.085	0.068
$\hat{\sigma}_{ii}$	0.845	0.248	0.153	0.042

Table 7.4: Descriptive model for the *io* group

	PC1	PC2	PC3	PC4
variance explained	99.6%	0.3%	0.1%	0.0%
P_{io}	0.233	-0.122	0.821	-0.507
	0.038	-0.207	0.483	0.850
	0.709	-0.635	-0.305	-0.014
	0.664	0.734	0.009	0.143
distribution	$\ln \mathcal{N}$	\mathcal{N}	\mathcal{N}	\mathcal{N}
$\hat{\mu}_{io}$	1.092	0.004	0.258	0.061
$\hat{\sigma}_{io}$	1.021	0.183	0.128	0.028

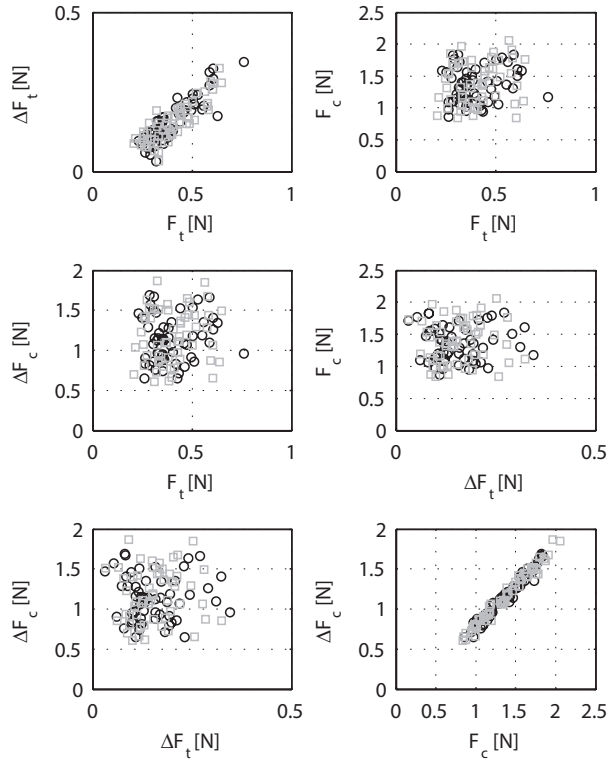


Figure 7.13: Example of a representative simulated dataset (\square) for the *ci* group, together with measured data (\circ). Note that axis scaling varies in order to show the distribution of the observations clearly.

of negative values in the simulations was 0.03% for *ci* (best case) and 0.7% for *ii* (worst case). For illustrative purposes, Fig. 7.13 shows a representative example of a simulated dataset for *ci*, together with the original observations.

7.4 Discussion

7.4.1 Summary of main results

Classification of force peaks proved challenging due to qualitative variability in force response and limited quality of ultrasound footage, and resulted in different group sizes: $n_{ci} = 55$, $n_{co} = 47$, $n_{ii} = 10$, and $n_{io} = 7$ (from a total of 60 insertions). Total axial force observed during the experiments did not exceed 12N. For the capsule groups (*ci* and *co*), $F_t < 1N$, $\Delta F_t < 0.5N$, $F_c < 2N$, and $\Delta F_c < 2N$, whereas for the internal structure groups (*ii* and *io*) $F_t < 3N$, $\Delta F_t < 0.5N$, $F_c <$

$8N$, and $\Delta F_c < 8N$. For all groups it was found that $F_t \lesssim F_c$, $\Delta F_t \lesssim F_t$, and $\Delta F_c \approx F_c$. High sample correlations were observed between ΔF_t and F_t , and between ΔF_c and F_c in the capsule groups.

The multivariate distribution of the metrics was modeled using principal component matrices combined with either normal or lognormal distribution functions. An assessment of correspondence between model and measured data, using Monte-Carlo simulations, showed a 1.6% rejection rate for the two-sample KS-test, and directional bias of $0.002N$ in the first principal component.

7.4.2 Interpretation of main results

The classification of force peaks was almost trivial for the *ci* group, but proved much more challenging for the remaining groups, as illustrated by the differences in group size. Most observations in the internal structures groups (*ii* and *io*) are likely to represent calyx wall punctures, but these observations should be treated with the proper caution.

The difference in magnitude of the force metrics between the capsule and internal structures suggests that the latter are generally harder to penetrate.

The metrics F_t and F_c can be interpreted as measures of tissue failure strength for two different load cases. The fact that $F_t \lesssim F_c$ is in line with expectation, because the area of needle-tissue contact at the tip is much smaller than at the cannula edge, so that the failure stress is reached at a lower axial force.

A higher failure stress (stronger tissue) could be expected to increase both F_t and F_c , thus correlating the two. The high sample correlations for the internal structures groups seem to agree with this expectation, but these correlations were not statistically significant. On the other hand, no obvious correlation was observed in the (more reliable) capsule groups. It is possible that other factors, such as quality of the incision made by the tip, counteract the expected relation.

The association observed between ΔF_t and F_t is in agreement with Section 7.2.8 and also with the nonlinearity of the force-position curve during membrane loading (e.g. Fig. 7.5). After initial membrane failure, represented by F_t , the membrane will unload until it encounters the edge of the cannula. The unloading distance (distance from tip to edge of the cannula) is constant. Due to the nonlinearity of the loading curve, the change in force (ΔF_t) associated with this distance will increase with F_t .

The association between ΔF_c and F_c also agrees with expectation: After final membrane failure, represented by F_c , the membrane will unload until its elastic energy is no longer sufficient to overcome friction. If the friction force is independent of F_c , it is reasonable to expect ΔF_c to be directly proportional to F_c (in the extreme case of zero friction, ΔF_c would be equal to F_c).

The Monte-Carlo performance evaluation of the proposed models suggests that they provide an adequate description of the data. A rejection rate of 1.6% implies reasonable correspondence between the individual distributions of the simulated metrics and the original metrics. The bias of $0.002N$ in the principal component directions is negligibly small. Qualitative assessment of scatter plots

like those in Fig. 7.13 showed good general agreement without obvious discrepancies.

7.4.3 Limitations

The use of an ultrasound probe moving with the needle proved to be very useful in verifying contact with different tissue structures, because the location of the tip in the image is known even if the tip itself is not visible. However, the approach should be refined in order to allow more precise identification of internal structures.

Difficulties in classification caused the sample sizes for the internal structures groups to remain very small. This limits the reliability of the estimated models for ii and io .

Although the choice of threshold value (ϵ) for line simplification ensures reproducibility, it is inherently subjective, and will influence the number of force peaks taken into account in the analysis. However, peak identification inevitably requires such choices.

The use of principal components to remove correlation between variables does not cause them to become independent. However, the scatter plots of the observed data do not suggest obvious hidden dependencies.

The choice of normal and lognormal distribution functions was based on convenience. In contrast, Kobayashi et al. [16] used a gamma distribution to model puncture forces, and in light of failure strength analysis a Weibull distribution might also be suitable [162, 163]. However, these distributions did not provide obvious improvements in goodness of fit in our case.

The proposed modeling approach does not preclude negative values, even though the force metrics are all strictly positive by definition. However, in the worst case, less than 1% of the values in the Monte-Carlo simulations were negative, so the effect of discarding negative values on the distribution shape is deemed negligible.

7.4.4 Conclusion

The goal of this investigation was to construct stochastic models of the peak forces and subsequent drops in force that arise during puncture of tissue structures in the kidney. This goal was achieved using measurement data obtained under ultrasound observation with a moving probe. Reliable classification of peak forces proved a challenge despite the use of ultrasound, especially for internal kidney structures. Nevertheless, a useful dataset was obtained, and multivariate stochastic models were successfully constructed. These models can be used to simulate kidney puncture events in a variety of applications such as training, path planning, and robotics.

Chapter 8

Discussion

...there exists a very human tendency to cease from labor and inwardly rejoice at having thus risen from common fallacious argument to the serene certainty of mathematics. —Charles Spearman, 1904

8.1 A broader scope

The general aim of this thesis was to provide insight into needle-tissue interaction mechanics. To this end we focused on experimental observation rather than (mathematical) theory. The approach adopted was that of indirect observation of interaction mechanics by measuring its results in terms of loads and displacements.

8.1.1 Measuring is essential for a proper understanding

Chapter 1 mentioned several examples of applications involving medical needles. These applications have in common that they all require a clear understanding of the mechanics of needle-tissue interaction. This understanding is typically captured in a theoretical model of some sort.

Clinicians use their internal models of needle-tissue interaction to control the position of the needle tip and to extract information about its anatomical surroundings. Needle insertion robots also need some model of needle-tissue interaction to determine which actions are required to steer the needle to the desired position. For these applications a very simple qualitative model might suffice, but applications like path planning and simulation are likely to require a more detailed description of the relations between loads and displacements. The manufacture of needles, finally, also requires some model that allows one to relate individual design parameters to mechanical behavior in terms of loads and displacements.

The literature contains a variety of theoretical models of needle-tissue interaction, but few of these models have been tested empirically. It is the interaction

between theory and experiment that leads to understanding, and without experimental validation a theory is little more than a belief. Thus, both for the development and for the validation of theory, it is necessary to observe the needle in its natural environment.

8.1.2 Little is known from the literature

To show what others have already learnt by observing needle-tissue interaction, Chapter 2 presented a survey of the literature related specifically to needle-tissue interaction forces. The survey focused on studies that explicitly discussed the axial force, as this is believed to be the most important load. This choice is supported by the fact that hardly any studies were encountered that considered other load components. Most of the studies that measured axial force also measured axial needle displacement, but studies of axial force in combination with tissue displacement were rare. Several studies considered tissue displacement or radial tip displacement without measuring forces, but these were not included in the survey.

Most authors agree that the axial force can be interpreted as a resultant of loads distributed along the shaft, mainly due to friction, and loads concentrated on the tip, mainly due to crack extension (either by gradual cutting or by sudden rupture). The term “puncture” is used often, but is not well defined: Puncture force may refer either to the force at crack initiation or to the overall maximum force, although this distinction is rarely recognized. Friction was found to increase approximately linearly with insertion depth in artificial as well as biological materials.

In addition to these force components, we assert, on the basis of Chapters 4 to 6, that the loads acting on the tip include another component, namely one due to wedging. This component is also found in the industry standard DIN-13097 [3], but to our knowledge has not received explicit attention in the scientific literature. The wedging force is the component of axial force required to enlarge or stretch the hole after the cutting or incision stops. In Chapters 5 to 7 it was found that, depending on needle type, needle coating, and specimen (both artificial and biological), the force component due to wedging can be much higher than that due to cutting. In artificial materials the wedging process may be largely elastic without noteworthy crack extension, but whether this extends to biological tissues is yet to be determined. In addition to the wedging force, we note that needle misalignment or deformation (bending) may also cause normal forces acting on the shaft to contribute to the axial force measured. To our knowledge these notions have not received attention in the literature.

The question of what actually happens at the needle tip pertains to tip geometry, sharpness, and lubrication. These topics have received very little attention in the scientific literature, but it is likely that much more is known in industry. The few sources that are available suggest that specific tip geometries produce specific force characteristics, but very little was found in terms of detailed visual observations. Needle sharpness can be expected to play a major role in the cutting

phase, yet we could not find any investigations specifically aimed at sharpness or wear. The subject has been touched upon indirectly by a few researchers that considered the effects of repeated use of a needle, but actual observations relating reuse effects to reduced sharpness are not provided. Lubrication is another topic that has received only little attention although it can be expected to play a large role. Lack of lubrication was found to increase overall maximum insertion forces, but no studies were found relating these findings to specific force metrics.

Based on the literature, the following general statements can be made, although tentatively: Higher insertion speed leads to higher friction force. Larger diameter leads to both higher friction force and higher maximum force during puncture. Larger bevel angles increase the maximum force during puncture. An increased number of cutting edges reduces the maximum force during puncture. Finally, repeated use and lack of lubrication both tend to increase the total axial force.

These effects all depend on the experimental conditions, so in order to interpret experimental results, details of the experimental conditions need to be reported. It turns out that the available literature rarely provides sufficient methodological detail for the reader to properly assess the results. For example, some 20% of the papers neglected to provide any information regarding needle type or size. Moreover, the results themselves often lack required detail, as illustrated by the fact that 70% of papers neglected to specify measures of variability or sample size. Without this information it is very difficult to synthesize knowledge from the literature.

The literature survey provided some insight into needle tissue interaction mechanics, but most questions remain unanswered. Looking at the bigger picture, the main problem encountered in surveying the available literature is the lack of essential detail in reported data. It is asserted here that, if we are to expand our knowledge of needle-tissue interaction mechanics by observation, it is necessary to standardize the method of storing and sharing measurement data.

8.1.3 Synthesis of knowledge requires structure

To facilitate the storage and exchange of needle-tissue interaction data, Chapter 3 presented the prototype of a database structure that allows storage of detailed experimental methodology together with experimental data. The database approach imposes a much more rigorous structure than the typical publication. This serves several purposes:

1. To provide guidance in the definition phase of an experiment
2. To allow researchers to keep track of their own original experiments
3. To enable storage and exchange of results both from literature and from original experiments
4. To provide the capability of meta-analysis, literally at the push of a button

5. To ensure traceability of individual measurements to researchers, equipment, etc.

These points are especially important in light of the high variability that is typical in biological tissue. The key to dealing with this variability is to exploit the law of large numbers, and requires large amounts of repetitive experimental work.

The database approach has the potential of facilitating the accumulation of large amounts of data by automating the measurement and storage processes. Once a user-interface has been developed that streamlines manual input of data from the literature, the same interface should also allow definition of new original experiments by selecting information from the database, such as equipment, insertion conditions and other factors, and by specification of an experimental design. This definition can then be used to generate an experimental protocol that might also be used to run an automated experiment. If steps in the analysis process are also automated, summary statistics can then be stored directly in the database with reference to the corresponding raw data files.

Automation of (parts of) the data analysis is not only beneficial from a practical point of view, it is also essential for ensuring objectivity of the results, as it requires precise definition of every step of the process. Chapters 4 to 7 of the thesis illustrate approaches to (partial) automation of the data acquisition and analysis processes in different experimental settings.

8.1.4 Direct visual observation is essential for selection of metrics

Arguably the first thing to do when trying to investigate needle-tissue interaction by measuring loads and displacements is to see what actually happens at the tip of the needle. How do loads and displacements relate to the mechanical processes at work at the tip? Surprisingly, no satisfactory answer was found in the literature.

Chapter 4 presents an approach to this problem involving direct visual observation of the membrane puncture process with the help of a high-speed camera. Synchronized video observation enabled the estimation of membrane displacement and corresponding needle insertion depth. This in turn allowed us to relate force characteristics to geometric features of the needle tip.

Based on the literature, Chapter 2 identified three needle insertion phases: boundary displacement, tip insertion and tip and shaft insertion. The observations from Chapter 4 allow us to subdivide the tip insertion phase into an incision phase and a wedging phase, which can be related to three metrics: F_0 , F_1 , and F_2 . These metrics are similar to those for lancet point needles described (very concisely) in the literature.

By inspection of the video footage and by microscopic investigation of the resulting damage to the specimens, it was possible to relate F_0 to the start of the incision phase (possibly involving local yield as well as crack initiation). In the same manner, F_1 was related to the transition from back bevel to primary bevel, which marks the end of the incision phase. Thus, the back bevel was found to

create the incision, and the primary bevel was found to act as a wedge. The metric F_2 was identified as the maximum force during the transition from primary bevel to the shaft, i.e. the maximum wedging force. Wedging in the polyurethane specimen material was found to be largely reversible, as the hole in the specimen closed up neatly after needle removal, showing few signs of plastic deformation and no signs of additional crack extension.

The definition of objective metrics implies that it must be possible to evaluate these metrics using a fixed set of rules. We defined such a set of rules in terms of stationary points of the force signal and its first and second derivatives, and constructed an algorithm that successfully evaluated the described metrics for the current experiment. The same algorithm was found to be applicable to other experiments with the same needle under similar conditions, as in [164]. Identification of F_1 (end of incision) and F_2 (maximum wedging) was relatively straightforward, involving only the identification of local maxima. However, identification of F_0 (start of incision) proved more difficult due to considerable qualitative variation in the force response. Thus, in the absence of visual confirmation, the automatically evaluated F_0 metrics are less reliable.

In this particular experiment, F_0 and F_2 were approximately equal in value and both were considerably smaller than F_1 . All three metrics increased in value as the number of punctures with the same needle increased, which was referred to as the reuse effect. Moreover, the difference between F_0 and F_1 was found to increase with reuse.

The question whether these findings apply to biological tissue as well remains to be answered. A needle inserted into the human body typically encounters a succession of membranes, which would suggest that a reuse effect could occur even within one insertion. It is not known whether such an effect could be large enough to be relevant.

The matter of needle reuse in experiments requires careful attention, as the reuse effect was found to be strong enough, even after 100 punctures, to obscure main effects under study. Follow up studies (e.g. [164]) showed that the strength of the effect decreases with use, so it is more pronounced for a new needle than for a used needle. The reuse effect appears to be cumulative, as the axial force increases with each puncture. Therefore, likely causes for the reuse effect are wear of the cutting edge (decreased “sharpness”), wear of the lubricant, and/or accumulation of specimen material on the needle surface. Because the reuse effect was also observed in the wedging metric, which does not involve cutting, it made sense to investigate the effects of lubricant.

8.1.5 Lubrication influences the force metrics

In Chapter 5 we investigated the influence of needle coating on the force metrics identified in Chapter 4. This was achieved by subjecting back-bevel needles to a cleaning treatment in order to remove their coatings, and comparing them, in terms of membrane puncture forces, to a control group of unmodified needles.

The idea was that, if coating wear plays a role in the reuse effect, complete removal of the coating should cause a reduction in strength of the reuse effect.

The experiment showed that the cleaning treatment has a very large effect on the wedging force F_2 , and that it has small effects on F_0 and F_1 , which are related to cutting. This in itself suggests that, if the coating would actually wear off between punctures, the result would indeed be an increase in all force metrics. However, the experiment also showed that the reuse effect was still present in both groups of needles for F_0 and F_1 , and no obvious difference in strength was observed between groups. The small effect of reuse observed for F_2 was not statistically significant, but a small effect is easily obscured by the large variability in the cleaned group.

Considering the general effect of needle coating on the metrics for the back-bevel needle, it is safe to say that the most important effect of coating is to dramatically reduce the wedging force. For the coated needles F_1 is the largest peak, but for the cleaned needles F_2 is much larger than F_1 .

It remains to be seen whether these findings apply to biological tissue as well. It is conceivable that the effect would not be as large that observed here, e.g. due to a possible lubricating effect of fluids that are released as the tissue is damaged, but this is just speculation.

The available equipment did not allow verification that the cleaning treatment actually removed all of the coating: Optical microscopy did not show noticeable differences in needle (or coating) surface quality. Nevertheless, based on the observed differences in force, it is safe to assume that the coating quality has at least been altered.

The algorithm from Chapter 4, for evaluation of the force metrics, worked reasonably well, although the results for F_0 are again less reliable. This shows that even in relatively tightly controlled experiments with known boundary conditions and uniform specimen quality, it is a challenge to obtain high quality data. This challenge becomes much greater when dealing with biological tissue, especially when it is located deep inside the body.

8.1.6 Kidneys in human cadavers

Experiments dealing with artificial specimens, such as those described above, are useful for the study of fundamental questions involving factors related to the needle and for optimizing the experimental set-up and protocol. In that context, variability due to the specimen is considered noise. The use of artificial specimens minimizes noise, as the specimens are typically homogeneous, isotropic, and uniform in quality, at least much more so than biological tissue specimens, and their properties are relatively time invariant. Moreover, with artificial specimens it is known in advance which kinds of structures will be penetrated and where they are located, and visualization can be achieved with relatively simple means. Thus, it is not too difficult to relate forces to structures of an artificial specimen.

However, medical needles are intended for use on live biological specimens, also known as patients, which have entirely different properties and exhibit much greater intrinsic variability. The effects that arise in experiments with artificial tissue, such as those described above, might not be present with biological tissue, or they might turn out differently. Variability due to biological specimens tends to obscure these effects and can therefore be considered a nuisance in this type of experiment. On the other hand, when the aim of an experiment is to describe or model the interaction between needle and specific types of biological tissue, the intrinsic variability of the tissue becomes important in itself.

Chapter 6 presented an attempt at characterizing the forces that arise when a needle is inserted into the kidney of a human cadaver. The aim of this experiment was to describe the forces that arise when puncturing specific anatomical structures in the body. The logical approach was to consider anatomical theory, in this case an image from a textbook, and then try to relate observed force peaks to the tissue structures that should theoretically be encountered. Ultrasound visualization was used to aid in the identification of these tissue structures. This, however, was not so easy as it seemed.

The results did not show justifiable correspondence between observed force peaks and expected tissue structures. The use of ultrasound did not help much in this respect, because of difficulties in discerning individual tissue structures and difficulties in maintaining a clear view of the needle during insertion. Although needle presence in kidney calyces was confirmed by ultrasound on several occasions, we were not able to relate calyx-puncture events to individual force peaks with reasonable certainty due to the close proximity of adjacent force peaks and the relatively large position estimation error.

Nevertheless, it was possible to identify two general tissue regions based on the ultrasound data, containing either mostly muscle or mostly kidney. The properties of the forces observed in each region were then characterized in terms of friction slope, puncture force slopes, and puncture force peaks. Although the needle was reused multiple times, no obvious trend was observed in the peak forces. The friction slope in the kidney region was found to be higher than that in the muscle region. Despite the fact that the characterization per region is very crude, it does provide a useful impression of the general variability of puncture forces in this type of procedure.

The matter of selection of peaks to include in the characterization presented a serious challenge. The type of approach adopted in Chapter 4 is not applicable here because we are no longer dealing with isolated puncture events and variability is too great. The typical approach then would be manual selection, but, in addition to being time consuming, this approach is subjective and it proved to be difficult to reproduce. For this reason a line simplification algorithm was employed that removed irrelevant detail from the time series on the basis of a single threshold value. This line simplification approach is still subjective on two accounts, namely the choice of algorithm and the choice of threshold value, but some choices inevitably have to be made. The fact that it is a naive method implies that some loss of relevant detail or misclassification are inevitable, however,

the same is true for manual classification in the absence of an absolute standard. Moreover, the line simplification algorithm allows automation and thus provides reproducible results.

This explorative study provided a ballpark estimate of the magnitude and variability of forces that may be encountered in human cadavers. Such information was not available before. However, it remains to be seen whether these findings are also representative of live human tissue. Moreover, the study did not provide detailed insight into the needle-tissue interaction process itself, nor did it allow detailed classification of forces. In order to relate force characteristics to individual tissue structures a more strictly controlled environment is needed.

8.1.7 Isolated porcine kidneys

In order to simulate puncture events inside the kidney, it is necessary to determine when specific anatomical structures of the kidney tend to fail, that is, we need to know at which axial force the needle will penetrate these tissue structures. The multitude of factors involved in mechanical failure of tissue implies that failure will not occur at the same force level each time, but rather that the force level will vary between punctures. The question, then, is how to describe the distribution of forces at which tissue failure occurs. This question was addressed in Chapter 7.

Chapter 7 describes an experiment in which isolated porcine kidneys were punctured using a trocar needle under ultrasound visualization. The challenge in this experiment was to identify individual force peaks and evaluate corresponding metrics, and then to relate these force peaks to specific tissue structures based on ultrasound information. To ensure that the tip position in the ultrasound image was known at all times, the ultrasound probe was moved along with the needle (fixed relative position). This approach had not been adopted before in the literature.

The resulting ultrasound footage was easier to analyze than that described in the cadaver study from Chapter 6. Forces due to puncture of the kidney capsule were readily identified and classified. Inside the kidney, however, it was still often difficult to distinguish between individual puncture events. Moreover, it proved difficult to unequivocally identify specific anatomical structures such as calyces and pelvis. Thus, classification was still limited to a very general distinction between capsule and “internal structures.”

The forces that were observed during puncture of these kidney structures, i.e. capsule and internal structures, were qualitatively similar to those observed during penetration of thin polyethylene membranes: The puncture process was characterized by a double-peak, i.e. a small peak corresponding to penetration of the needle point, followed by a larger peak corresponding to penetration of the blunt cannula. Similar characteristics were also found in Chapter 4 for a bevel-tip needle puncturing polyurethane membranes. In Chapter 6, on the other hand, the trocar needle was found to produce both single peaks and double peaks when inserted into a human cadaver.

To summarize the puncture force characteristics for each of the kidney structures we considered four metrics, namely the relative peak forces related to tip and cannula, and the corresponding drops in force. The cannula peak was found to be consistently higher than the tip peak, and can be attributed to wedging effects as described in Chapter 4. The single peaks observed in Chapter 6 are then most likely due to cannula wedging, which would imply that the insertion of the first 3mm of the trocar needle (up to the cannula edge) often goes unnoticed in the cadaver puncture experiment. A possible explanation for the relatively small number of distinct tip-peaks in the cadaver study from Chapter 6 is that the tissue enclosing the cannula might act as a mechanical filter, because it effectively attaches (through friction) a mass-spring-damper system to the cannula.

The choice of metrics for this study was based on the intended application in a training simulator, and on the assumption that these metrics dominate the clinician's perception of puncture events. Whether this assumption is valid depends on psychophysical factors that have not received attention in the current thesis, despite their importance. It is likely that stiffness metrics also play an important role in the clinician's perception of puncture events, but these metrics could not be adequately evaluated using the current methods.

In general, the approach adopted in Chapter 7 provides more reliable data than that in Chapter 6, but the methodology still needs to be improved considerably in order to be able to distinguish specific tissue structures. Direct comparison of the estimated parameters for human cadaver kidneys from Chapter 6 and for isolated porcine kidneys from Chapter 7 is not possible because the former presents a pooled set of peak forces without distinguishing between the tissue structures or the tip and cannula peaks. Nevertheless, we find that the peak forces from the cadaver study which were attributed to the kidney region range up to 13N with a median of approximately 2N. These peaks are most likely due to the cannula edge, and the cannula peaks in the isolated porcine kidneys have a comparable distribution, although sample median and range are lower. At least the values are in the same order of magnitude.

The added value of ultrasound in the present case is disputable, because the analysis requires a substantial effort but does not provide the ability to identify specific internal tissue structures, as was initially intended. As long as the first and last puncture events are distinct, the identification of the capsule would also be possible without ultrasound. Nevertheless, without ultrasound, it would not have been possible to unequivocally distinguish the internal puncture events.

8.2 General limitations of the work

Ideally the type of data presented in this thesis would be obtained from live human patients, but the ethical implications of such an approach are prohibitive. The question directly rises what level of fidelity is actually necessary to achieve our goals, and whether the possible gain of real patient data would outweigh ethical objections. The answer depends strongly on the intended application and

a general answer cannot be given here, but we believe that, before measurements on live patients should even be attempted, the experimental methodology should be optimized as much as possible with the help of alternative specimens.

The experiments presented in the thesis involved artificial membranes, human cadavers, and isolated porcine kidney specimens. As such, none of the findings can be directly extrapolated to the clinical setting, but the findings represent pieces of a larger chain of evidence that might, in the future, allow translation of findings from artificial specimens to the clinical practice. In any case, knowing just a little is preferable to knowing nothing at all.

Although Chapters 4 and 5 presented small samples, the methods used are equally suitable for dealing with much larger samples, e.g. in the order of 1000. The main cost would be time. The methods presented in Chapters 6 and 7 are less suited to large samples, due to limited specimen availability, experimentation time and cost, but also due to analysis effort. The latter issues, in addition to possible ethical objections, become even more limiting when dealing with live animals or humans.

The present thesis focused only on the axial force component. It is likely that interesting information can also be obtained from transverse forces and moments, although this subject was not encountered in the literature. In addition, a more specific investigation of tissue displacement measurement techniques could be of great value.

The present work considered only fixed speed insertion, and the dynamics of needle insertion were neglected in the process. This too implies that the results presented here cannot be translated to the clinical setting directly. To illustrate this point, it is likely that specific control strategies like those employed by clinicians provide much more useful information regarding the needle-tissue interaction process.

The experiments presented in this thesis cover only a very small part of what may be called the experimental design space. For example, we did not consider the influence of speed, needle diameter, etc. This is an inevitable if we want to limit the complexity of the experimental design. The same holds for the choice of metrics or outcome variables.

It should be noted that the experiments presented in Chapters 4 to 7 are not in chronological order. The latter two were performed first, which explains why the insights and recommendations from Chapters 4 and 5, e.g. regarding needle reuse and experimental design, were not implemented in Chapters 6 and 7. Although the possible influence of reuse was recognized beforehand, its potential was underestimated, which is partly due to the lack of attention for the subject in the literature.

The thesis did not cover detailed theoretical models of needle-tissue interaction. Nevertheless, these models play a vital role in the investigation of needle-tissue interaction mechanics, as it is the interaction between experiment and theory that leads to understanding. The choice to focus almost exclusively on the experimental approach was prompted by the general lack of reliable data in the literature, whereas theoretical models are well covered.

8.3 Conclusion

8.3.1 Accomplishments

This thesis showed that, despite great efforts that have been invested in the development of needles and needle-tissue interaction models in past decades, little is known from actual observation of the needle-tissue interaction process and the factors influencing this process.

It was asserted that, to improve upon this situation, a structured approach is required, not only to the collection of experimental data, but also to storage and dissemination of this data. A data model for needle-tissue interaction experiments was presented that facilitates such an approach. This data model is regarded as the essential framework for automating and streamlining the process from setting up and experiment to gathering data, analyzing data, and storing the results. A high degree of automation of all steps in this process is considered essential for ensuring that data are objective and reproducible.

This automation-oriented approach was adopted in the study of membrane puncture. Membrane puncture force characteristics were related to needle tip geometry by video observation of the puncture process. This allowed the establishment of characteristic force metrics related to incision and wedging, together with an algorithm for their evaluation, for one specific combination of needle and specimen type. The establishment of force metrics based on video observation rather than speculation is considered an essential first step in any experimental investigation of needle-tissue interaction force. It is shown that uniaxial tension in the specimen gives rise to very slight anisotropic effects. In addition, the effect of needle reuse is strong enough to obscure other effects and may impede the successful evaluation of force metrics. It is asserted that, in addition to cutting and friction components, the force component due to wedging at the tip needs to be taken into account explicitly in needle tissue-interaction models.

In addition to that of tip geometry, the influence of needle coating on membrane puncture force was investigated. The effect of needle reuse was found to be present regardless of needle coating. The coating was found to cause a strong decrease in the force metrics related to wedging, but had much less profound influence on the incision force metrics.

The explorative investigation of needle insertion into the kidney of a human cadaver provided a first impression of the variability encountered in this type of biological tissue. This information was not yet available in the literature. The degree of experimental control and automation attainable in this type of setting was found to be very low, and objective assessment of the results difficult. The use of a line simplification filter was found to enable objective and reproducible peak identification. On the other hand, peak classification (attaching names to individual peaks) proved very difficult despite the use of ultrasound visualization.

The use of ultrasound to enable classification of force peaks was investigated further in isolated porcine kidneys. The puncture force characteristic for kidney

structures was shown to be similar to that for thin polyethylene membranes. An ultrasound probe moving along with the needle provided knowledge of needle tip position in relation to surrounding kidney tissue and allowed unambiguous classification of peaks into two groups related to capsule and internal structures. The approximate distribution of specific force metrics was described for each of these groups, providing a basis for the simulation of puncture events based on tissue failure strength.

8.3.2 Recommendations

Based on the work presented here, the following recommendations are made:

- Automate as much of the experimental process as possible: This enforces rigorous structure and precision in the approach, and it enables one to harness the strength of numbers.
- If needle reuse cannot be avoided, take its effects into account in the experimental design and analysis.
- Ensure that the level of detail in a report of experimental needle-tissue interaction data is sufficient to enable proper appraisal of the data, e.g. by using the data model from Chapter 3 as a guideline.

Some interesting directions for future work are:

- Incorporation of the data model from Chapter 3 in a software suite for semi-automated data collection.
- Construction of an open access web database based on this data model
- Investigation of a variety of needle tip types with the help of high speed video.
- Investigation of the influence of sharpness on the reuse effect by standardized methods of blunting.
- A more detailed investigation of the crack initiation phase and corresponding metrics.
- Investigation of membrane puncture metrics in isolated biological tissue membranes.
- Follow up the experiment from Chapter 7 using perfused organs and with the ultrasound probe in an out-of-plane approach.
- Psychophysical investigation of force metrics to determine which are actually important for inclusion in haptic simulations.

8.3.3 Final comment

The purpose of this thesis was to provide insight into the needle-tissue interaction process, and some specific insights were indeed gained by experimental observation of the interaction forces. However, the most important contribution consists of a set of tools for gathering, analyzing, and disseminating experimental needle-tissue interaction data.

Bibliography

- [1] Theodore R Kucklick. *The Medical Device R&D Handbook*. CRC Press, Boca Raton, 2006.
- [2] ISO-9626. Stainless steel needle tubing for manufacture of medical devices. Technical Report ISO 9626:1991(E), International Organization for Standardization, 1991.
- [3] DIN-13097. Hypodermic needles – point geometry, requirements and testing. Technical Report DIN 13097:2002-09, DIN Deutsches Institut für Normung, 2002.
- [4] ISO-7864. Sterile hypodermic needles for single use. Technical Report ISO 7864:1993(E), International Organization for Standardization, 1993.
- [5] ISO-11608-2. Needle-based injection systems for medical use - requirements and test methods - part 2: Needles. Technical Report ISO 11608-2:2012(E), International Organization for Standardization, 2012.
- [6] Niki Abolhassani, Rajni Patel, and Mehrdad Moallem. Needle insertion into soft tissue: A survey. *Med Eng Phys*, 29:413–431, 2007.
- [7] Noah J. Cowan, Ken Goldberg, Gregory S. Chirikjian, Gabor Fichtinger, Ron Alterovitz, Kyle B. Reed, Vinutha Kallem, Wooram Park, Sarthak Misra, and Allison M. Okamura. Robotic needle steering: Design, modeling, planning, and image guidance. In Jacob Rosen, Blake Hannaford, and Richard M. Satava, editors, *Surgical Robotics: Systems Applications and Visions*, volume 3, pages 557–582. Springer, 2011.
- [8] Nick J P van de Berg, Dennis J van Gerwen, and John J van den Dobbelen. Approaches in needle steering. *Int J Robot Res*, submitted, 2013.
- [9] Sarthak Misra, K. T. Ramesh, and Allison M. Okamura. Modeling of tool-tissue interactions for computer-based surgical simulation - a literature review. *Presence - Teleoperators and Virtual Environments*, 17(5):463–491, 2008.
- [10] Dedong Gao, Yong Lei, and Haojun Zheng. Needle steering for robot-assisted insertion into soft tissue: A survey. *Chin. J. Mech. Eng.*, 25(4):629–638, 2012.

- [11] Peter Kosso. *A Summary of Scientific Method*. Springer, Dordrecht, 2011.
- [12] Dennis J van Gerwen, Jenny Dankelman, and John J van den Dobbelsteen. Needle-tissue interaction forces - a survey of experimental data. *Med Eng Phys*, 34(6):665–680, 2012.
- [13] A.L. Trejos, R.V. Patel, and M.D. Naish. Force sensing and its application in minimally invasive surgery and therapy: a survey. *P I Mech Eng C-J Mec*, 224:1435–1454, 2010.
- [14] T.B. Frick, D.D. Marucci, J.A. Cartmill, C.J. Martin, and W.R. Walsh. Resistance forces acting on suture needles. *J Biomech*, 34:1335–1340, 2001.
- [15] Winnie Jensen, Ken Yoshida, and Ulrich G. Hofmann. In vivo implant mechanics of single-shaft microelectrodes in peripheral nervous tissue. In *IEEE EMBS Conference on Neural Engineering*, pages 1–4, Kohala Coast, Hawaii, 2007.
- [16] Yo Kobayashi, Akinori Onishi, Takeharu Hoshi, and Kazuya Kawamura. Modeling of conditions where a puncture occurs during needle insertion considering probability distribution. In *IEEE/RSJ International Conference on Intelligent Robots and Systems*, pages 1433–1440, Nice, France, 2008.
- [17] Mohsen Mahvash and Pierre E. Dupont. Mechanics of dynamic needle insertion into a biological material. *IEEE Trans Biomed Eng*, 57(4):934–943, 2010.
- [18] Allison M. Okamura, Christina Simone, and Mark D. O’Leary. Force modeling for needle insertion into soft tissue. *IEEE Trans Biomed Eng*, 51(10):1707–1716, 2004.
- [19] Carlo C. Passerotti, Nikolai Begg, Frank J. Penna, Ana Maria A.M.S. Passerotti, Katia R.M. Leite, Alberto Azoubel Antunes, Miguel Srougi, Alan B. Retik, and Hiep T. Nguyen. Safety profile of trocar and insufflation needle access systems in laparoscopic surgery. *J Am Coll Surgeons*, 209(2):222–232, 2009.
- [20] Tarun Podder, Douglas Clark, Jason Sherman, Dave Fuller, Edward Messing, Deborah Rubens, John Strang, Ralph Brasacchio, Lydia Liao, Wan Sing Ng, and Yan Yu. In vivo motion and force measurement of surgical needle intervention during prostate brachytherapy. *Med Phys*, 33(8):2915–2922, 2006.
- [21] T. K. Podder, J. Sherman, E. M. Messing, D. J. Rubens, D. Fuller, J. G. Strang, R. A. Brasacchio, and Y. Yu. Needle insertion force estimation model using procedure-specific and patient-specific criteria. In *28th Annual International Conference of the IEEE EMBS*, pages 555–558, New York City, 2006.

- [22] Jeffrey Taylor Stellman. Development, production, and characterization of plastic hypodermic needles. Master's thesis, Georgia Institute of Technology, August 2009.
- [23] Toshiyasu Suzuki, Akira Tanaka, Haruo Fukuyama, Junichi Nishiyama, Masahiro Kanazawa, Masatoshi Oda, and Miwa Takahashi. Differences in penetration force of intravenous catheters - effect of grinding methods on inner needles of intravenous catheters. *Tokai J Exp Clin Med*, 29(4):175–181, 2004.
- [24] Jonathan L. Westbrook, David R. Uncles, B. Todd Sitzman, and Len E. S. Carrie. Comparison of the force required for dural puncture with different spinal needles and subsequent leakage of cerebrospinal fluid. *Anesth Analg*, 79:769–772, 1994.
- [25] K. Yan, T. Podder, L. Li, J. Joseph, D. R. Rubens, E. M. Messing, L. Liao, and Y. Yu. A real-time prostate cancer detection technique using needle insertion force and patient-specific criteria during percutaneous intervention. *Med Phys*, 36(7):3356–3362, 2009.
- [26] Jessica R. Crouch, Chad M. Schneider, Josh Wainer, and Allison M. Okamura. A velocity-dependent model for needle insertion in soft tissue. In *Lect Notes Comput Sc*, pages 624–632. Springer Berlin / Heidelberg, Berlin, 2005.
- [27] D. Gossot, P. Validire, S. Matsumoto, H. Tokumura, K. Shimomura, J. Flowers, N. Borenstein, and Daniel. P. Development of an ultrasonically activated trocar system. *Surg Endosc*, 16:210–214, 2002.
- [28] J. T. Hing, A. D. Brooks, and J. P. Desai. Reality-based needle insertion simulation for haptic feedback in prostate brachytherapy. In *IEEE International Conference on Robotics and Automation, ICRA 2006*, pages 619–624, 2006.
- [29] James T. Hing, Ari D. Brooks, and Jaydev P. Desai. A biplanar fluoroscopic approach for the measurement, modeling, and simulation of needle and soft-tissue interaction. *Med Image Anal*, 11:62–78, 2007.
- [30] Yo Kobayashi, Takahiro Sato, and Masakatsu G. Fujie. Modeling of friction force based on relative velocity between liver tissue and needle for needle insertion simulation. In *31st Annual International Conference of the IEEE EMBS*, pages 5274–5278, Minneapolis, Minnesota, 2009.
- [31] Kiyoshi Matsumiya, Yasuyuki Momoi, Etsuko Kobayashi, Nobuhiko Sugano, Kazuo Yonenobu, Hiroshi Inada, Takayuki Tsuji, and Ichiro Sakuma. Analysis of forces during robotic needle insertion to human vertebra. In *Lect Notes Comput Sc*, volume 2878, pages 271–278. Springer, Berlin, 2003.
- [32] G. Mayer, V. Knappertz, and P. Kinast. Needles: A comparison study. Technical report, European Medical Device Technology, 2009.

- [33] Fabian Mueller. Biomechanical test report on hsw fine-ject needles. Technical report, Henke-Sass Wolf GmbH, 2011.
- [34] Daisaku Okuno, Tatsuo Togawa, Hirokazu Saito, and Kiichi Tsuchiya. Development of an automatic blood sampling system: control of the puncturing needle by measuring forces. In *20th Annu. Int. Conf. of the IEEE Eng. in Medicine and Biology Soc.*, pages 1811–1812, Hong Kong, 1998.
- [35] Tarun K. Podder, Jason Sherman, Dave Fuller, Edward M. Messing, Deborah J. Rubens, John G. Strang, Ralph A. Brasacchio, and Yan Yu. In-vivo measurement of surgical needle intervention parameters: A pilot study. In *28th Annual International Conference of the IEEE EMBS*, pages 3652–3655, New York City, USA, 2006.
- [36] T. K. Podder, J. Sherman, L. Li, J. Joseph, D. R. Rubens, E. M. Messing, J. Huang, and Y. Yu. Mechanical properties of human prostate tissue in the context of surgical needle insertion. *Int J Comp Assist Radiol Surg*, 2: S82–S133, 2007.
- [37] H. Saito and T. Togawa. Detection of needle puncture to blood vessel using puncture force measurement. *Med Biol Eng Comput*, 43:240–244, 2005.
- [38] Denis Tran, King-wei Hor, Allaudin A. Kamani, Victoria A. Lessoway, and Robert N. Rohling. Instrumentation of the loss-of-resistance technique for epidural needle insertion. *IEEE Trans Biomed Eng*, 56(3):820–827, 2009.
- [39] A. Wittek, T. Dutta-Roy, Z. Taylor, A. Horton, T. Washio, K. Chinzei, and K. Miller. Subject-specific non-linear biomechanical model of needle insertion into brain. *Comput Meth Biomech Biomed Eng*, 11(2):135–146, 2008.
- [40] Niki Abolhassani, Rajni Patel, and Mehrdad Moallem. Experimental study of robotic needle insertion in soft tissue. *Int Congr Ser*, 1268:797–802, 2004.
- [41] Niki Abolhassani, Rajni Patel, and Mehrdad Moallem. Trajectory generation for robotic needle insertion in soft tissue. In *26th Annual International Conference of the IEEE EMBS*, pages 2730–2733, San Francisco, CA, 2004.
- [42] Niki Abolhassani, Rajni Patel, and Mehrdad Moallem. Control of soft tissue deformation during robotic needle insertion. *Minim Invasiv Ther*, 15(3): 165–176, 2006.
- [43] Niki Abolhassani, Rajni Patel, and Farzam Ayazi. Minimization of needle deflection in robot-assisted percutaneous therapy. *Int J Med Robot Comp*, 3: 140–148, 2007.
- [44] Ali Asadian, Mehrdad R. Kermani, and Rajni V. Patel. A compact dynamic force model for needle-tissue interaction. In *32nd Annual International Conference of the IEEE EMBS*, pages 2292–2295, Buenos Aires, Argentina, 2010. IEEE.

- [45] Ali Asadian, Rajni V. Patel, and Mehrdad R. Kermani. A distributed model for needle-tissue friction in percutaneous interventions. In *IEEE International Conference on Robotics and Automation*, pages 1896–1901, Shanghai, China, 2011. IEEE.
- [46] Toufic Azar and Vincent Hayward. Estimation of the fracture toughness of soft tissue from needle insertion. In F. Bello and E. Edwards, editors, *Lect Notes Comput Sc*, volume 5104, pages 166–175. Springer-Verlag, Berlin, 2008.
- [47] Shadi Badaan, Doru Petrisor, Chunwoo Kim, Pierre Mozer, Dumitru Mazilu, Lucian Gruionu, Alex Patriciu, Kevin Cleary, and Dan Stoianovici. Does needle rotation improve lesion targeting? *Int J Med Robotics Comput Assist Surg*, 7:138–147, 2011.
- [48] Andrew Bzostek, Rajesh Kumar, Lilian Diaz, Mukta Svrivastava, James H. Anderson, and Russell H. Taylor. Force vs deformation in soft tissue puncture, 1999. Unpublished.
- [49] Young Bin Choy, Hong Cao, Supan Tungjitkusolmun, Jang-Zern Tsai, Dieter Haemmerich, Vicken R. Vorperian, and John G. Webster. Mechanical compliance of the endocardium. *J Biomech*, 35:1671–1676, 2002.
- [50] Simon P. DiMaio and Septimiu E. Salcudean. Needle insertion modelling and simulation. In *IEEE International Conference on Robotics and Automation, ICRA 2002*, pages 2098–2105, Washington, DC, 2002.
- [51] Simon P. DiMaio and Septimiu E. Salcudean. Needle insertion modeling and simulation. *IEEE Trans Robot Autom*, 19(5):864–875, 2003.
- [52] Andrew E. Healey, Jonathan C. Evans, Michael G. Murphy, Steven Powell, Thien V. How, David Groves, Fraser Hatfield, Bernard M. Diaz, and Derek A. Gould. In vivo force during arterial interventional radiology needle puncture procedures. In J.D. Westwood, editor, *St Heal T*, volume 13, pages 178–184. IOS Press, 2005.
- [53] Matt Heverly and Pierre Dupont. Trajectory optimization for dynamic needle insertion. In *IEEE International Conference on Robotics and Automation, ICRA 2005*, pages 1658–1663, Barcelona, Spain, 2005.
- [54] Leslie L. Hiemenz Holton. Force models for needle insertion created from measured needle puncture data. In J.D. Westwood, editor, *St Heal T*, pages 180–186. IOS Press, 2001.
- [55] Matthew A. Howard, Bruce A. Abkes, Michael C. Ollendieck, Myoung-gyu D. Noh, Rogers C. Ritter, and George T. Gillies. Measurement of the force required to move a neurosurgical probe through in vivo human brain tissue. *IEEE Trans Biomed Eng*, 46(7):891–894, 1999.

- [56] Hiroyuki Kataoka, Toshikatsu Washio, Kiyoyuki Chinzei, Kazuyuki Mizuhara, Christina Simone, and Allison M. Okamura. Measurement of the tip and friction force acting on a needle during penetration. In *Lect Notes Comput Sc*, volume 2488, pages 216–223. Springer Berlin / Heidelberg, Berlin, 2002.
- [57] Yo Kobayashi, Akinori Onishi, Hiroki Watanabe, Takeharu Hoshi, Kazuya Kawamura, Makoto Hashizume, and Masakatsu G. Fujie. Development of an integrated needle insertion system with image guidance and deformation simulation. *Comput Med Imag Grap*, 34:9–18, 2010.
- [58] X.Q. Kong and C.W. Wu. Measurement and prediction of insertion force for the mosquito fascicle penetrating into human skin. *J Bionic Eng*, 6(2): 143–152, 2009.
- [59] V. Lagerburg, M. A. Moerland, M. K. Konings, R. E. van de Vosse, J. J. W.Legendijk, and J. J. Battermann. Development of a tapping device: a new needle insertion method for prostate brachytherapy. *Phys Med Biol*, 51:891–902, 2006.
- [60] Helene M. Langevin, David L. Churchill, James R. Fox, Gary J. Badger, Brian S. Garra, and Martin H. Krag. Biomechanical response to acupuncture needling in humans. *J Appl Physiol*, 91:2471–2478, 2001.
- [61] Timo J. Lechner, Maarten G. van Wijk, Ad J. Maas, Frank R. van Dorsten, Ronald A. Drost, Chris J. Langenberg, Leo J. Teunissen, Paul H. Cornelissen, and Jan van Niekerk. Clinical results with the acoustic puncture assist device, a new acoustic device to identify the epidural space. *Anesth Analg*, 96:1183–1187, 2003.
- [62] T.J.M. Lechner, M.G.F. van Wijk, A.J.J. Maas, and F.R.C. van Dorsten. Thoracic epidural puncture guided by an acoustic signal: clinical results. *Eur J Anaesth*, 21:694–699, 2004.
- [63] M. C. Lewis, J. P. Lafferty, M. S. Sacks, V. S. Pallares, and M. TerRiet. How much work is required to puncture dura with tuohy needles? *Brit J Anaesth*, 85(2):238–241, 2000.
- [64] Mohsen Mahvash and Pierre E. Dupont. Fast needle insertion to minimize tissue deformation and damage. In *IEEE International Conference on Robotics and Automation, ICRA 2009*, pages 3097–3102, Kobe, Japan, 2009.
- [65] B. Maurin, L. Barbe, B. Bayle, P. Zanne, J. Gangloff, M. De Mathelin, A. Gangi, L. Soler, and A. Forgione. In vivo study of forces during needle insertions. In *Medical Robotics, Navigation and Visualisation Scientific Workshop*, pages 415–422, Remagen, Germany, 2004.

- [66] M.A. Meltsner, N.J. Ferrier, and B.R. Thomadsen. Observations on rotating needle insertions using a brachytherapy robot. *Phys Med Biol*, 52:6027–6037, 2007.
- [67] Sarthak Misra, Kyle B. Reed, Andrew S. Douglas, K. T. Ramesh, and Allison M. Okamura. Needle-tissue interaction forces for bevel-tip steerable needles. In *IEEE/RAS-EMBS International Conference on Biomedical Robotics and Biomechatronics*, pages 224–231, Scottsdale, AZ, 2008.
- [68] S. Misra, K.B. Reed, B.W. Schafer, K.T. Ramesh, and A.M. Okamura. Mechanics of flexible needles robotically steered through soft tissue. *Int J Robot Res*, 29(13):1640–1660, 2010.
- [69] K. Naemura. Comparative phantom study on epidural anesthesia needle. In *28th Annual International Conference of the IEEE EMBS*, pages 4995–4998, New York City, 2006.
- [70] K. Naemura, Y. Uchino, and H. Saito. Effect of the needle tip height on the puncture force in a simplified epidural anesthesia simulator. In *29th Annual International Conference of the IEEE EMBS*, pages 3504–3507, Lyon, France, 2007.
- [71] K. Naemura, A. Sakai, T. Hayashi, and H. Saito. Epidural insertion simulator of higher insertion resistance and drop rate after puncture. In *30th Annual International Conference of the IEEE EMBS*, pages 3249–3252, Vancouver, British Columbia, Canada, 2008.
- [72] C. Thang Nguyen, Toan Vu-Khanh, Patricia I. Dolez, and Jaime Lara. Puncture of elastomer membranes by medical needles. part i: Mechanisms. *Int J Fract*, 155:75–81, 2009.
- [73] Mark D. O’Leary, Christina Simone, T. Washio, K. Yoshinaka, and Allison M. Okamura. Robotic needle insertion: Effects of friction and needle geometry. In *IEEE International Conference on Robotics and Automation, ICRA 2003*, pages 1774–1780, Taipei, Taiwan, 2003.
- [74] Tarun K. Podder, Douglas P. Clark, Dave Fuller, Jason Sherman, Wan Sing Ng, Lydia Liao, Deborah J. Rubens, John G. Strang, Edward M. Messing, Y.D. Zhang, and Yan Yu. Effects of velocity modulation during surgical needle insertion. In *IEEE Eng Med Biol*, pages 5766–5770, Shanghai, China, 2005.
- [75] T. K. Podder, J. Sherman, D. P. Clark, E. M. Messing, D. J. Rubens, J. G. Strang, L. Liao, R. A. Brasacchio, Y. Zhang, W. S. Ng, and Y. Yu. Evaluation of robotic needle insertion in conjunction with in vivo manual insertion in the operating room. In *IEEE International Workshop on Robots and Human Interactive Communication*, pages 66–72, 2005.

- [76] Kyle B. Reed, Allison M. Okamura, and Noah J. Cowan. Controlling a robotically steered needle in the presence of torsional friction. In *IEEE International Conference on Robotics and Automation, ICRA 2009*, pages 3476–3481, Kobe, Japan, 2009.
- [77] Alex Jahya Roy J. Roesthuis, Youri R.J. van Veen and Sarthak Misra. Mechanics of needle-tissue interaction. In *IEEE/RSJ International Conference on Intelligent Robots and Systems*, pages 2557–2563, San Francisco, CA, USA, 2011. IEEE.
- [78] Hirokazu Saito and Tatsuo Togawa. Detection of puncturing blood vessel wall for automatic blood sampling. In *The First Joint BMES/EMBS Conference Serving Humanity, Advancing Technology*, page 866, Atlanta, GA, 1999.
- [79] Chad Michael Schneider, Jessica R. Crouch, and Allison M. Okamura. Modeling and measuring the dynamic 3d effects of needle insertion in soft tissue. Technical Report 04-1, The Johns Hopkins University, June 1 2004.
- [80] Oliver A. Shergold and Norman A. Fleck. Experimental investigation into the deep penetration of soft solids by sharp and blunt punches, with application to the piercing of skin. *J Biomech Eng*, 127(5):838–848, 2005.
- [81] Christina Simone. Modeling of needle insertion forces for percutaneous therapies. Master’s thesis, The Johns Hopkins University, May 2002.
- [82] Christina Simone and Allison M. Okamura. Modeling of needle insertion forces for robot-assisted percutaneous therapy. In *IEEE International Conference on Robotics and Automation, ICRA 2002*, pages 2085–2091, Washington, DC, 2002.
- [83] Niki Abolhassani and Rajni Patel. Deflection of a flexible needle during insertion into soft tissue. In *28th Annual International Conference of the IEEE EMBS*, pages 3858–3861, New York City, USA, 2006.
- [84] L. Barbe, B. Bayle, M. de Mathelin, and A. Gangi. Online robust model estimation and haptic clues detection during in vivo needle insertions. In *IEEE International Conference on Biomedical Robotics and Biomechatronics*, page 341, Pisa, Italy, 2006.
- [85] Peter N. Brett, T.J. Parker, Andrew J. Harrison, Trevor A. Thomas, and A. Carr. Simulation of resistance forces acting on surgical needles. *P I Mech Eng H*, 211:335–347, 1997.
- [86] Peter N. Brett, Andrew J. Harrison, and Trevor A. Thomas. Schemes for the identification of tissue types and boundaries at the tool point for surgical needles. *IEEE Trans Inf Technol Biomed*, 4(1):30–36, 2000.

- [87] Iman Brouwer, Jeffrey Ustin, Loren Bentley, Alana Sherman, Neel Dhruv, and Frank Tendick. Measuring in vivo animal soft tissue properties for haptic modeling in surgical simulation. In et al. Westwood, J.D., editor, *St Heal T*, pages 69–74. IOS Press, 2001.
- [88] Ehsan Dehghan, Xu Wen, Reza Zahiri-Azar, Maud Marchal, and Septimiu E. Salcudean. Modeling of needle-tissue interaction using ultrasound-based motion estimation. In *Lect Notes Comput Sc*, volume 4791, pages 709–716. Springer Berlin / Heidelberg, 2007.
- [89] Ehsan Dehghan, Xu Wen, Reza Zahiri-Azar, Maud Marchal, and Septimiu E. Salcudean. Parameter identification for a needle-tissue interaction model. In *29th Annual International Conference of the IEEE EMBS*, pages 190–193, Lyon, France, 2007.
- [90] Ehsan Dehghan and Septimiu E. Salcudean. Needle insertion study using ultrasound-based 2d motion tracking. In D. Metaxas, editor, *Lect Notes Comput Sc*, volume 5242, pages 660–667. Springer-Verlag, Berlin, 2008.
- [91] Simon P. DiMaio and Septimiu E. Salcudean. Simulated interactive needle insertion. In *10th IEEE Symposium On Haptic Interfaces For Virtual Environments and Teleoperator Systems*, page 344, Orlando, Florida, 2002.
- [92] Simon P. DiMaio and Septimiu E. Salcudean. Interactive simulation of needle insertion models. *IEEE Trans Biomed Eng*, 52(7):1167–1179, 2005.
- [93] Abdalla A. Elagha, Ann H. Kim, Ozgur Kocaturk, and Robert J. Lederman. Blunt atrial transseptal puncture using excimer laser in swine. *Catheter Cardio Inte*, 70:585–590, 2007.
- [94] Imran Fazal and Mohd D. Karsiti. Needle insertion forces for haptic feedback device. In *IEEE Symposium on Industrial Electronics and Applications*, pages 20–22, Kuala Lumpur, Malaysia, 2009.
- [95] L. Hiemenz, A. Litsky, and P. Schmalbrock. Puncture mechanics for the insertion of an epidural needle. In *21st Annual Meeting of the American Society of Biomechanics*, Clemson, South Carolina, 1997.
- [96] Leslie Hiemenz, Don Stredney, and Petra Schmalbrock. Development of the force feedback model for an epidural needle insertion simulator. In J.D. Westwood and H.M. Hoffman, editors, *St Heal T*, pages 272–277. IOS Press, 1998.
- [97] Nikolai Hungr, Jocelyne Troccaz, Nabil Zemiti, and Nathanael Tripodi. Design of an ultrasound-guided robotic brachytherapy needle-insertion system. In *31st Annual International Conference of the IEEE EMBS*, pages 250–253, Minneapolis, MN, 2009.

- [98] Hiroyuki Kataoka, Shigeho Noda, Hideo Yokota, Shu Takagi, Ryutaro Himeno, and Shigenobu Okazawa. Simulations of needle insertion by using a eulerian hydrocode fem and the experimental validations. In *Lect Notes Comput Sc*, volume 5242, pages 560–568. Springer, Berlin, 2008.
- [99] Yo Kobayashi, Akinori Onishi, Takeharu Hoshi, Kazuya Kawamura, Makoto Hashizume, and Masakatsu G. Fujie. Development and validation of a viscoelastic and nonlinear liver model for needle insertion. *Int J Comp Assist Radiol Surg*, 4(1):53–63, 2009.
- [100] Yo Kobayashi, Makiko Suzuki, Kozo Konishi, Makoto Hashizume, and Masakatsu G. Fujie. Development of a novel approach, palpation based needle insertion, for breast cancer treatment. In *IEEE International Conference on Robotics and Biomimetics*, pages 505–511, Bangkok, Thailand, 2009.
- [101] Yo Kobayashi, Onishi Akinori, Hiroki Watanabe, Takeharu Hoshi, Kazuya Kawamura, and Masakatsu G. Fujie. Developing a planning method for straight needle insertion using probability-based condition where a puncture occurs. In *IEEE International Conference on Robotics and Automation, ICRA 2009*, pages 3482–3489, Kobe, Japan, 2009.
- [102] Yo Kobayashi, Makiko Suzuki, Atsushi Kato, Kozo Konishi, Makoto Hashizume, and Masakatsu G. Fujie. A robotic palpation-based needle insertion method for diagnostic biopsy and treatment of breast cancer. In *IEEE/RSJ International Conference on Intelligent Robots and Systems*, pages 5534–5539, St. Louis, USA, 2009.
- [103] Rebecca Kokes, Kevin Lister, Rao Gullapalli, Bao Zhang, Alan MacMillan, Howard Richard, and Jaydev P. Desai. Towards a teleoperated needle driver robot with haptic feedback for rfa of breast tumors under continuous mri. *Med Image Anal*, 13:445–455, 2009.
- [104] Thomas S. Lendvay, Feng-Ju Hsieh, Blake Hannaford, and Jacob Rosen. *The Biomechanics of Percutaneous Needle Insertion*. St Heal T. Newport Beach, CA, 2008.
- [105] Sarthak Misra, Kyle B. Reed, K. T. Ramesh, and Allison M. Okamura. Observations of needle-tissue interactions. In *31st Annual International Conference of the IEEE EMBS*, pages 262–265, Minneapolis, Minnesota, 2009.
- [106] C. Thang Nguyen, Toan Vu-Khanh, Patricia I. Dolez, and Jaime Lara. Puncture of elastomer membranes by medical needles. part ii: Mechanics. *Int J Fract*, 155:83–91, 2009.
- [107] Z. T. H. Tse, H. Elhawary, M. Rea, I. Young, B. L. Davis, and M. Lamperth. A haptic unit designed for magnetic-resonance-guided biopsy. *P I Mech Eng H*, 223:159–172, 2009.

- [108] Franck P. Vidal, Nigel W. John, Andrew E. Healey, and Derek A. Gould. Simulation of ultrasound guided needle puncture using patient specific data with 3d textures and volume haptics. *Comput Anim Virtual Worlds*, 19:111–127, 2008.
- [109] H. Wiksell, V. Ekstrand, C. Wadstrom, and G. Auer. A new semi-automated instrument to improve the fine needle aspiration procedure during breast lesion cell sampling. *Physica Med*, 25:128–132, 2009.
- [110] Yu Xie, Dong Sun, Chong Liu, Shuk H. Cheng, and Yun H. Liu. A force control based cell injection approach in a bio-robotics system. In *IEEE International Conference on Robotics and Automation, ICRA 2009*, pages 3443–3448, Kobe, Japan, 2009.
- [111] W. Xu, T. G. Frank, and A. Cuschieri. Development of a shape memory alloy multiple-point injector for chemotherapy. *P I Mech Eng H*, 219:213–217, 2005.
- [112] Aleksandar Zivanovic and Brian L. Davies. A robotic system for blood sampling. *IEEE Trans inf Technol Biomed*, 4(1):8–14, 2000.
- [113] A.P.S. Selvadurai. Deflections of a rubber membrane. *J Mech Phys Solids*, 54:1093–1119, 2006.
- [114] Mohsen Mahvash and Vincent Hayward. Haptic rendering of cutting: A fracture mechanics approach. *Haptics-e*, 2(3):1–12, 2001.
- [115] R. A. Lawrie and D. A. Ledward. *Lawrie's meat science*. Woodhead Publishing Limited, Cambridge, seventh edition, 2006.
- [116] Paul D. Warriss. *Meat Science: An Introductory Text*. CABI, Oxfordshire, 2nd edition, 2010.
- [117] Robert A Day. The origins of the scientific paper: the imrad format. *J. Am. Med. Writers Assoc.*, 4:16–18, 1989.
- [118] Paulraj Ponniah. *Database Design and Development: An Essential Guide for IT Professionals*. John Wiley & Sons, Hoboken, NJ, 2003.
- [119] Matthew Norman. *Database Design Manual: using MySQL for Windows*. Springer-Verlag, London, 2004.
- [120] Gavin Powell. *Oracle Performance Tuning for 10gR2*. Elsevier Digital Press, Burlington, MA, 2nd edition, 2007.
- [121] Peidong Han, Demeng Che, Kumar Pallav, and Kornel Ehmann. Models of the cutting edge geometry of medical needles with applications to needle design. *Int J Mech Sci*, 65:157–167, 2012.
- [122] Jason Zachary Moore. *Tissue cutting in needle biopsy*. PhD thesis, 2011.

- [123] Cynthia Donahey, Robert W Matteson, and Lawrence W Schneider. The effect of point geometry on needle penetration parameters. Technical Report UM-HSRI-80-55, University of Michigan, July 1980.
- [124] Ispg products: Cannulae, retrieved: April 25, 2013, from <http://www.ispg.com/cannulae.html>.
- [125] Lawrence W Schneider, Leigh S Peck, and John W Melvin. Penetration characteristics of hypodermic needles in potential skin simulants - Series I. Technical Report UM-HSRI-78-29, University of Michigan, July 1978.
- [126] H J Qi and M C Boyce. Stress-strain behavior of thermoplastic polyurethanes. *Mech Mater*, 37:817–839, 2005.
- [127] Lucas J Pavlovich, W Lyle McClung, John G Thacker, Richard F Edlich, and George T Rodeheaver. A synthetic membrane for testing needle penetration. *J Appl Biomater*, 4:157–160, 1993.
- [128] Yann Barrandon and Howard Green. Cell size as a determinant of the clone-forming ability of human keratinocytes. *Proc Natl Acad Sci USA*, 82:5390–5394, 1985.
- [129] Valentin Lulevich, Hsin-ya Yang, R Rivkah Isseroff, and Gang-yu Liu. Single cell mechanics of keratinocyte cells. *Ultramicroscopy*, 110:1435–1442, 2010.
- [130] Dow corning 360 medical fluid - frequently asked questions. Technical Report 52-1038-01, Dow Corning Corporation, 2002.
- [131] Dow corning mdx4-4159, 50% medical grade dispersion - frequently asked questions. Technical Report 52-1039A-01, Dow Corning Corporation, 2002.
- [132] Andre Colas, Jason Siang, and Kathy Ulman. Silicones in pharmaceutical applications. Part 5: Siliconization of parenteral packaging components. Technical Report 52-1094-01, Dow Corning Corporation, 2006.
- [133] Lawrence W Schneider, Leigh S Peck, and John W Melvin. Penetration characteristics of hypodermic needles in skin and muscle tissue - Phase I. Technical Report UM-HSRI-78-23, University of Michigan, June 1978.
- [134] J S Pulido, M E Zobitz, and K N An. Scleral penetration force requirements for commonly used intravitreal needles. *Eye*, 21:1210–1211, 2007.
- [135] Douglas Kline and Terry Kuhn. Needle reuse and tip damage. *Diabetes Care*, 27(2):617, 2004.
- [136] Ian Nock, Robert Parkin, and Brian Dalay. An investigation of the force-time characteristics of needle insertions into isobutene-isoprene (butyl) rubber bungs used in the pharmaceutical industry. *T I Meas Control*, 15(2):81–86, 1993.

- [137] Roger E Kirk. *Experimental Design: Procedures for the Behavioral Sciences*. SAGE Publications, Thousand Oaks, CA, fourth edition, 2013.
- [138] Gary W. Oehlert. *A First Course in Design and Analysis of Experiments*. University of Minnesota, Minneapolis, MN, 2010.
- [139] H J Keselman, James Algina, and Rhonda K Kowalchuk. The analysis of repeated measures designs: A review. *Br J Math Stat Psychol*, 54:1–20, 2001.
- [140] James Stevens. *Applied Multivariate Statistics for the Social Sciences*. Lawrence Erlbaum Associates, Hillsdale, NJ, 1992.
- [141] Katherine S Button, John P A Ioannidis, Claire Mokrysz, Brian A Nosek, Jonathan Flint, Emma S J Robinson, and Marcus R Munafo. Power failure: why small sample size undermines the reliability of neuroscience. *Nat Rev Neurosci*, 14:365–376, 2013.
- [142] Raymond B. Dyer, John D. Regan, Peter V. Kavanagh, Elaine G. Khatod, Michael Y. Chen, and Ronald J. Zagoria. Percutaneous nephrostomy with extensions of the technique: Step by step. *RadioGraphics*, 22(3):503–525, 2002.
- [143] Harold Ellis. The anatomy of the kidney and ureter. *Surgery*, 20(9):201–203, 2002.
- [144] David H Douglas and Thomas K Peucker. Algorithms for the reduction of the number of points required to represent a digitized line or its caricature. *The Canadian Cartographer*, 10(2):112–122, 1973.
- [145] Ralph B D’Agostino and Michael A Stephens. *Goodness-of-Fit Techniques*. Marcel Dekker Inc., New York, 1986.
- [146] T W Anderson and D A Darling. A test of goodness of fit. *J Am Stat Assoc*, 49(268):765–769, 1954.
- [147] Ingrid Kerckaert, Tom Van Hoof, Piet Pattyn, and D’Herde Katharina. Endogent: Centre for anatomy and invasive techniques. *Anatomy*, 2:28–33, 2008.
- [148] C.A. van Ee, A.L. Chasse, and B.S. Myers. Quantifying skeletal muscle properties in cadaveric test specimens: Effects of mechanical loading, post-mortem time, and freezer storage. *J Biomech Eng*, 122:9–14, 2000.
- [149] Savio L.Y. Woo, Carlo A. Orlando, Jonathan F. Camp, and Wayne H. Akeson. Effects of postmortem storage by freezing on ligament tensile behavior. *J. Biomechanics*, 19(5):399–404, 1986.
- [150] D J van Gerwen, J Dankelman, and J J van den Dobbels. Measurement and stochastic modeling of kidney puncture forces. *Ann Biomed Eng*, In Press, 2013.

- [151] P F Villard, F P Vidal, L ap Cenydd, R Holbrey, S Pisharody, S Johnson, A Bulpitt, N W John, F Bello, and D Gould. Interventional radiology virtual simulator for liver biopsy. *Int J CARS*, pages 1–13, 2013.
- [152] Robert Marcovich and Arthur D. Smith. Percutaneous renal access: tips and tricks. *Brit J Urol Int*, 95(s2):78–84, 2005.
- [153] Arthur D. Smith, Gopal Badlani, Glenn M. Preminger, and Louis R. Kavoussi. *Smith's Textbook of Endourology*. Wiley-Blackwell, Chichester, 3rd edition, 2012.
- [154] E. C. B. Hall-Craggs. *Anatomy - as a Basis for Clinical Medicine*. Williams & Wilkins, London, third edition, 1995.
- [155] Michael Schuenke, Erik Schulte, and Udo Schumacher. *Thieme Atlas of Anatomy - Neck and Internal Organs*. Georg Thieme Verlag, Stuttgart, 1st edition, 2010.
- [156] J Zhai, K Karuppasamy, R Zvavanjanja, M Fisher, D Gould, and T How. A sensor for needle puncture force measurement during interventional radiological procedures. *Med Eng Phys*, 35:350–356, 2013.
- [157] M. Michael Swindle and Alison C. Smith. Comparative anatomy and physiology of the pig. *Scand J Lab Anim Sci Suppl*, 25:11–21, 1998.
- [158] C Spearman. The proof and measurement of association between two things. *Am J Psychol*, 15(1):72–101, 1904.
- [159] David C Lay. *Linear Algebra and Its Applications*. Addison-Wesley, Reading, MA, 2nd edition, 2000.
- [160] J L Hodges. The significance probability of the Smirnov two-sample test. *Arkiv för Matematik*, 3(43):469–486, 1958.
- [161] Frank J Massey. The kolmogorov-smirnov test for goodness of fit. *J Am Stat Assoc*, 46(253):68–78, 1951.
- [162] Waloddi Weibull. A statistical distribution function of wide applicability. *J Appl Mech*, pages 293–297, 1951.
- [163] James W Dally. Statistical analysis of experimental data. In William N Sharpe, editor, *Springer Handbook of Experimental Solid Mechanics*, pages 259–280. Springer, New York, 2008.
- [164] D.J. van Gerwen and J.J. van den Dobbelsteen. Effects of needle reuse on puncture force characteristics. In *Design of Medical Devices Conference Europe*, Delft, The Netherlands, 2013.

Dankwoord

Na jaren tegenover familie en vrienden te hebben volgehouden dat ik nooit, maar dan ook écht nooit, zou gaan promoveren, lijkt het tegendeel nu toch bewaarheid te worden. Het boek ligt er in ieder geval. Daarom, lieve Anna en Olivia, lieve (schoon-)ouders, broers, zussen, en Tom, Koen, Marijn, Rolf, Willem, en Bram: Sorry dat ik me niet aan mijn woord heb gehouden. In hoeverre het doctoreren daadwerkelijk heeft geleid tot de verwachte onherroepelijke sociale, psychische, en fysieke schade valt nog te bezien.

Eén van de belangrijkste eisen om een promotietraject te kunnen uitzitten is dat je leuke collega's hebt. Gelukkig is in mijn geval ruimschoots aan die voorwaarde voldaan. Zonder de vele mooie (en soms minder mooie) momenten met mijn lot- en labgenoten Tim, Kirsten, John, Arjan, Nick, Linda, Filip, Patrice, David, en Pablo, met de heren instrumentmakers, Hans, Andries, Nisse, en (andere) John, en met Jenny en de rest van de afdeling, zou het leven als promovendus er een stuk minder rooskleurig uit hebben gezien.

Verder spreekt het hopelijk voor zich dat ik iedereen erg dankbaar ben die, op wat voor manier dan ook, een bijdrage heeft geleverd aan dit proefschrift.

Curriculum Vitae

Personal information:

Name: Dennis Jordi van Gerwen
Date of birth: February 26, 1980
Place of birth: Amstelveen, The Netherlands

Relevant work experience:

2009-2013 Ph.D. candidate: Needle-tissue interaction mechanics
Department of Biomechanical Engineering, Faculty of Mechanical,
Maritime, and Materials Engineering, Delft University of
Technology, Delft, The Netherlands

2006–2009 Researcher: Ornicopter rotor analysis and design
Department of Design of Aircraft and Rotorcraft, Faculty of
Aerospace Engineering, Delft University of Technology, Delft, The
Netherlands

Education:

Feb 2006 M.Sc. Aerospace Engineering
Specialization Flight Mechanics and Propulsion
Delft University of Technology, Delft, The Netherlands
Thesis title: "An investigation into Ornicopter rotor blade behavior"

Oct 2003 B.Sc. Aerospace Engineering
Delft University of Technology, Delft, The Netherlands

Jul 2000 Propedeutic exam Aerospace Engineering (honors)
Delft University of Technology, Delft, The Netherlands

Jul 1999 Propedeutic exam Aeronautical engineering
HTS-Haarlem, Haarlem, The Netherlands

Jun 1998 VWO (atheneum)
Titus Brandsmalyceum, Oss, The Netherlands

